CORA Cork Open Research Archive
Cartlann Taighde Oscailte Chorcaí

Title	Laser fabrication of porous, 3D graphene-like carbon from polyimide and sustainable bioplastics
Authors	Larrigy, Cathal
Publication date	2022-06
Original Citation	Larrigy, C. 2022. Laser fabrication of porous, 3D graphene-like carbon from polyimide and sustainable bioplastics. PhD Thesis, University College Cork.
Type of publication	Doctoral thesis
Rights	© 2022, Cathal Larrigy. - https://creativecommons.org/licenses/by-nc-nd/4.0/
Download date	2026-11-15 04:41:25
Item downloaded from	https://hdl.handle.net/10468/14517

UCC
University College Cork, Ireland
Coláiste na hOllscoile Corcaigh

Ollscoil na hÉireann, Corcaigh

NATIONAL UNIVERSITY OF IRELAND, CORK



Laser fabrication of porous, 3D graphene-like carbon from polyimide and sustainable bioplastics

A thesis presented to

The National University of Ireland

For the degree of Doctor of Philosophy

By

Cathal Larrigy B.Sc. M.Sc.

School of Chemistry

Tyndall National Institute

University College Cork, Ireland

June 2022

Supervisors: Dr Aidan Quinn and Dr Daniela Iacopino

Head of School of Chemistry: Dr Humphrey Moynihan

Contents

Declaration 5

Acknowledgements 6

List of Acronyms 7

List of Figures 9

List of Tables 20

Thesis Abstract 21

Chapter 1: Introduction 22

1.1 Introduction 23

1.2 Thesis Overview 39

1.3 References 42

Chapter 2: Fabrication and Electrochemical Properties of Three-Dimensional (3D) Porous Graphitic and Graphene like Electrodes Obtained by Low-Cost Direct Laser Writing Methods 49

2.1 Abstract 50

2.2 Introduction 51

2.3 Results and Discussion 54

2.4 Conclusions 70

2.5 Experimental 71

2.6 References 74

Supporting Information 79

Chapter 3: Porous 3D graphene from sustainable materials: laser graphitization of chitosan 91

3.1 Abstract 92

3.2 Introduction 93

3.3 Results and Discussion 96

3.4 Conclusions 117

3.5 Experimental 118

3.6 References 121

Supporting Information 125

Chapter 4: VOC, solvent and humidity sensors from sustainable Chitosan- based Laser-induced graphitic carbon materials 138

4.1 Abstract 139

4.2 Introduction 140

4.3 Results and Discussion 143

Humidity detection 145

Solvent VOC detection 153
4.4 Conclusions 158
4.5 Experimental 159
4.6 References 161
Supporting Information 163
Chapter 5: Discussion and Conclusions 166
5.1 Discussion and Conclusion 167
5.2 Future Work 170
Appendix A: peer reviewed publications 173

Declaration

This is to certify that the work I am submitting is my own and has not been submitted for another degree, either at University College Cork or elsewhere. All external references and sources are clearly acknowledged and identified within the contents. I have read and understood the regulations of University College Cork concerning plagiarism and intellectual property.

X

Cathal Larrigy

Acknowledgements

I would firstly like to thank both of my supervisors, Aidan Quinn, and Daniela Iacopino, for the opportunity to explore this PhD, and their continued guidance and help throughout I am very grateful for their advice and patience.

Many people in Tyndall and externally provided me with great assistance through this thesis, whether that be via training, discussion of results, or general help and assistance in the lab. I would like to mention my gratitude towards Eoghan and Richard, who provided the above, as well as moral support and a few laughs in the process.

On the mention of moral support, I would like to thank the countless friends I have made throughout this process, who provided a great deal of support, and kept my spirits up! Here's to Alida, Alessandra, Veronica, Martina, Jahidul, Khairul, Hassan, Yunyun, Juliette, Claudia, Julie, Shane, Ian, Luiza, Fernando, Colm, Rob, Tarun, Kathleen, and countless others!

Additionally, I would like to thank my friends outside of Tyndall, for their constant support. Whether it's my lifelong friends from back home, the Elmhurst crew and that extended family, the "Mouthful of Quiz" table quiz team, or Kellie <3. You're legends one and all!

And finally, last but not the least, my family, who have been a constant rock of support in every aspect of my life not just this thesis, I wouldn't be who I am today with you all. My sincerest thanks to you for everything.

List of Acronyms

(Acronyms in alphabetical order)

3D/2D	Three dimensional/ Two Dimensional
AC	Alternating Current
a-C	Amorphous carbon
A_D, A_G, A_{2D}	Peak Area under Raman *D*, *G*, 2i peaks, respectively
Ag/AgCl	Silver/Silver Chloride
Al/Mg	Magnesium Aluminium
BE	Binding Energy
BPPG	Basal Plane Pyrolytic Graphite
CA	Contact Angle
CE	Counter Electrode
CLIG	Chitosan-Based Laser-Induced Graphene
CNT	Carbon Nanotubes
CuCl	Copper Chloride
CV	Cyclic Voltammetry
CVD	Chemical Vapour Deposition
CVD-Gr	Chemical Vapour Depositioned Graphene
ΔEp	Peak-To-Peak Separation
DMF	Dimethylformamide
DOS	Density Of Electronic States
EPPG	Edge Plane Pyrolytic Graphite
E_B	Binding Energy
ET	Electron Transfer
$Fe(CN)_6^{3-/4-}$	Ferricyanide
FTIR	Fourier Transform Infrared Spectroscopy
GO	Graphene Oxide
HDPE	High Density Polyethylene
HET	Heterogeneous Electron Transfer
$I_{p,ox}$	Peak Oxidation Current
ITO	Indium Tin Oxide
I_D, I_G, I_{2D}	Peak Intensity under Raman *D*, *G*, 2i peaks, respectively
K2CO3	Potassium Carbonate
KCl	Potassium Chloride
k^0	Average Heterogeneous Electron Transfer Rate
L_a	Crystallite Size
L_i	Track Length
LiCl	Lithium Chloride
LIG	Laser-Induced Graphene

LIG/Pt	Laser-Induced Graphene/ Platinum
$MgCl_2$	Magnesium Chloride
ms/pix	Milliseconds per Pixel
MWNT	Multi-Walled Nanotube
NaCl	Sodium Chloride
p / p0	Pressure Ratio of Absorbed Gas
PEEK	Polyether Ether Ketone
PET	Polyethylene Terephthalate
PHB	Polyhydroxybutyrate
PLA	Polylactic Acid
Pos	Peak Position
PVC	Polyvinyl Chloride
Q-graphene	Quasi-Graphene
Rc	Contact Resistance
RE	Reference Electrode
RFID	Radio Frequency Identification
rGO	Reduced Graphene Oxide
RH	Relative Humidity
R_i	Track Resistance
R_s	Sheet Resistance
RSF	Relative Sensitivity Factor
R_{sheet}	Sheet Resistance
$[Ru(NH3)_6]^{3+/2+}$	Ruthenium (iii) Hexaamine
SEM	Scanning Electron Microscope/Microscopy
SWNT	Single Walled Nanotubes
TEMPO	2,2,6,6-Tetramethylpiperidine-1-Oxyl Radical
TGA	Thermogravimetric Analysis
UV	Ultraviolet
$\nu^{1/2}$	Square Root of electrochemical scan rate, ν
V_a	Total Gas Volume Adsorbed
VOC	Volatile Organic Compounds
WCA	Water Contact Angle
WE	Working Electrode
XPS	X-Ray Photoelectron Spectroscopy
XRD	X-Ray Diffraction

List of Figures

Chapter 1

Figure 1.1.	Structural comparision of (a) graphene and (b) graphite.
Figure 1.2.	Low dimensional forms of carbon nanomaterials.
Figure 1.3.	Schematic showing Tour's groups accidental discovery of LIG while attempting to laser reduced graphene oxide.
Figure 1.4.	Ternary phase diagram of amorphous carbons. The three corners correspond to diamond-like carbon (sp^3) , graphitic carbon (sp^2) , and hydrocarbons (*H*). Green region demonstrates phases which LIG matrials can form.
Figure 1.5.	Adapted Ternary phase diagram of amorphous carbons from A. C. Ferrari and J. Robertson, demonstrating LIG graphitization.
Figure 1.6	Chemical structure of polyimide.
Figure 1.7.	Cumlative global plastic production, for the years 1950-2019, revealing the massive increase of plastic usage over time.
Figure 1.8.	Global plastic waste by disposal, for the years 1950-2015.
Figure 1.9.	Co-ordinate system of the breakdown of varying types of bioplastics.
Figure 1.10.	Chemical structures of chitin, and its de-acetylated form, chitosan.

Chapter 2

Figure 2.1.	a) Schematic of LIG fabrication process; b-d) Photographs of LIG electrochemical platforms showing working (thin line, ~ 120 µm width) and counter/reference electrodes (thick lines, ~ 1 mm width) fabricated at 50 ms/pix dwell time.
Figure 2.2.	Optical (a-d) and scanning electron (e-h) micrographs of LIG electrodes fabricated at 20, 50, 80 and 110 ms/pix dwell times. Scale bars on optical images: 50 µm.
Figure 2.3.	a) Cross-section SEM image of a LIG track written at 50 ms/pix; b) Profilometer height measurements for LIG tracks in the 20 – 120 ms/pix dwell time range.
Figure 2.4.	a) I-V measurements on a transmission line measurement (TLM) structure written at 50 ms/pix dwell time, comprising four different track lengths (L_i) with mm-scale contact pads. b) Corresponding track resistance (R_i) values *vs* length (L_i). Inset: photograph of TLM structures; c) Sheet resistance *vs* dwell time and d) Contact resistance vs dwell time measured for dwell times 10 - 120 ms/pix.
Figure 2.5.	a) Representative Raman spectra of LIG electrodes fabricated at 20, 50, 80 and 110 ms/pix dwell times; b) Full width at half maximum (FWHM) intensity of the D peak vs dwell time; c) FWHM intensity of the G peak *vs* dwell time. Error bars in b) and c) represent standard error on the mean plus fit error; d) I_D/I_G ratios across dwell times; e) Frequency of 2D peak *vs* dwell times.
Figure 2.6.	Survey scans of LIG electrodes fabricated at 20 (black line), 50 (red line), 80 (blue line) and 110 (pink line) ms/pix laser dwell times.

Figure 2.7.	a) ΔEp values recorded in the interval 20 -120 ms/pix dwell time for 5 mM $Ru(NH_3)_6^{3+/2+}$ and $Fe(CN)_6^{3-/4-}$ in 0.1 M KCl solution as supporting electrolyte at 100 mV/s; b) cyclic voltammograms at LIG electrode 50 ms/pix at different scan rates in 5 mM $Ru(NH_3)_6^{3+/2+}$ 0.1 M KCl. Inset: peak oxidation current values vs square root of potential scan rate; c) repeat CVs at LIG electrode 50 ms/pix at 100 mV/s in 5 mM $Fe(CN)_6^{3-/4-}$ 0.1 M KCl; d) CV of 0.5 mM benzocaine at LIG electrode 50 ms/pix in 0.1 M KCl at 100 mV/s, pH = 2. Inset: benzocaine square wave voltammetric response measured for the same electrode.
Figure S2.1.	Optical microscopy images (a-l) of LIG electrodes written at laser burn times 10 - 120 ms/pix.
Figure S2.2.	SEM images (a-l) of LIG electrodes written at laser burn times 10 -120 ms/pix.
Figure S2.3.	a) α_s plot for the determination of the surface area; b) Adsorption (black squares) / desorption (red circles) isotherm obtained for 50 ms/pix LIG material.
Figure S2.4.	Characterization of surface property by contact angle for a) Kapton tape; b) LIG 20 ms/pix; c) LIG 50 ms/pix; d) LIG 80 ms/pix; e) LIG 110 ms/pix.
Figure S2.5.	Variation of D, G and 2D peak position (a-c), 2D FWHM (d) and I_{2D}/I_G (e) trend measured from Raman spectra collected for LIG electrodes written in the interval 10 -120 ms/pix.
Figure S2.6.	Deconvoluted C1s XPS peak of LIG electrodes fabricated at a) 20, b) 50, c) 80 and d) 110 ms/pix laser burn times.
Figure S2.7.	Deconvoluted N1s XPS peak of LIG electrodes fabricated at 20, 50, 80 and 110 ms/pix laser burn times.

Figure S2.8.	Photographs of a) one electrode electrochemical platform assembled in a Teflon electrochemical cell: b) complete electrochemical cell showing LIG working electrode (WE), Ag/AgCl reference electrode (RE) and Pt wire Counter electrode (CE). Free domain photographs courtesy of author Eoghan Vaughan.
Figure S2.9.	Cyclic voltammograms of 50 ms/pix LIG electrodes for 5 mM $Ru(NH_3)_6^{3+/2+}$ in 0.1 M KCl solution as supporting electrolyte recorded with a) LIG working and counter electrode and Pt wire as reference electrode; b) all carbon system. Insets: photographs of the LIG electrodes; c-d) Peak oxidation current *vs* square root of scan rate for a-b).
Figure S2.10.	Cyclic voltammograms of LIG electrodes written between 30 and 120 ms/pix burn times (a-f) for 5 mM $Ru(NH_3)_6^{3+/2+}$ in 0.1 M KCl solution as supporting electrolyte.
Figure S2.11.	a) Cyclic voltammograms of LIG electrode 50 ms/pix at different scan rates in 5 mM $Fe(CN)_6^{3-/4-}$/ 0.1 M KCl; b) Current peak n values *vs* square root of potential scan rate.

Chapter 3

Figure 3.1. Patterning and morphology of chitosan graphene-like carbon electrodes. Schematic process flow, comprising: (a) Deposition and curing of the chitosan formulation. Inset: photo of an as-cured flexible film; (b) Step 1: pre-conditioning a specific region with a 10.6 μm CO_2 laser; (c) Step 2: direct-write graphitization of an electrode pattern within this region using a 405 nm laser; (d) Step-3 post-processing with a 10.6 μm CO_2 laser to form graphene-like carbon. (e) Photo of a typical sample showing the optical contrast associated with the various stages. (f-k) Scanning electron micrographs (SEMs) showing the morphology resulting from the different laser processing steps: (f, g) Quasi-planar film with hierarchical pore network following Step 1; (h, i) High porosity, 3-D morphology following Step 2; (j,k) Further increases in porosity and surface roughness following Step 3.

Figure 3.2. First order peaks in Raman spectra of laser-graphitized chitosan films following (a) 2-step processing; (b) 3-step processing. (c) Second order Raman peaks for the 3-step processed film. (d) Lorentzian fit values for full-width at half maximum intensity (*FWHM*) plotted vs. peak position.

Figure 3.3. C1*s* XPS data (circles) of (a) 2-step laser-processed chitosan; (b) 3-step laser-processed chitosan. The fit for each spectrum (colored line) was deconvoluted into 3 peaks (solid black lines) plus a background term (dashed line).

Figure 3.4. FTIR spectra for a region of an as-cured chitosan film (solid curve) and for a different region from the same film which was exposed to 1-step laser treatment with a 10.6 μm CO_2 laser (dashed curve). Each spectrum is the average of individual spectra acquired at 5 different locations across the as-cured and 1-step treated regions, respectively.

Figure 3.5.	Sheet resistance data for bar structures (inset photo) following 3 laser processing steps ($R_{\text{sheet, 3-step}}$), plotted vs. data following 2 laser processing steps ($R_{\text{sheet, 2-step}}$). Open symbols: Data from 12 devices across 2 substrates where the raster direction for the 405 nm laser pattern (Step#2) was parallel to the direction for CO_2 laser pattern (Steps #1 & #3). Filled symbols: Data from 57 devices across 8 substrates where raster direction for 405 nm pattern was perpendicular to raster direction for CO_2 pattern.
Figure 3.6.	Proof of concept demonstration of transient electrochemical sensing using 3-step laser fabricated graphene-like carbon electrodes from a doctor-bladed chitosan biopolymer. Photos of: an as-prepared single working electrode (a); the 3-electrode electrochemical cell (b); the working electrode following ~40 minutes electrochemical cycling **(d)** cyclic voltammograms from the working electrode in a 5 mM solution of $Fe(CN)_6^{3-/4-}$ in 1 M KCl.
Figure S3.1.	Transmission electron microscopy of 2-step chitosan-based laser-induced graphene material.
Figure S3.2.	(A-C) Transmission electron microscopy of 3-step chitosan-based laser-induced graphene material. Highlighted area (C) shows a winkle structure, with layering, indicative of graphitic structure.
Figure S3.3.	SEM image collage showing changes in surface morphology at different stages of the 3-step chitosan laser-fabricated graphene-like carbon process
Figure S3.4.	Full Raman spectroscopy of (a) 2-step and (b) 3-step processed material.
Figure S3.5.	Maps of Raman fit results for (a) peak intensity ratios of the *D*, *D´*and 2*D* peaks, each normalised to the intensity of the *G* peak for both 2-step and 3-step processed chitosan. (b) Corresponding area ratios.

Figure S3.6.	Nitrogen 1s XPS spectra for 2-step processed material (bottom) and 3-step processed material (top).
Figure S3.7.	Single Thermogravimetric analysis (TGA) measurements conducted in air, (solid) with corrosponding derivative weight (Dashed), of various stages of Chitosan LIG prodction; a) as cured (light blue) , b) 1-step processed (red) , c) 2-step processed (purple) and d) 3-step processed (green).
Figure S3.8	X-Ray diffraction measurements of various stages of Chitosan LIG prodction; as cured (light blue), 1-step processed (red), 2-step processed (purple) and 3-step processed (green).
Figure S3.9	(a-c) Scanning Electron Micrographs (SEMs) of a laser-processed chitosan bioplastic film acquired at boundary between an as-cured region (left) and a 1-step processed region (right). (d, e) SEMs acquired at the boundary between a 1-step processed region (left) and a 2-step processed region (right). 1-step process: 10.6 µm CO_2 laser, ~2.8 W power, 110 mm/sec write speed. 2-step process: 1-step process followed by irradiation with 405 nm laser, 0.5 W power, 120 ms/pixel dwell time.
Figure S3.10	(a, b) SEM images showing: A 2-step patterned "H" structure (a); the same region following the 3rd step (exposure of the entire region using a CO_2 laser) (b). (c) 0-1 V segment of current-voltage (*I-V*) data acquired for the 2-step patterned device shown in (a) and for the same device following the 3rd step.
Figure S3.11	Electrical conductivity test of doctor-bladed Chitosan-based Laser-induced graphene structures, (for 54 of the 57 devices which were under 20 kΩ/sq.) displaying the change in the sheet resistance between 2-step (x-axis) and 3-step process (y-axis).

Figure S3.12 Proof of concept demonstration of transient electrochemical sensing using 3-step laser fabricated graphene-like carbon electrodes from a drop-cast chitosan biopolymer. Photos of an as-prepared single working electrode (a); the 3-electrode electrochemical cell (b); the working electrode following ~20 minutes electrochemical cycling **(d)** cyclic voltammograms from the working electrode in a 5 mM solution of $Fe(CN)_6^{3-/4-}$ in 1 M KCl. **(e)** Peak oxidation and reduction values vs square root of potential scan rate, for Cyclic voltammograms of 1 mM $Fe(CN)_6^{3-/4-}$ in 1 M KCl.

Chapter 4

Figure 4.1. Chitosan-based Laser-induced graphene fabrication process flow for 2-terminal impedance style sensors. a) example of as cured chitosan film, b-e) Chitosan LIG fabrication process b) chitosan film deposited and cured to glass slides, c) Step 1: pre-treatment of chitosan film with 10.6µm CO_2 laser; d) step 2: direct write graphitization of required pattern using 405nm laser; e) step 3: post-processing step with 10.6µm CO2 laser. f) example of chitosan-based laser-induced graphene fabricated 2-terminal impedance style sensor.

Figure 4.2. Imagery of 2-terminal chitosan-based LIG impedance style sensors. a-b) microscope images of centre and edges of gap region. c-d) Scanning electron microscopy of centre gap region. e) Fluorescent microscopy images of centre and edges of gap region. f) macro photo of sensor.

Figure 4.3. Humidity detection scheme for chitosan-based laser-induced graphene fabricated 2-terminal impedance style sensors.

Figure 4.4. Repeated resistance measurements from 2-terminal CLIG impedance sensors exposed to consistent humidity from an aqueous saturated salt solution of lithium chloride.

Figure 4.5. Resistance measurements, from 2-terminal impedance Chitosan based-LIG sensor measurements when exposed to a series of aqueous saturated salt solutions.

Figure 4.6 Humidity detection scheme with humidity-controlled nitrogen gas flow for chitosan-based laser-induced graphene fabricated 2-terminal impedance style sensors.

Figure 4.7	Humidity detection resistance response of chitosan-based laser-induced graphene fabricated 2-terminal impedance style sensors to humidity-controlled nitrogen gas flow.
Figure 4.8	Solvent detection scheme for chitosan-based laser-induced graphene fabricated 2-terminal impedance style sensors.
Figure 4.9	Resistance and capacitance measurements of a 2-terminal impedance Chitosan based-LIG sensor measurement when exposed to 20 µL of ethanol in a 50mL vessel. Purple solid reference line representing analyte introduction, and grey representing purging via pressurized nitrogen gas (light orange dotted line; gas on, dark orange dash line: gas off)
Figure 4.10	Comparison of delta resistive responses from 20µL various VOC solvents; Methanol (Green), Ethanol (blue) isopropanol (yellow), and Acetone (red). Purple solid reference line representing analyte introduction, and grey area representing purging via humidity controlled pressurized nitrogen gas (light orange dotted line; gas on, dark orange dash line: gas off)
Figure S4.1	Repeated capacitance measurements from 2-terminal CLIG impedance sensors exposed to consistent humidity from an aqueous saturated salt solution of lithium chloride.
Figure S4.2	Capacitive measurements, from 2-terminal impedance Chitosan based-LIG sensor measurements when exposed to a series of aqueous saturated salt solutions.
Figure S4.3	Percentage response from capacitive and resistive response of 2-terminal CLIG impedance sensors.

Figure S4.4 Resistance measurements, from 2-terminal impedance Chitosan based-LIG sensor measurements from exposure humidity-controlled nitrogen gas flow. grey area representing humidity controlled pressurized nitrogen gas (light orange dotted line; gas on, dark orange dash line: gas off)

List of Tables

Chapter 2

Table 2.1. Percentage C-C sp^2, C-C sp^3, epoxides-hydroxides, carbonyls carboxyls and π-π* bonding as derived from C1s XPS spectrum deconvolution. The % carbon, oxygen and nitrogen atomic concentration is also presented for the 20, 50, 80 and 110 ms/pix irradiated samples.

Chapter 3

Table 3.1. Results for Lorentzian fits to Raman spectra (Figure 3.2a-c).

Table 3.2. Fit results from XPS Data.

Table 3.3. Peak assignations for FTIR spectra shown in Figure 4.

Chapter 4

Table 4.1 Values of Hansen's solubility parameter for selected solvents.

Table 4.2 Values of dielectric constants for selected solvents.

Thesis Abstract

Laser-induced graphitization (LIG) of materials provides a unique and advantageous method for fabrication of 3D, porous, conductive, carbon structures with high surface area. By using laser-irradiation of target substrates, conductive patterns such as electrochemical or chemiresistive sensing elements can be fabricated additively, thus reducing both the energy footprint and cost. However, typically LIG is fabricated on non-sustainable feedstock substrates, most commonly polyimide. Studies toward using alternative and more sustainable substrates have been researched, and in this thesis one such alternative is explored, chitosan-based laser-induced graphene.

This thesis aims to show the possibilities of laser-induced graphene fabrication, in examining first the fabrication of LIG on polyimide using a low-cost hobbyist 405 nm laser engraving machine, as an alternative low energy intensive fabrication method. Following this the possibility of using a more sustainable substrate as a target precursor for laser-induced graphitization in the form of a chitosan-based LIG. Finally, a potential application using chitosan-based LIG was demonstrated in the form of chemi-resistive 2-terminal impedance devices for sensing humidity and volatile organic compounds.

Chapter 1: Introduction

1.1 Introduction

Graphene, graphite, and various other other low-dimensional carbon nanomaterials have been widely researched for their potential applications due to their unique chemical and physical properties. Graphene being one of the more exciting of these materials.[1–4] However, the fabrication of graphene can be costly, inefficient, and difficult to scale up toward manufacturing levels.[5] In addition, the environmental impact of such substrates and their manufacturing methods can be significant.[6–8] There is an interest towards a less complex and more environmentally sound methods of producing graphene-like materials. Laser-induced graphene is one method widely researched, and the method explored in this thesis, which could address these challenges.

Carbon allotropes have been widely known about for the past few decades. Historically, carbon in the form of carbon black inks, and graphite have been used as writing media[9–11] and carbon-rich sources, such as coal have been implemented as fuel sources.[12–14] Graphite was initially discovered in the 1600s.[11] However, studies into its chemical structure and /or properties didn't begin until the 19th Century, with Ruess and Vogt being the first to use electron microscopy to identify multi-layer and eventually single layers of graphite in 1948.[15]

Pure graphite is a carbon allotrope comprising of multiple layers of carbon atoms arranged in honeycomb patterns, forming a trigonal planar molecular geometry. Each carbon atom within this lattice uses three of its free electrons to bond to three neighbouring (in-plane) carbon atoms covalently, forming sp^2-hybridised bonds. Meanwhile, the carbons' remaining electron becomes delocalised, being able to move anywhere in the sheet. These delocalised electrons form dipole moments between sheets, allowing for Van der Waals interactions, creating a weak bond between

them.[16,17] Therefore within graphitic sheets, bonds between atoms are strong, but conversely, as a result of the weak Van der Waals interactions individual sheets are easily separated from each other. [17,18]

Graphene is the result of isolating a single atomic layer of this graphite. Graphene maintains the covalent bonds within its sheet, while the delocalised electrons remain. Pristine graphene, combined with delocalised electrons, can have a high electric conductivity.[19]

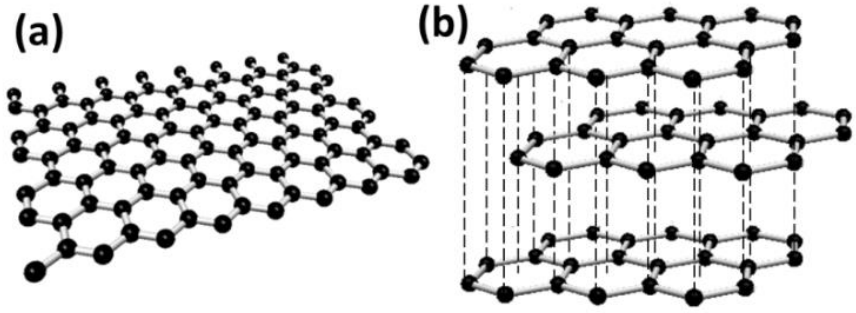


Figure 1.1. Structural comparision of (a) graphene and (b) graphite.[93]

Graphene research initially stems from studies of graphite. Sir Benjamin Collins Brodie in 1859 was the first to describe the structure of graphite-oxide,[20] and this aided in describing the layered nature of graphite. This led to further research in 1947, where PR Wallace first theorised the possibility of single-layer graphite or graphene as it is now known.[21] With improvements in electron microscopy in the late 1940s, layers of graphite could be observed.[15] However, it wasn't until 2004 when Prof. Andre Geim and Prof. Konstantin Novoselov from the University of Manchester, UK successfully managed to isolate graphene using mechanical exfoliation of bulk graphite.[22] For their efforts, they were awarded the Nobel prize in physics in 2010 "for ground-breaking experiments regarding the two-dimensional material graphene".[23]

Current research shows that graphene fabrication is possible in many ways. As previously mentioned, the first method to isolate graphene was through mechanical exfoliation of bulk graphite. [22] Geim and Novoselov took a piece of bulk graphite, and with scotch tape, effectively "peeled" layers of graphite away from the source. Through subsequent peeling of these layers, few- or single-layer graphene could be exfoliated from graphite and then transferred onto a target substrate. The scotch tape could be removed or delaminated through a chemical wash, leaving behind isolated graphene. While a very cost-effective and simple method to isolate micron-scale regions of single- or few-layer graphene for research purposes, this method is unsuitable for commercial purposes to produce continuous monolayer or few-layer graphene films at lateral dimensions greater than ~10 microns. The volume of graphene produced here is miniscule, and methods to scale up this production have proven difficult and costly.[5] There are other methods to produce graphene currently under research or being widely used. They too, however, have significant drawbacks. One example is chemical vapour deposition (CVD),[24] a method by which gases react or decompose, often at a heated surface, creating a film of material on a substrate. In the production of graphene[24], this is a useful method to produce large area graphene (with lateral dimensions from $(1\ cm)^2$ to > $(50\ cm)^2$). For CVD to work, gases must be allowed to react at a catalytic substrate (on transitional metal catalysts such as nickel, copper, cobalt etc.), and this is where graphene monolayers (for Cu) or multilayers (for Ni) form. To examine pure, isolated graphene, it needs to be removed from the metal catalyst substrate, which can be an arduous process. Separation can be performed via dry or wet etching of the catalytic surface and transfer to a target substrate. However,many issues arise from CVD in graphene production; There is a significant risk of mechanical and chemical damage to the graphene layers. CVD is energy intensive, as substrates are heated to high temperatures. Vapours used can

present significant health risks. The substrate and gases need to be introduced in a sealed vacuum environment.[5] CVD can be an expensive prospect, in terms of instrumentation usage, maintenance, operator training, and post sample treatments.

In addition to Graphene, several other low-dimensional carbon nanomaterials have been discovered; From zero-dimensional fullerenes, one dimensional carbon nanotubes (CNT), and other two-dimensional carbon structures like carbon nanowalls. Fullerenes were first developed 1985 by researchers in Rice University and consist of spherical "cages" of carbon atoms[25] and are most widely used in medicine as an excipient for antibiotics and drugs, particularly in cancer treatments.[26,27] Carbon nanotubes are graphitic carbon structures, organised in a rolled up, tube structure, and can be characterised as single wall carbon nanotubes (SWNT), or multiwall carbon nanotubes (MWNT). MWNT first discovered in 1991[28], followed by SWNT in 1993 [29]. CNTs are often applied in fields such as engineering to make stronger lighter items, ranging from everyday commercial equipment like sports equipment, to construction where its widely used to strengthen concrete[30]. In addition, its unique chemical and electronic properties see its use in a wide range of fields, from filtration of air pollution and water filtration to electrical components such as electric motor brushes[31], light bulb filaments[32] and chemical nanowires[33]. Much of these low-dimensional carbon nanomaterials can also be constructed via techniques like CVD, and various other synthesis methods dependant on the structure required (arc-discharge, material pyrolysis, laser vaporisation).

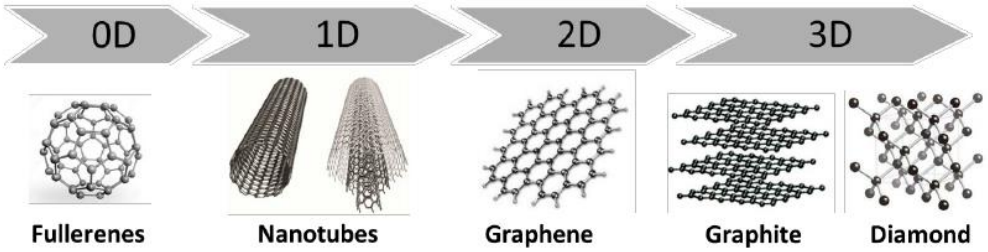


Figure 1.2 Low dimensional forms of carbon nanomaterials. [90]

One recent area of research in the fabrication of conductive graphitic structures is that of laser-induced graphene (LIG). By directing intense laser light onto a polymer, an insulating material can be converted into a highly conductive graphitic structure. LIG could arguably stem from research in 1980; Early methods describe the "creating of resistor material through localised heating of polymers".[34] Although research on this topic in this decade is brief, it does show the initial signs of interest in what would later be called LIG. In 2014, the current push toward LIG was initiated by James Tour's group at Rice University.[35] While attempting to laser reduce graphene oxide, they accidentally missed their intended target, and hit the surrounding polyimide. They noticed that by irradiating the polyimide with a CO_2 laser, it changed from its orange/yellow hue to an intense dark material. Raman spectroscopy investigtion showed that this material has similar properties to turbostratic graphite or few-layer graphene structures.

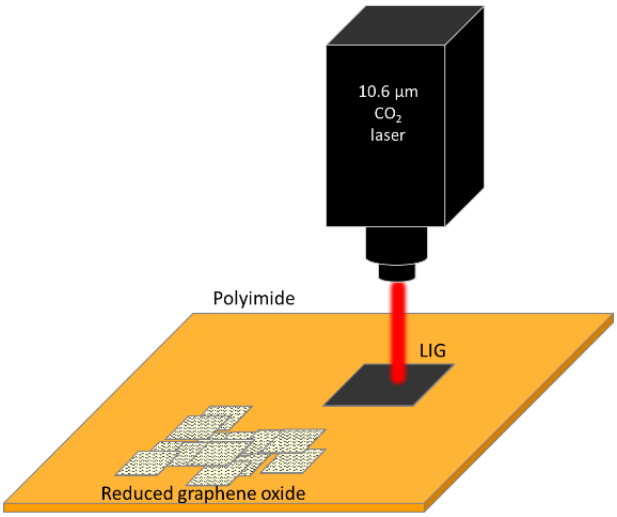


Figure 1.3 Schematic showing Tour's groups accidental discovery of LIG while attempting to laser reduced graphene oxide.

While the material formed was not of a similar standard to that of isolated graphene, as a method for creating conductive carbon structures, it proves particularly useful. One of the chief qualities to highlight being that this process is an additive method. While other fabrication methods produce bulk amounts of material, requiring a subtractive step, LIG converts only a specific region of target substrate into a conductive carbon structure. This reduces both the number of processing steps and waste material produced during fabrication. Combining this with the overall cost of production, the ease at which the method could be scaled up, and indeed the simplicity of the method of production itself, research into this material would prove extremely beneficial.

LIG in its current form is not without its own share of flaws. Despite using the word 'graphene' to describe it, it is more like a low dimensional graphitic structure. The structure is more similar to that of nano-graphene clusters[36], a structure which does have repeating units of hexagonally linked carbon atoms, but intermittent areas of disorder in the form of Stone–Wales defects, and defect atoms such as oxygen or

nitrogen laced throughout the material. However, this can prove beneficial, as this leads to the overall structure being porous, and having a high surface area.

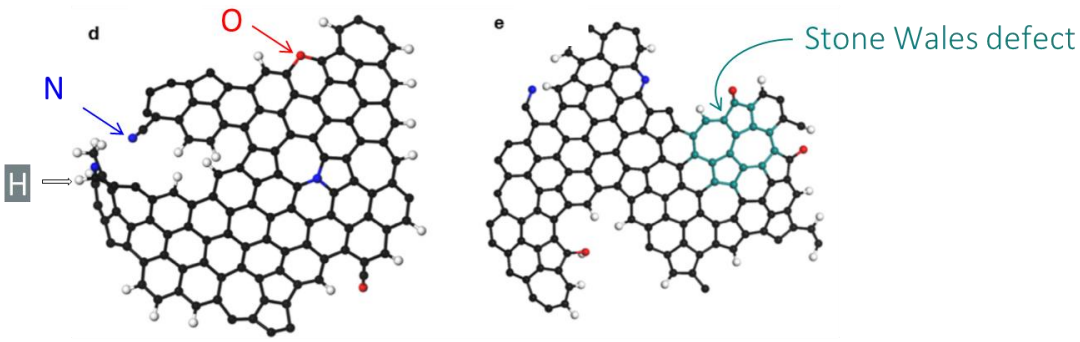


Figure 1.4 Molecular dynamics of polyimide under high pressure and high temperature forming nanographene clusters (LIG), showing the effects of both stone-wales defects, and non-carbon atoms on the 3D structure and curvarture of the clusters. [36]

Typically, LIG synthesis has been conducted using polyimide as a precursor material. Direct laser writing of commercial polyimide sheets (Kapton) provided an ideal target for graphitization. This was mostly performed utilizing infrared CO_2 laser systems, starting initially with controlled atmospheres.[37,38] This has progressed on to using other lasing systems and in ambient conditions. While the exact method of conversion remains under debate, the basic premise stands that through a thermal interaction of the intense laser photons with the polyimide structure, weaker bonds (such as C-H, C-O and C-N) are broken, and the components are released as a gas, while stronger bonds such as those arising from sp^2 bonds in C-C and C=C remain on the structure. This leaves a heavily carbonised region on the substrate.[26]

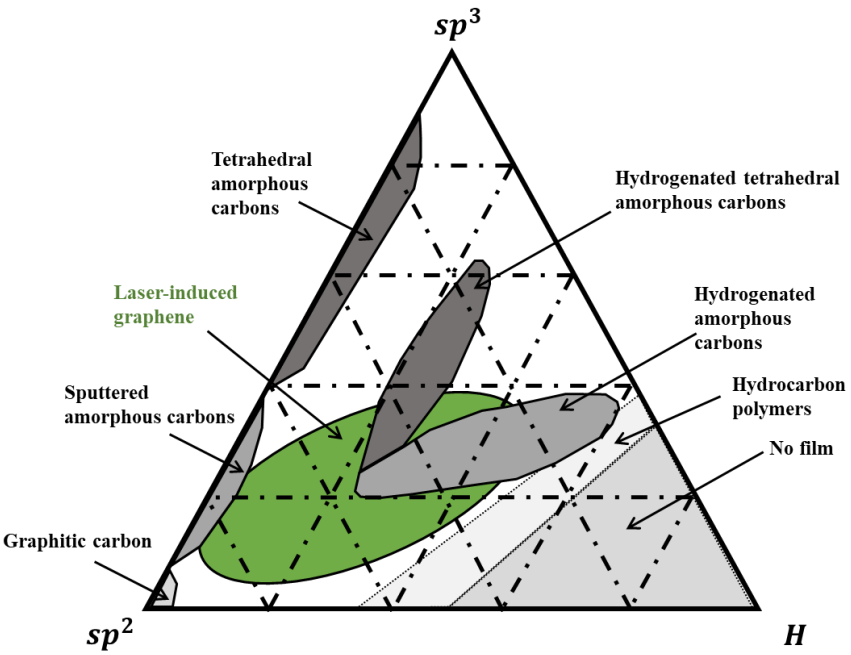


Figure 1.5 Ternary phase diagram of amorphous carbons. The three corners correspond to diamond-like carbon (sp^3) , graphitic carbon (sp^2) , and hydrocarbons (H). Green region demonstrates phases which LIG matrials can form.[96]

The two major theories about this interaction are that the reaction is either a photochemical or a photothermal effect. Photochemically, the photons from the laser source vibrate the specific bond with sufficient energy to separate the atoms. Photothermally, the photons from the laser source heats the entire structure, with the lighter elements outgassing, including some carbon atoms, the majority of which remain, forming the graphitised structure.[26,30] The method of conversion therefore can largely depend on the wavelength of the laser used. Shorter wavelength systems, (high photon energy) create photochemical processes, whereas longer wavelength (low photon energy) infared systems result in a photothermal effects. Depending on the laser source, feedstock material and process conditions, one of the two reaction routes can dominate the graphitisation. [35,39]

While most of the work on LIG has been focused on polyimide, a wide range of other plastics have been explored. However, polyimide acts as one of the easiest starting precursors for LIG. For example, polyether ether ketone (PEEK) can be converted to LIG, but only via modification of its surface, or through multiple lasing/ defocused lasing methods.[35,40] Many other plastics can be converted to LIG, but also require additional steps to reach complete conversion.[35,40] Polyimides base structure, combined with its thermal stability minimizes depolymerization and ablation of material, allowing for facile conversion into LIG structures.[40,41]

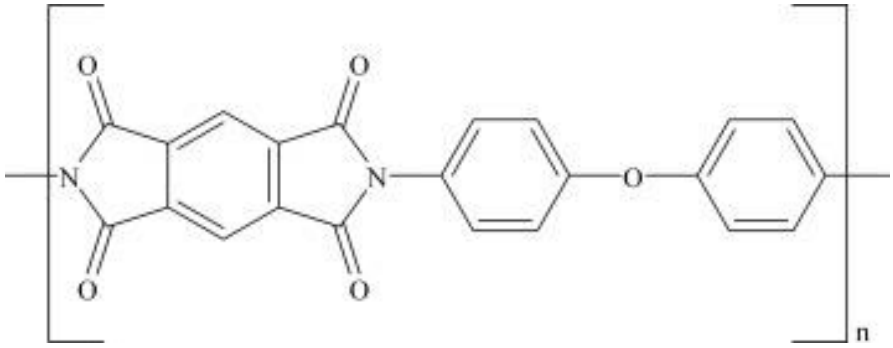


Figure 1.6 Chemical structure of polyimide. [94]

To circumvent difficulties encountered with other feedstock materials, several methods can be adapted to improve LIG yields. Performing laser graphitization in an inert environment prevents incineration of target material, allowing for direct conversion, and was widely used initially in the conversion of flammable materials such as bulk woods.[38,42] Multiple lasing passes allows for either pre-treatment of the target area or the gradual building of LIG structures.[40,43] This aids in converting easily ablated material by using a lower laser power over multiple scans, as opposed to one very high fluence scan. Conversely, for thermally stable materials, repeated exposure to a laser source allowed for gradual conversion from precursor to carbonised material to graphitised. Defocusing laser methods additionally are a means of controlling the delivered energy of a beam.[40,44,45] By purposely defocusing the laser, and increasing

the spot size of the laser beam, the energy density decreases reducing the chance of ablation. In addition, this method can also result in overlapping of laser target areas, resulting in some multiple lasing of areas occurring, further aiding the LIG conversion. The last and most extreme scenario is the modification of precursor materials via sample pre-treatment. Methodologies vary but most common are dehydration of samples via exposure to high temperatures[37], pre-carbonization of material via flame retardant treatment and exposure to direct flame[31], or inclusion of "dopants".[42,46,47]

Alternatives to plastics have also been examined, in the form of such materials as bulk woods, plants, foodstuffs, and cloths.[40,46,48] Many of these materials require the previously mentioned LIG methods (multi-lasing, defocusing atmosphere control etc.). This highlights the diversity this methodology can have, in building electrical components on any number of materials. For example, the conversion of LIG from foodstuffs shows promise in tackling the reduction of packaging of food items (on-product RFID tags for example, as opposed to part of packaging), or in wearable and flexible sensing applications[40,49,50] (i.e. strain or stress sensors on clothing items). Investigations towards a more sustainable precursor to this point have mostly been focused on the conversion of bulk wood products (i.e. Pine, cork and cedar as potential target material[42,51,52]). Lately, however, the growing interest in the development of bioplastics and biopolymers opens new avenues for sustainable laser-graphene fabrication processes.

Recently there has been a major drive towards bioplastics, and other biodegradable plastic alternatives. Traditional polymers, in particular petrochemical-based plastics, tend to have detrimental effects on the environment as a whole.[53–57] From the source of their raw materials, fabrication methods, and disposal after use, the combined impact on animal ecology, energy usage, and overall carbon footprint,

presents a huge concern. Currently, around 250 million tonnes of plastic are produced globally per annum[54], with an estimated 8.3 billion tonnes produced since the 1950s, and an estimated 60% of which are currently located in landfills, or in the natural environment.[58]

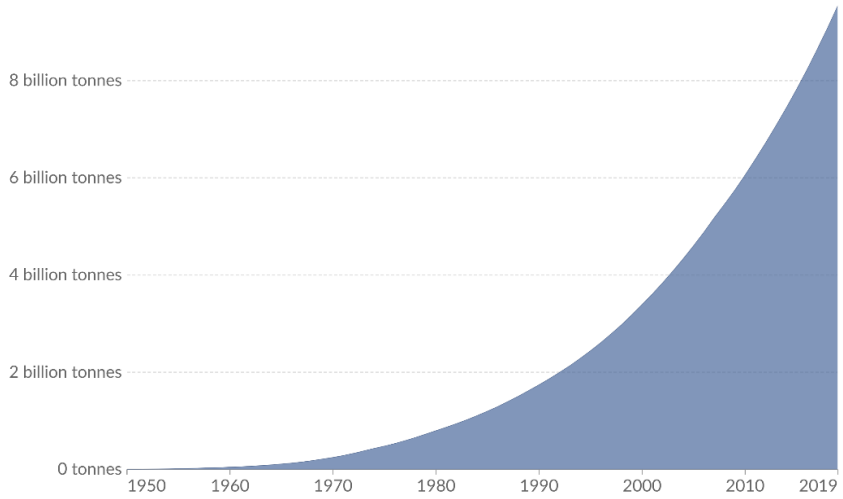


Figure 1.7 Cumlative global plastic production, for the years 1950-2019, revealing the massive increase of plastic usage over time. [92]

This presents an additional issue as plastic lifespan; their degradation is extremely long, particularly concerning their general short term uses[56,58] (e.g. single-use plastics in food packaging). Dependant on the type of plastic (i.e., PET, HDPE, PVC) and the structure it is in (i.e., Film, fibre, beads), where it is deposited at end of life (i.e., landfill or marine environments), and if the degradation process is assisted (i.e., UV-treated, thermal treated, or microbe incubation) complete plastic degradation can take anywhere from 2 years to over 2000 years.[53,59,60] This longevity presents significant problems in terms of occupied space, health hazards to animal life, and potential toxicity to land and marine environments for general use. This issue arises from the fact that plastics are designed to be both mechanically and chemically inert. While this is potentially beneficial for such applications as packaging, as it can prevent

goods from spoiling due to exposure to external elements, and maintain a longer shelf life, it becomes detrimental when dealing with plastic waste.

Other solutions to these are available but present their own disadvantages. Recycling said plastics can extend their potential usage. However, the scope of what can be recycled is limited, and indeed even for widely recycled plastics issues such as contamination, varying types of plastic, and inability to reach a complete recycle loop (plastic recycled indefinitely).[54,55] This results in certain estimations that only 30% of plastic sent for recycling manages to be recycled, with only 9% of total plastic waste actual in total being full recycled.[58] An alternative to both recycling and landfill is incineration. This effectively removes the usage of substantial amounts of land for landfills, and gives the plastic a definite endpoint, as opposed to general disposal and recycling. Incineration can also provide some energy production and recovery, from the heat/gases produced.[54] However, incineration directly releases a large number of harmful compounds into the atmosphere, not limited to just greenhouse gases which rapidly impact climate change, but also potentially harmful and toxic gases, depending on the materials consumed in the incinerator.[53]

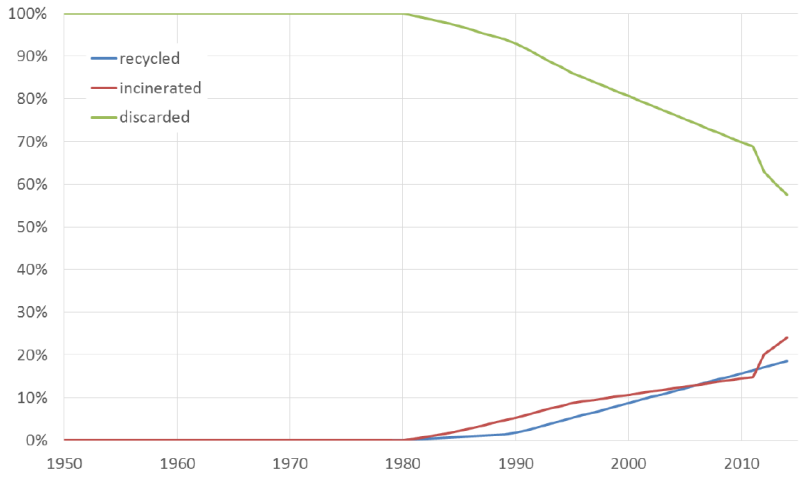


Figure 1.8 Global plastic waste by disposal, for the years 1950-2015. [92]

Bioplastics provide a more environmentally friendly alternative to traditional petrochemical-based plastics. It should be noted, that despite the pitfalls previously mentioned regarding plastics, its use as a material for a wide variety of applications is extremely beneficial, particularly in fields such as packaging. Therefore, an ideal material would simulate some of the properties of plastics, while being environmentally friendly. Bioplastics can be characterised by three categories: plastics fabricated from non-petrochemical, sustainable and natural substrates. Biodegradable plastics. Or a combination of both sets.[61] The latter being the most ideal situation.

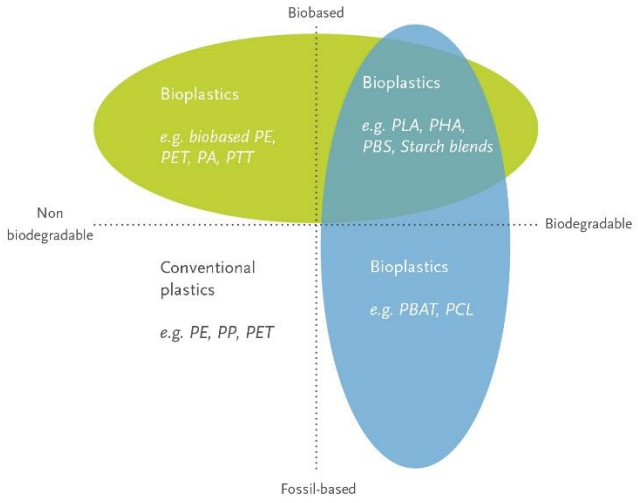


Figure 1.9 Diagram of the breakdown of varying types of bioplastics.[95]

Initial bioplastic research technically pre-dates the invention of most common modern-day petrochemical-based plastics. The late 19th century saw many efforts towards the invention of plastics as a whole. Parkesine is often cited as the first man-made bioplastic, derived from cellulose, and was invented by Alexander Parkes in 1862.[62] While not still widely used, an improved version of it, celluloid, invented by John Wesley Hyatt in 1869[62], is still widely used to this day. 1897 saw the arrival of galalith, a biodegradable plastic derived from casein, invented by Adolf Spitteler.[63] The arrival of modern plastics, and the difficulty of production, saw galalith become

outmoded, however, which current day uses being small productions, for example, shirt buttons.

The arrival of synthetic plastic, however, diminished the interest in bioplastics. 1907 saw the first synthetic plastic, in the form of bakelite, invented by Leo Baekeland.[64] Bakelite being very adaptable saw a wide range of uses and encouraged the development of other plastics of its kind. This would eventually lead to the development of petrochemical polymers in the early to mid-20th century, such examples including polyethylene, polystyrene, and nylon. The success of these polymers and corresponding plastics of its type left research into bioplastics stagnant until later in the 20th century.

Despite this, many bioplastics still in use today found their start during the synthetic plastic boom. Cellophane, derived from cellulose, was patented in 1912.[65] This transparent, thin, sheet plastic is still widely used to this day in food packaging. PVC(PHB), the first bioplastic made from bacteria, was developed in 1926.[66] It saw a wide range of uses from biomedical in the form of sutures, and stitches, to single-use plastic materials like bags, bottles, and other food ware. Polylactic Acid (PLA) was also developed in the 1920s, however, the production cost to develop it as a useful product was initially deemed too expensive. In recent years, interests in bioplastics have seen its re-emergence, particular in use as a more environmentally friendly method for producing single-use plastics.[61,67,68]

In recent years, bioplastics have seen a significant increase in interest. Initially, this was driven by limited access to petrochemical sources, due to both sources becoming depleted, and trade embargos as a result of diplomatic issues in the middle east particularly around the 1970s.[69–71] Currently, the extra pressure emerging from

both climate change, and the environmental impact of plastics, has seen a significant increase in research in bioplastics[55,72,73] (such as the aforementioned PLA).

Cellulose continues to be the key biopolymer of interest when it comes to bioplastic research. This is chiefly due to cellulose's abundance, as it is cited as the most common biopolymer in existence.[76] Cellulose provides the main structure for plant cell walls and provides the structure for most plant fibres. As cellulose comes from a wide range of readily available sources (wood from trees, cotton, flax, and any other plant fibres) that are sustainable to reproduce, cellulose is extremely beneficial as a starting point for most bioplastics research. As previously mentioned, cellulose was already widely adopted in the forms of celluloid and nitro-cellulose[62], initially derived from cotton. Current cellulose research is geared toward the application of other sources, from bulk woods[75,76], to algae,[77,78]widening the sustainability options.

Examining other cellulose sources also expands the number of other biopolymers to be examined. For example, bulk woods, which provide an excellent source of cellulose, also contains many other biopolymers with them. Lignin is one such biopolymer, which is one of three common polymers in wood and other plant life (including cellulose and hemicellulose).[79] Lignin acts as the connecting polymer in plant life between the main cellulose and hemicellulose structures. In bioplastic research, lignin has mostly been co-opted into other bioplastics as a reinforcing agent. Composites with lignin include such common bioplastics as PLA, PHB and cellulose-based bioplastics.[80]

Chitosan is another biopolymer that shows great promise in the field of bioplastics and is the key bioplastic explored later in this thesis. Chitosan is the acetylated form of chitin, the main component of most hard shell and exoskeleton containing wildlife, such as shrimp, crabs, and insects.[81] As such, it is often cited as

the second most abundant polysaccharide[82], after cellulose. Similarly to cellulose, these advantages of abundance and a readily available sustainable source have increased its interest. Currently, chitosan has seen many possible applications explored,e.g., food packaging[83,84], medical[81,85] and cosmetic uses.[82,86]

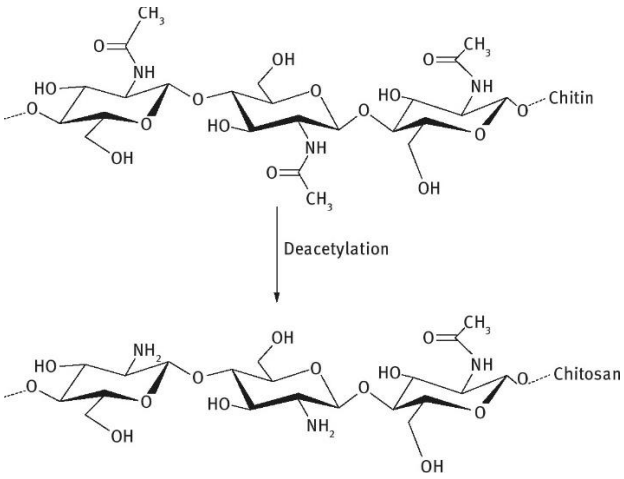


Figure 1.10 Chemical structures of chitin, and its de-acetylated form, chitosan. [92]

The majority of LIG based investigations on bioplastic composites have been focused mainly on cellulose and lignin-based bioplastic and variations therein. Arguably this arises from previous success from LIG conversion of bulk wood products as described earlier, and from the abundance, in particular of cellulose, of their sources. This has been shown through applications such as flexible supercapacitors.[87–89] This shows, however, that there is a potential gap in the community for exploring not only other applications, but also exploring other bioplastics, and sustainable substrates.

In terms of LIG fabrication, bioplastics have not been widely explored. As previously mentioned, the majority of sustainability targets for LIG have been on bulk woods, with some work on cloth, paper, and foodstuffs. There is however a developing interest in the use of bioplastic in this field, mostly toward plant-based biopolymers, such as those derived from cellulose and lignin.

1.2 Thesis Overview

In this thesis, the potential of using LIG, with reference to its ability to be a sustainable and environmentally friendly method of fabrication will be explored. This will be achieved by material characterisation and demonstrated through proof-of-concept application of LIG based sensors. Initially exploring a less intensive method of producing LIG via diode lasers on polyimide, before exploring its application on a more sustainable substrate in the form of chitosan bioplastic composites. This will then all cumulate into an examination of a potential application of a chitosan-based laser-induced graphene gas sensing platform.

In chapter two, a low-cost means of producing LIG on polyimide is explored, via a 405-nanometre diode laser. By using a diode laser, as opposed to a larger industrial level laser, we show that LIG can be produced much more economically, and environmentally friendly means. this chapter acts as a brief introduction to LIG production and characterisation before its application on sustainable bioplastics. In addition, this chapter explores LIGs' potential as an electrochemical sensor material.

Personal contribution to chapter two:

- Electrode fabrication: Design and fabrication of LIG electrodes.
- Characterisation and analysis.
    - Scanning electron and optical microscopy.
    - Profilometry measurements.
    - Two-terminal current-voltage measurements.
    - Raman spectroscopy: measuring fitting, and analysis.
    - Electrochemical measurments.
- Manuscript drafting and authoring.

Chapter three begins to explore LIG on sustainable substrates, namely a chitosan-based composite. Here we see the increase in complexity in laser-induced fabrication, in comparison to that of polyimide-based LIG. Chapter three follows on from the work in chapter two utilizing similar characterisation methods. As an alternative to polyimide (a nonsusitainable, petrochemcial based plastic) based LIG, this chapter highlights the benefits of sustainable and compostable sensing material. This is particularly notable in the latter half of the chapter, where the potential application of the chitosan-based LIG is used to form electrochemical sensors.

Personal contributions to chapter three:

- Device fabrication
    - Chitosan film formulation: Optimisation, and preparation
    - Laser graphitization of chitosan film
- Characterisation and analysis
    - Sample preperation for all characterisation steps.
    - Scanning electron and optical microscopy.
    - Two-terminal current-voltage measurements.
    - Electrochemical measurements.
    - Raman spectroscopy: measuring fitting, and analysis.
- Data analysis
    - Tranmission electron microscopy.
    - Thermogravometric analysis.
    - Fourier transform infared spectroscopy.
- Manuscript drafting and authoring.

This work is then continued into chapter four, where a potential application of the chitosan-based LIG is widely explored. Here chitosan-based LIG is used to form 2-terminal impedance style sensors for humidity and volatile organic compounds.

Personal contribution to chapter four:

- Device fabrication
    - Chitosan film preparation
    - Device design
    - Laser graphitization
- Characterisation and analysis
    - Scanning electron microscopy
    - Optical microscopy
    - Flourecnece microscopy
- Humidity and gas sensing
    - Assisted in experimental design
    - Humidity sensing measurements
    - Solvent sensing measurments
- Manuscript drafting and authoring

Finally, in chapter five, the work of the previous chapters is reflected on. Here the future of this work is explored, examining possible commercial applications, and comments on the limitations and advantages of the material going forward.

1.3 References

[1] A. H. Castro Neto, F. Guinea, N. M. R. Peres, K. S. Novoselov, A. K. Geim, *Rev. Mod. Phys.* **2009**, *81*, 109.

[2] A. A. Balandin, S. Ghosh, W. Bao, I. Calizo, D. Teweldebrhan, F. Miao, C. N. Lau, *Nano Lett.* **2008**, *8*, 902.

[3] C. Lee, X. Wei, J. W. Kysar, J. Hone, Science (80-.). 2008, 321, 385.

[4] G. Wang, J. Yang, J. Park, X. Gou, *J. Phys. Chem. C* **2008**, *112*, 8192.

[5] C. Soldano, A. Mahmood, E. Dujardin, *Carbon N. Y.* **2010**, *48*, 2127.

[6] D. Beloin-Saint-Pierre, R. Hischier, *Int. J. Life Cycle Assess.* **2021**, *26*, 327.

[7] X. J. Lee, B. Y. Z. Hiew, K. C. Lai, L. Y. Lee, S. Gan, S. Thangalazhy-Gopakumar, S. Rigby, *J. Taiwan Inst. Chem. Eng.* **2019**, *98*, 163.

[8] L. Serrano-Luján, S. Víctor-Román, C. Toledo, O. Sanahuja-Parejo, A. E. Mansour, J. Abad, A. Amassian, A. M. Benito, W. K. Maser, A. Urbina, *SN Appl. Sci.* **2019**, *1*, 1.

[9] T. Davids, *The History of Ink: Including Its Etymology, Chemistry and Bibliography*; T. Davids & Company, 1860: Michigan, 1860.

[10] E. H. VOICE, *Trans. Newcom. Soc.* **1949**, *27*, 131.

[11] P. Delhaes, *Graphite and Precursors*; Delhaes, P., Ed.; CRC Press, 2000.

[12] T. Novakov, V. Ramanathan, J. E. Hansen, T. W. Kirchstetter, M. Sato, J. E. Sinton, J. A. Sathaye, *Geophys. Res. Lett.* **2003**, *30*, 1.

[13] R. D. Singh, *Principles and Practices of Modern Coal Mining*; Reprint.; New Age International: New Delhi, 2005.

[14] R. L. Galloway, *A History of Coal Mining in Great Britain*; Macmillan and Company, 1882: Oxford, 1882.

[15] G. Ruess, F. Vogt, *Monatshefte f*[illegible]*r Chemie* **1948**, *78*, 222.

[16] L. Spanu, S. Sorella, G. Galli, *Phys. Rev. Lett.* **2009**, *103*, 1.

[17] R. Adler, C. Kang, Y. Chen, S. Fan, T. Gould, **1994**.

[18] L. Pauling, *Proc. Natl. Acad. Sci.* **1966**, *56*, 1646.

[19] K. S. Kim, Y. Zhao, H. Jang, S. Y. Lee, J. M. Kim, K. S. Kim, J. H. Ahn, P. Kim, J. Y. Choi, B. H. Hong, *Nature* **2009**, *457*, 706.

[20] B. C. Brodie, *Philos. Trans. R. Soc. London* **1859**, *149*, 249.

[21] P. R. Wallace, *Phys. Rev.* **1947**, *71*, 622.

[22] K. S. Novoselov, A. K. Geim, S. V Morozov, D. Jiang, Y. Zhang, S. V. Dubonos, I. V Grigorieva, A. A. Firsov, *Science (80-.).* **2004**, *5*, 1.

[23] The Royal Swedish Academy of Sciences, **2010**. *The Nobel Prize in Physics 2010*. [online] Available at: <https://www.nobelprize.org/prizes/physics/2010/press-release/> [Accessed 7 October 2022].

[24] G. Kalita, M. Tanemura, *Fundamentals of Chemical Vapor Deposited Graphene and Emerging Applications*; 2017.

[25] H. W. Kroto, J. R. Heath, S. C. O'Brien, R. F. Curl, R. E. Smalley, *Nature* **1985**, *318*, 162.

[26] R. Bakry, R. M. Vallant, M. Najam-ul-Haq, M. Rainer, Z. Szabo, C. W. Huck, G. K. Bonn, *Int. J. Nanomedicine* **2007**, *2*, 639.

[27] Chun-Mao Lin, Tan-Yi Lu, *Recent Pat. Nanotechnol.* **2012**, *6*, 105.

[28] S. Iijima, *Nature* **1991**, *354*, 56.

[29] S. Iijima, T. Ichihashi, *Nature* **1993**, *363*, 603.

[30] Z. Shariatinia, *Handb. Carbon-Based Nanomater.* **2021**, 321.

[31] G. Toth, J. Mäklin, N. Halonen, J. Palosaari, J. Juuti, H. Jantunen, K. Kordas, W. G. Sawyer, R. Vajtai, P. M. Ajayan, *Adv. Mater.* **2009**, *21*, 2054.

[32] J. Wei, H. Zhu, D. Wu, B. Wei, *Appl. Phys. Lett.* **2004**, *84*, 4869.

[33] X. P. Gao, Y. Zhang, X. Chen, G. L. Pan, J. Yan, F. Wu, H. T. Yuan, D. Y. Song, *Carbon N. Y.* **2004**, *42*, 47.

[34] D. M. Daniel, L. Mesa, M. Conny, S. Diego, E. Robert, US . Patent Apr . 22 , 1986 **1986**.

[35] J. Lin, Z. Peng, Y. Liu, F. Ruiz-Zepeda, R. Ye, E. L. G. Samuel, M. J. Yacaman, B. I. Yakobson, J. M. Tour, *Nat. Commun.* **2014**, *5*, 1.

[36] Y. Dong, S. C. Rismiller, J. Lin, *Carbon N. Y.* **2016**, *104*, 47.

[37] D. X. Luong, K. Yang, J. Yoon, S. P. Singh, T. Wang, C. J. Arnusch, J. M. Tour, *ACS Nano* **2019**, *13*, 2579.

[38] Y. Li, D. X. Luong, J. Zhang, Y. R. Tarkunde, C. Kittrell, F. Sargunaraj, Y. Ji, C. J. Arnusch, J. M. Tour, *Adv. Mater.* **2017**, *29*, 1.

[39] R. Srinivasan, B. Braren, R. W. Dreyfus, *J. Appl. Phys.* **1987**, *61*, 372.

[40] Y. Chyan, R. Ye, Y. Li, S. P. Singh, C. J. Arnusch, J. M. Tour, *ACS Nano* **2018**, *12*, 2176.

[41] F. J. Romero, A. Salinas-Castillo, A. Rivadeneyra, A. Albrecht, A. Godoy, D. P. Morales, N. Rodriguez, *Nanomaterials* **2018**, *8*, 1.

[42] X. Han, R. Ye, Y. Chyan, T. Wang, C. Zhang, L. Shi, T. Zhang, Y. Zhao, J. M. Tour, *ACS Appl. Nano Mater.* **2018**, *1*, 5053.

[43] S. Lee, S. Jeon, *ACS Sustain. Chem. Eng.* **2019**, *7*, 2270.

[44] J. U. Lee, Y. W. Ma, S. Y. Jeong, B. S. Shin, *Micromachines* **2020**, *11*.

[45] S. Lee, H. Jang, H. Lee, D. Yoon, S. Jeon, *ACS Appl. Mater. Interfaces* **2019**, *11*, 26970.

[46] T. S. D. Le, S. Park, J. An, P. S. Lee, Y. J. Kim, *Adv. Funct. Mater.* **2019**, *29*, 1.

[47] Z. Zhang, M. Song, J. Hao, K. Wu, C. Li, C. Hu, *Carbon N. Y.* **2018**, *127*, 287.

[48] R. Ye, Y. Chyan, J. Zhang, Y. Li, X. Han, C. Kittrell, J. M. Tour, *Adv. Mater.* **2017**, *29*, 1.

[49] F. Tehrani, M. Beltrán-Gastélum, K. Sheth, A. Karajic, L. Yin, R. Kumar, F. Soto, J. Kim, J. Wang, S. Barton, M. Mueller, J. Wang, *Adv. Mater. Technol.* **2019**, *1900162*, 1.

[50] M. G. Stanford, K. Yang, Y. Chyan, C. Kittrell, J. M. Tour, *ACS Nano* **2019**, *13*, 3474.

[51] R. Trusovas, K. Ratautas, G. Račiukaitis, G. Niaura, *Appl. Surf. Sci.* **2019**, *471*, 154.

[52] A. Imbrogno, J. Islam, C. Santillo, R. Castaldo, L. Sygellou, C. Larrigy, R. Murray, E. Vaughan, M. K. Hoque, A. J. Quinn, D. Iacopino, *ACS Appl. Electron. Mater.* **2022**, acsaelm.1c01202.

[53] H. K. Webb, J. Arnott, R. J. Crawford, E. P. Ivanova, *Polymers (Basel).* **2013**, *5*, 1.

[54] J. Hopewell, R. Dvorak, E. Kosior, *Philos. Trans. R. Soc. B Biol. Sci.* **2009**, *364*, 2115.r

[56] A. Dormer, D. P. Finn, P. Ward, J. Cullen, *J. Clean. Prod.* **2013**, *51*, 133.

[57] J. G. B. Derraik, *Mar. Pollut. Bull.* **2002**, *44*, 842.

[58] R. Geyer, J. R. Jambeck, K. L. Law, *Sci. Adv.* **2017**, *3*, 25.

[59] A. Chamas, H. Moon, J. Zheng, Y. Qiu, T. Tabassum, J. H. Jang, M. Abu-Omar, S. L. Scott, S. Suh, *ACS Sustain. Chem. Eng.* **2020**, *8*, 3494.

[60] A. L. Andrady, *Mar. Pollut. Bull.* **2011**, *62*, 1596.

[61] S. Pathak, C. L. R. Sneha, B. B. Mathew, **2014**, *2*, 84.

[62] S. C. Rasmussen, *Angew. Chemie - Int. Ed.* **2021**, *60*, 8012.

[63] V. B. Gerritsen, *Bioinformatics* **2001**.

[64] L. H. Baekeland, *Ind. Eng. Chem.* **1909**, *1*, 149.

[65] P. Van Inskeep, Gordon C and Horn, *Ind. Eng. Chem.* **1952**, *44*, 2511_2524.

[66] M. N. Belgacem, A. Gandini, *Monomers, Polymers and Composites from Renewable Resources*; Elsevier Science, 2008.

[67] N. Jabeen, I. Majid, G. A. Nayik, *Cogent Food Agric.* **2015**, *1*, 1.

[68] A. Di Bartolo, G. Infurna, N. T. Dintcheva, *Polymers (Basel).* **2021**, *13*.

[69] O. J. Blanchard, J. Gali, *Natl. Bur. Econ. Res. no. 15467* **2007**, Cambridge.

[70] F. Venn, *The oil crisis*; Taylor \& Francis, 2016.

[71] A. U. B. Queiroz, F. P. Collares-Queiroz, *Polym. Rev.* **2009**, *49*, 65.

[72] S. M. Emadian, T. T. Onay, B. Demirel, *Waste Manag.* **2017**, *59*, 526.

[73] I. Muhammad Shamsuddin, *Adv. Biosci. Bioeng.* **2017**, *5*, 63.

[74] D. Klemm, B. Heublein, H. P. Fink, A. Bohn, *Angew. Chemie - Int. Ed.* **2005**, *44*, 3358.

[75] G. Chen, Z. Wu, Z. Shen, H. Y. Li, J. Li, B. Lü, G. Song, X. Gong, M. Qin, C. L. Yao, F. Peng, *Chem. Eng. J.* **2022**, *439*, 135680.

[76] G. Tedeschi, S. Guzman-Puyol, L. Ceseracciu, U. C. Paul, P. Picone, M. Di Carlo, A. Athanassiou, J. A. Heredia-Guerrero, *Biomacromolecules* **2020**, *21*, 910.

[77] J. W. Roy Chong, X. Tan, K. S. Khoo, H. S. Ng, W. Jonglertjunya, G. Y. Yew, P. L. Show, *Environ. Res.* **2022**, *206*, 112620.

[78] E. Zanchetta, E. Damergi, B. Patel, T. Borgmeyer, H. Pick, A. Pulgarin, C.

Ludwig, *Algal Res.* **2021**, *56*, 102288.

[79] A. M. Olsson, L. Salmén, *Nord. Pulp Pap. Res. J.* **1997**, *12*, 140.

[80] J. Yang, Y. C. Ching, C. H. Chuah, *Polymers (Basel).* **2019**, *11*, 1.

[81] M. Dash, F. Chiellini, R. M. Ottenbrite, E. Chiellini, Chitosan - A versatile semi-synthetic polymer in biomedical applications. *Prog. Polym. Sci.* **2011**, *36*, 981–1014.

[82] M. Rinaudo, *Prog. Polym. Sci.* **2006**, *31*, 603.

[83] H. Dong, L. Cheng, J. Tan, K. Zheng, Y. Jiang, *J. Food Eng.* **2004**, *64*, 355.

[84] P. J. Chien, F. Sheu, F. H. Yang, *J. Food Eng.* **2007**, *78*, 225.

[85] E. Szymańska, K. Winnicka, *Mar. Drugs* **2015**, *13*, 1819.

[86] C. R. Afonso, R. S. Hirano, A. L. Gaspar, E. G. L. Chagas, R. A. Carvalho, F. V. Silva, G. R. Leonardi, P. S. Lopes, C. F. Silva, C. M. P. Yoshida, *Int. J. Biol. Macromol.* **2019**, *132*, 1262.

[87] F. Mahmood, H. Zhang, J. Lin, C. Wan, *ACS Omega* **2020**, *5*, 14611.

[88] S. Wang, Y. Yu, S. Luo, X. Cheng, G. Feng, Y. Zhang, Z. Wu, G. Compagnini, J. Pooran, A. Hu, *Appl. Phys. Lett.* **2019**, *115*.

[89] F. Mahmood, C. Zhang, Y. Xie, D. Stalla, J. Lin, C. Wan, *RSC Adv.* **2019**, *9*, 22713.

[90] O. Kanoun, C. Müller, A. Benchirouf, A. Sanli, T. N. Dinh, A. Al-Hamry, L. Bu, C. Gerlach, A. Bouhamed, *Sensors (Switzerland)* **2014**, *14*, 10042.

[91] R. Ye, D. K. James, J. M. Tour, *Adv. Mater.* **2019**, *31*, 1.

[92] N. Berezina, Phys. Sci. Rev. 2016, 1, 1.

[92] R. Geyer, J. R. Jambeck, K. L. Law, *Sci. Adv.* **2017**, *3*, 25.

[93] A. Kumar, C. Huei, *Adv. Graphene Sci.* **2013**.

[94] L. W. McKeen, In *The Effect of Long Term Thermal Exposure on Plastics and Elastomers*; McKeen, L. W., Ed.; William Andrew Publishing, 2014; pp. 117–137.

[95] B. L. Ottoni, R. M. Deus, J. A. Gobbo Junior, Â. M. G. de Carvalho, R. A. G. Battistelle, *J. Appl. Packag. Res.* **2018**, *10*, 10.

[96] A. C. Ferrari, J. Robertson, *Phys. Rev. B - Condens. Matter Mater. Phys.* **2000**, *61*.

Chapter 2: Fabrication and Electrochemical Properties of Three-Dimensional (3D) Porous Graphitic and Graphene like Electrodes Obtained by Low-Cost Direct Laser Writing Methods

As published in:

ACS Omega 2020, 5, 3, 1540–1548 Publication Date: January 10, 2021 https://doi.org/10.1021/acsomega.9b03418

Author list:

Micheal Burke, Cathal Larrigy, Eoghan Vaughan, George Paterakis, Labrini Sygellou, Aidan J. Quinn, Grégoire Herzog, Costas Galiotis, and Daniela Iacopino

2.1 Abstract

The development of three-dimensional (3D) porous graphitic structures is of great interest for electrochemical sensing applications as they can support fast charge transfer and mass transport through their extended, large surface area networks. In this work we present the facile fabrication of conductive and porous graphitic electrodes by direct laser writing techniques. Irradiation of commercial polyimide sheets (Kapton tape) was performed with a low-cost laser engraving machine with visible excitation wavelength (405 nm) at low power (500 mW) leading to formation of 3D Laser Induced Graphene (LIG) structures. Systematic correlation between applied laser dwell time per pixel ("dwell time") and morphological/structural properties of fabricated electrodes showed that conductive and highly 3D porous structures with spectral signatures of nanocrystalline graphitic carbon materials were obtained at laser dwell times between 20 and 110 ms/pix, with graphene-like carbon produced at 50 ms/pix dwell time, with comparable properties to LIG obtained with high-cost CO_2 lasers. Electrochemical characterization with inner and outer sphere mediators showed fast electron transfer rates, comparable to previously reported 2D/3D graphene-based materials and other graphitic carbon electrodes. This work opens the way to the facile fabrication of low-cost, disposable electrochemical sensor platforms for de-centralized assays.

2.2 Introduction

Graphitic and graphene-like materials are intensively studied due to their unique physical and chemical properties which can be exploited for fabrication of electrochemical sensors and biosensors.[1-3] The interest towards these materials for sensing applications arises from the possibility of tuning their analytical performance by controlling structure, morphology, porosity and surface functionalities of the carbon electrodes, as all the above chemico-physical parameters have a direct impact on the electron transfer rate. For example, it is known that graphite basal and edge planes possess different surface morphologies and that electron transfer kinetics are greatly enhanced at graphene edge sites, due to high density of defects and corrugations.[1] Moreover, it has been reported that the use of porous graphene 3D structures can lead to enhanced electrochemical responses, associated to availability of highly conducting pathways providing high mass transport and charge transfer rates.[4,5] Therefore, the realization of high performance electrochemical sensors requires availability of large mass two-dimensional (2D) graphitic materials extending into large porous 3D networks. This process is usually achieved by application of costly (chemical vapor deposition, CVD),[6] cumbersome (spray coating),[7] or inefficient (self-assembly of reduced graphene oxide) techniques.[8] Another issue is that the complex solution processing of graphene-like materials leads to aggregated graphene sheets with dramatically reduced surface area and therefore reduced electrochemical activity.[9] Therefore, the development of straightforward fabrication methods enabling high-throughput, low-cost and large scale fabrication of 3D graphene-based electrodes under ambient conditions is a technologically important goal for the realization of highly sensitive electrochemical sensors. Recently, porous graphitic structures have been obtained by direct laser writing methods on commercial polyimide sheets

(Kapton tape). For example, extended 3D graphitic structures (Laser Induced Graphene, LIG) were patterned on polyimide by simple direct writing with CO_2 laser irradiation under ambient conditions.[10-13] The formation of LIG was ascribed to the generation of local high temperatures induced by a resonance effect between the laser wavelength and the polyimide, which caused carbonization and subsequent graphitization of polyimide. During this process the polyimide sp^3-carbon atoms were photo-converted in sp^2–carbon atoms by pulsed laser irradiation. Atoms from broken C-H, C-O, C=O and C-N bonds were released as gas, thus contributing to porous structure formation. In addition, as the process occurred at ambient conditions, the fast release of locally available, hydrogen, oxygen and water in form of H_2, CO and CO_2 gases resulted in formation of highly porous structures.[10] The main application of LIG materials so far has been in the field of energy storage, whereby LIG structures were successfully used as electrodes for fabrication of low cost and flexible supercapacitors.[10-12] However, recently reports of LIG electrodes for demonstration of on-chip electrochemical sensing have also emerged.[14,15] For example, Nakak *et al.* found that the morphology of LIG, rich in defect and edge plane sites and functional enough to be wetted by aqueous electrolytes, was particularly amenable to electrochemical sensing applications and reported high electro-catalytic activity and high sensitivity towards ascorbic acid, dopamine and uric acid.[14] The same authors also demonstrated sensitive (5 pM in serum) bio-detection by aptamer bio-functionalization of LIG.[16] Also Cardoso *et al.* showed fabrication of molecularly-imprinted chloramphenicol sensors on LIG electrodes.[17] The variety of applications and the simplicity of instrumentation (laser engraving machine operating under ambient conditions) and precursor materials (commercial Kapton tape) required to make such electrodes, suggest that LIG could be used for the large scale fabrication of disposable electrochemical sensors for decentralized assays (point-of-care, in situ

monitoring). Towards this end, LIG structures were recently obtained by the use of visible laser sources and demonstration of biogenic amines in food samples achieved.[18-20] This is a desirable development towards further reduction of production costs. However, the use of 405 nm lasers required pre- or post-electrode doping in order to show satisfactory applications.

In this paper we present the fabrication of porous, conductive and 3D graphitic electrodes obtained by direct writing of polyimide sheets under ambient conditions with a low-cost laser engraving tool equipped with a 405 nm irradiation wavelength laser diode. As the irradiation power of this laser source was fixed at 500 mW, a detailed investigation of the correlation between applied dwell times and the resulting morphological, structural, electrical and electrochemical characteristics of obtained LIG electrodes was performed. It was found that dwell times in the range 40 – 60 ms/pix led to formation of conductive, porous structures with nanocrystalline graphitic carbon spectral signatures, evidenced by Raman and X-ray photoelectron spectroscopy (XPS) data. The electrochemical properties of LIG electrodes were tested with inner- and outer-sphere redox mediators and showed fast electron transfer (ET) kinetics and heterogeneous electron transfer rates (HET) comparable to other graphene-based materials and edge plane pyrolytic graphite (EPPG).

2.3 Results and Discussion

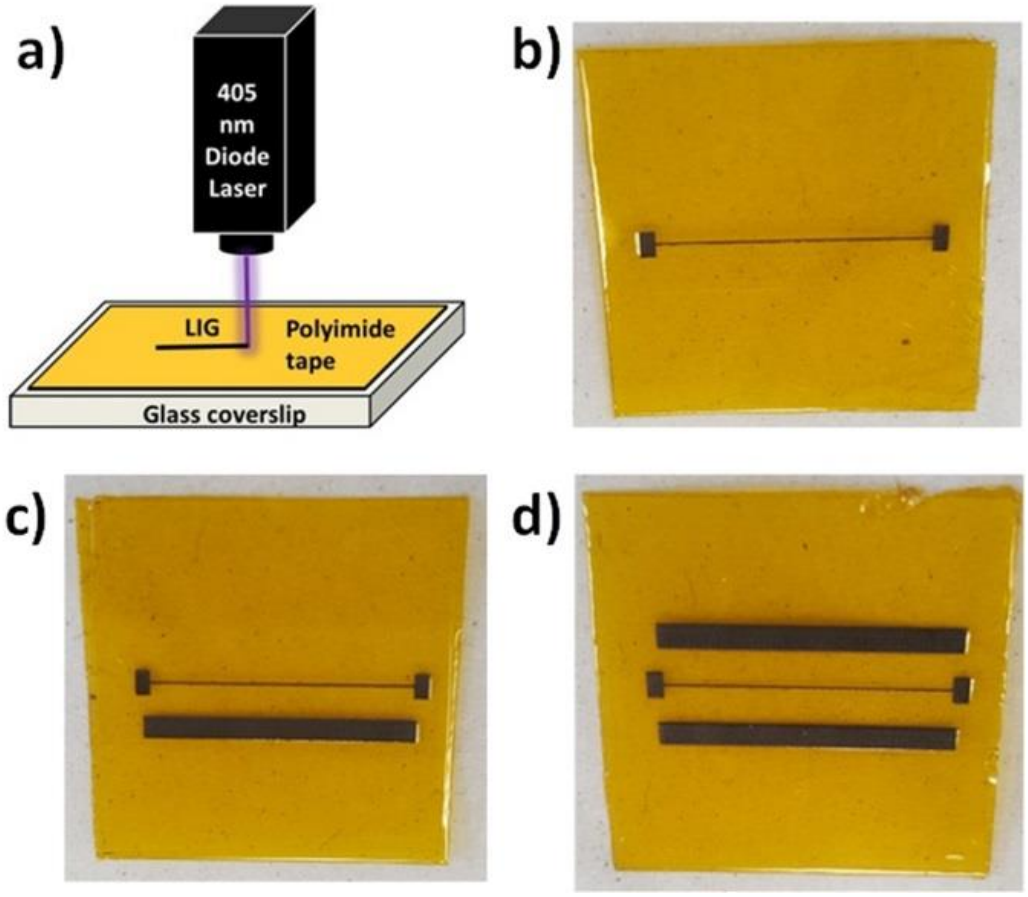


Figure 2.1. a) Schematic of LIG fabrication process; b-d) Photographs of LIG electrochemical platforms showing working (thin line, ~ 120 µm width) and counter/reference electrodes (thick lines, ~ 1 mm width) fabricated at 50 ms/pix dwell time.

All electrodes in this work were fabricated by direct laser writing of polyimide tape attached onto a glass microscope slide or coverslip for mechanical support. Figure 2.1a shows a schematic of the LIG process whereby computer-aided designs were written on polyimide tape by laser raster scanning with a commercial laser engraving machine. Figure 2.1b-d shows photographs of representative one-, two- and three-electrodes electrochemical sensor platforms fabricated at 50 ms/pix dwell time

comprising a thin line (ca. 120 µm width) as working electrode and thicker lines (ca. 1 mm) as counter and reference electrodes.

Figure 2.2 shows correlated optical (a-d) and scanning electron (e-h) microscopy images of LIG electrodes obtained at representative 20, 50, 80 and 110 ms/pix laser dwell times. It should be specified that the dwell time is the time the focused laser beam rested on a single pixel and illuminated it. Therefore, longer pixel times correspond to lower laser scan speeds. Complete sequences of optical and electron microscopy images for the full range of dwell times (10-110 ms/pix) are shown in Figure S2.1,2. The optical images showed that the LIG track patterns comprised individual quasi-hemispherical islands (see blue square Figure 2.2c), where each island corresponded to one pixel in the original design. At low dwell times, the LIG pixel islands had a diameter of ca. 100 µm with clear "necks" between adjacent islands. However, as the dwell time increased, the island diameters increased to ~130 µm, the inter-island separation decreased until coalescence of adjacent pixel islands was observed above 40 ms/pix dwell time. SEM images showed that the LIG islands were characterized by a highly porous 3D morphology associated to the rapid generation of gas (breaking of C-H, C-N, C-O, C=O atoms and local oxygen) occurring during the LIG process and increased by the availability of local O_2, due to the process being performed under ambient conditions.[10, 21] As already observed in the optical images, SEM images showed that individual islands became increasingly better-defined and showed increased coalescence as the dwell time increased. Specifically, at 20 ms/pix dwell time, a 3D surface topography characterized by micron-scale blister-like features was observed. Very few micropores were observed at this dwell time. In contrast, as the laser dwell time increased, open micropores were clearly evident across the surface, consistent with "bursting" of the

microblisters due to explosion of gas microbubbles and/or ablation of surface material. This morphology was consistent with the occurring of a laser-assisted high-temperature, high pressure process whereby polyimide absorbed the laser photon energy and converted it into heat.[22] In order to quantify the sample porosity, gas adsorption measurements (Figure S2.3) were performed for 50 ms/pix LIG and revealed formation of a microporous structure with a specific surface area of 428 m^2/g, higher than the 342 m^2/g value reported by Lin *et al.* for LIG structures obtained by CO_2 laser irradiation.[10]

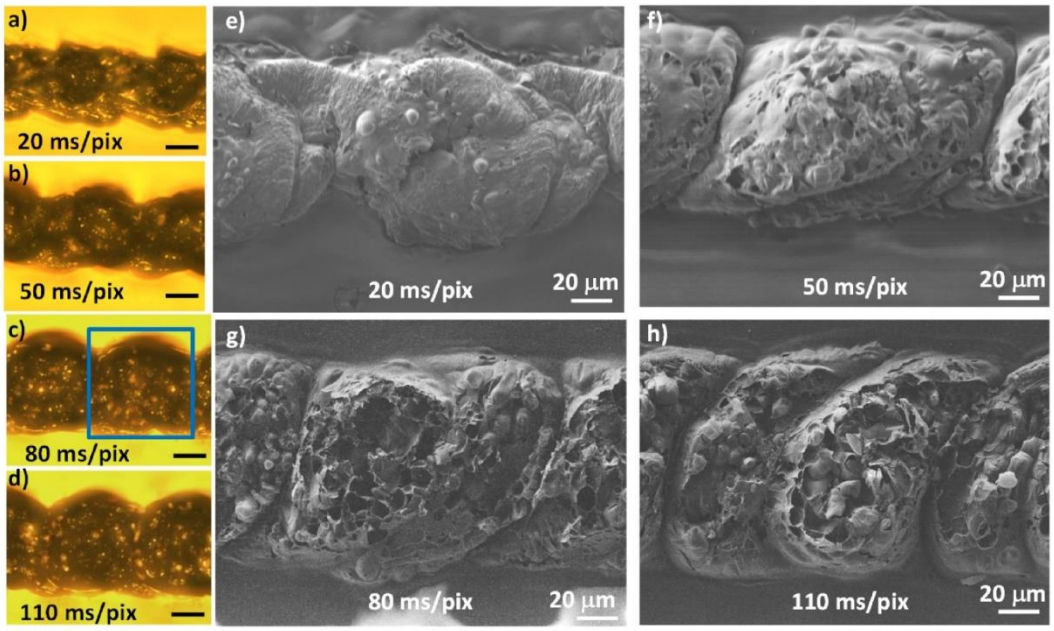


Figure 2.2. Optical (a-d) and scanning electron (e-h) micrographs of LIG electrodes fabricated at 20, 50, 80 and 110 ms/pix dwell times. Scale bars on optical images: 50 μm.

Electron microscopy was also used to measure the thickness of fabricated LIGs. The nominal thickness of commercial polyimide tape was 80 μm. Figure 2.3a shows a cross-section SEM image of a single line written at dwell time 50 ms/pix and showing a LIG structure ~ 50 μm protruding ~ 50 μm above the polyimide substrate. The

nearly-Gaussian LIG shape reflected the laser intensity beam distribution, a feature that has not been reported with higher cost/high power laser engraving systems.[23] Thickness data for LIG lines written in the 20 -120 ms/pix dwell time range were obtained by profilometry. Figure 2.3b shows average heights measured for three different set of lines across three areas. The protrusion thickness increased from 43 to 51 µm as dwell times increased from 20 to 50 ms/pix and slowly decreased to 34 µm for higher dwell times, suggesting the occurrence of oxidation or ablation processes, deleterious for the formation of good quality graphitic carbon structures.[10]

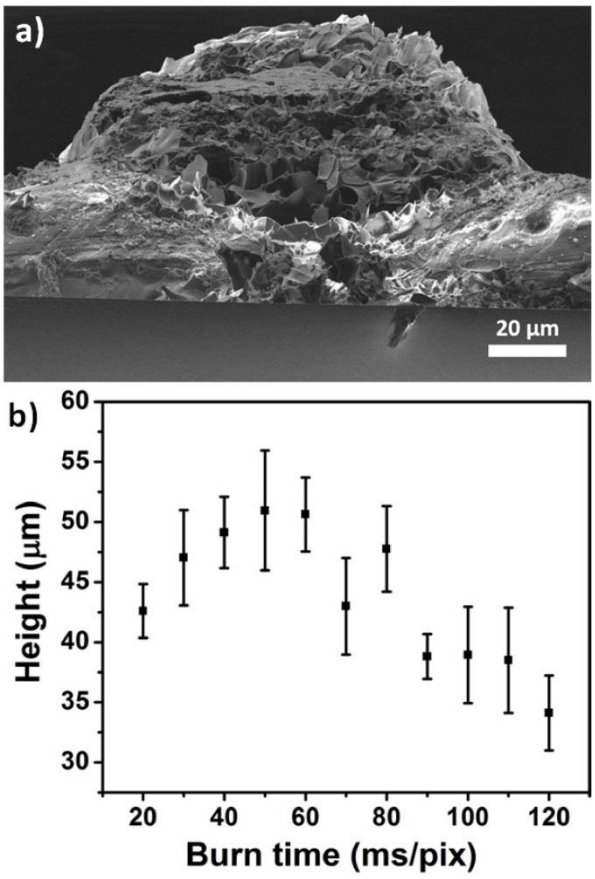


Figure 2.3. a) Cross-section SEM image of a LIG track written at 50 ms/pix; b) Profilometer height measurements for LIG tracks in the 20 – 120 ms/pix dwell time range.

LIG surface properties investigated by contact angle (CA) measurements showed hydrophobic characteristics. Specifically, measurements were performed for LIG structures obtained in the 20 to 110 ms/pix dwell times (see Figure S2.4) and the following CA values were found: LIG 20 ms/pix = 98.5°; LIG 50 ms/pix = 97.7°; LIG 80 ms/pix = 137.0°; LIG 110 ms/pix = 131.3°. These data were in contrast with LIG hydrophobic properties reported for structures made by CO_2 laser scribing.[14,24] However, our data were in agreement with surface properties of other LIG structures fabricated by 405 nm lasers [18,19] The CAs of low dwell time structures were consistent with CA values reported for amorphous Carbon (a-C) structures deposited at either high temperature (200 °C, CA = 97°)[25] or high temperature/pressure (85 C and 10 mbar, CA = 85°) conditions.[26] The hydrophobicity of a-C materials was attributed to the presence of nano- to micro- sized particles randomly distributed on the carbon surface. Similarly, a microporous surface was observed in LIG structures obtained at 20 and 50 ms/pix dwell times. Further increase in surface roughness could be the cause for the increased CA values found in 80 and 110 ms/pix LIG structures. However, the observed hydrophobicity could also be generated by the presence of oxygen and other reactive molecules free to attach to dangling bond during LIG formation. In addition, as LIG formation occurs at ambient conditions, air molecules can easily to get trapped within the microporous structures, preventing liquid molecules to enter into the pores and therefore giving hydrophobicity. Finally, reported values were also in agreement with wettability studies performed on graphitic carbon, reporting apparent water-contact angles (WCA) between 35° and 126° for either basal or edge graphite surfaces, depending on surface contamination and roughness.[27]

Figure 2.4 shows electrical characterization data acquired from a total of 57 transmission line structures fabricated over a range of dwell times (10 – 120 ms/pix). Figure 2.4a shows a typical set of two-terminal current vs. voltage (I-V) curves for positive bias voltages (0 – 1 V) measured for a single transmission line device fabricated at 50 ms/pix. All curves are linear over the bias voltage range (± 1 V). Figure 2.4b shows the track resistance data for this structure plotted *vs* track length. Linear regression of these data allows the sheet resistance and the contact resistance to be calculated from the slope and intercept, respectively (see equation 1, experimental session). For this device sheet resistance $R_s = 85 \pm 8$ Ω/square and contact resistance $R_c = 575 \pm 65$ Ω were measured. Panels c and d in Figure 2.4 show the extracted R_s and R_c data for multiple devices for each dwell time (30 devices in total). The trend shows a region of lower sheet resistance (80 – 100 Ω/square) for dwell times in the range 40 – 70 ms/pix. The contact resistance data (Figure 2.4d) also show minimum values (~ 600 Ω) over the same dwell time range. These data correlated well with the small and not uniform pore distribution and poor degree of structural connection between pixels observed in the optical images of Figure 2.2 for low dwell times. However, for dwell times of 40 ms/pix and above sheet resistance values abruptly dropped and saturated at ~80 Ω/square. This behavior was consistent with the formation of structures constituted by well-connected spherical units, as shown by optical and electron microscopy images (Figure 2.2). In addition, measured sheet resistance values correlated well with the observed thickness values previously measured, showing that up to 60 ms/pix, LIG structures of increased thickness showed decreased sheet resistance values and that increased resistance was measured at high dwell times, in agreement with the occurrence of deterioration processes at such high dwell times. The measured sheet resistance values at this modest laser power (0.5 W) were lower than values reported for other graphene-derived samples

(graphene/PET 280 Ω/sq;[28] graphene/SiO_2 350 Ω/square;[29] rGO/PET 226 Ω/square)[30] and LIG/polyimide structures reported by Romero *et al.* for a 405 nm laser diode at 0.1 W power (242 Ω/square, 295 Ω/square).[21] As expected, sheet resistance values were larger than the 35 Ω/square value reported by Tour *et al.* for LIG from CO_2 laser irradiation at higher laser powers (3.5 W).[10] In addition, our sheet resistance values were significantly lower in comparison with values reported for 3D nanostructured graphene structures obtained by inkjet printing/laser irradiation processes (10 MΩ/sq before laser irradiation, 0.7 kΩ/sq post laser irradiation).[31]

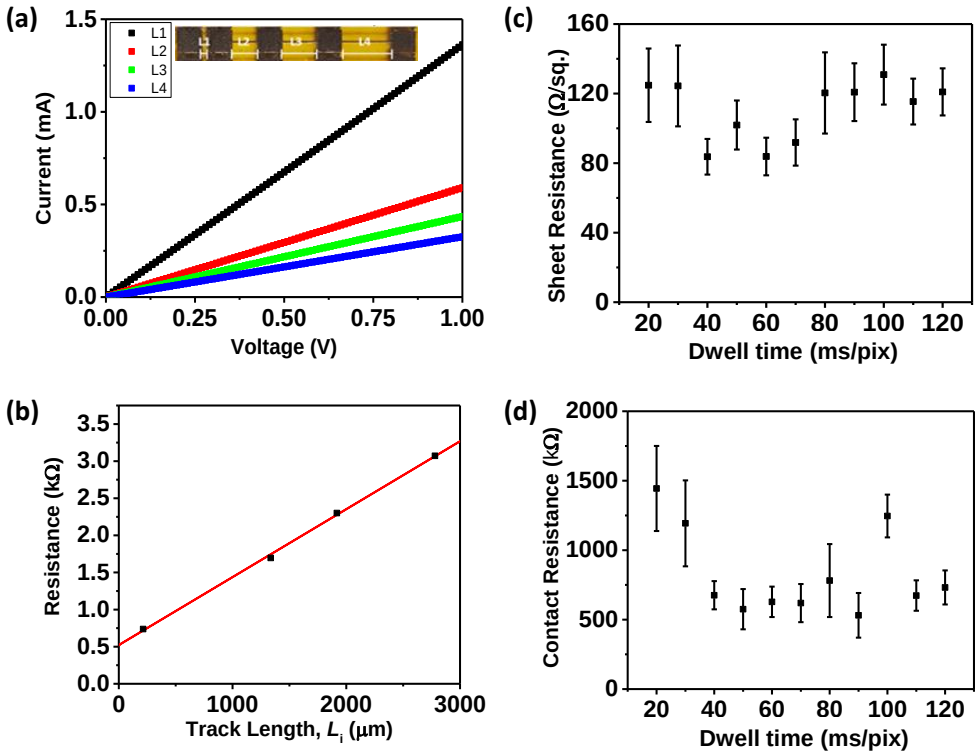


Figure 2.4. a) I-V measurements on a transmission line measurement (TLM) structure written at 50 ms/pix dwell time, comprising four different track lengths (L_i) with mm-scale contact pads. b) Corresponding track resistance (R_i) values *vs* length (L_i). Inset: photograph of TLM structures; c) Sheet resistance *vs* dwell time and d) Contact resistance vs dwell time measured for dwell times 10 -120 ms/pix.

Figure 2.5a shows representative LIG Raman spectra for four distinct dwell times: 20, 50, 80 and 110 ms/pix, respectively. Each spectrum shows two strong and distinct peaks in the 1000–1800 cm^{-1} range: the *G* mode centered close to 1580 cm^{-1}, assigned to in-plane bond stretching of pairs of sp^2 carbon atoms; and the *D* mode centered close to 1350 cm^{-1}, assigned to a defect-activated radial breathing mode.[32,33] Most of the spectra showed weak and/or broad features in the *2D* region close to 2700 cm^{-1}. However, spectra with clear second-order *2D* peaks could be observed for low dwell times (20-60 ms/pix), indicating generation of graphene-like carbon morphologies. As SEM images of Figure 2.2 showed formation of structures with inhomogeneous morphologies, a deeper Raman analysis was carried out whereby for each dwell time, 24 spectra were acquired across an 8×3 grid with a pitch of 15 μm close to the central axis of the track, i.e.. over a rectangular area of length 120 μm (parallel to track) and width 45 μm. Single Lorentzian line-shapes were fitted to the *D*, *G* and *2D* regions. Considering the first-order *D* and *G* peaks, Figure 2.5b, c showed that dwell times in the 20–50 ms/pix range yielded to the lowest mean full width at half maximum (FWHM) values of 85–100 cm^{-1} and 75–80 cm^{-1} for *D* and *G* peaks, respectively. For higher dwell times a broadening of these peaks was observed, representative of an increased degree of disorder in the sample.

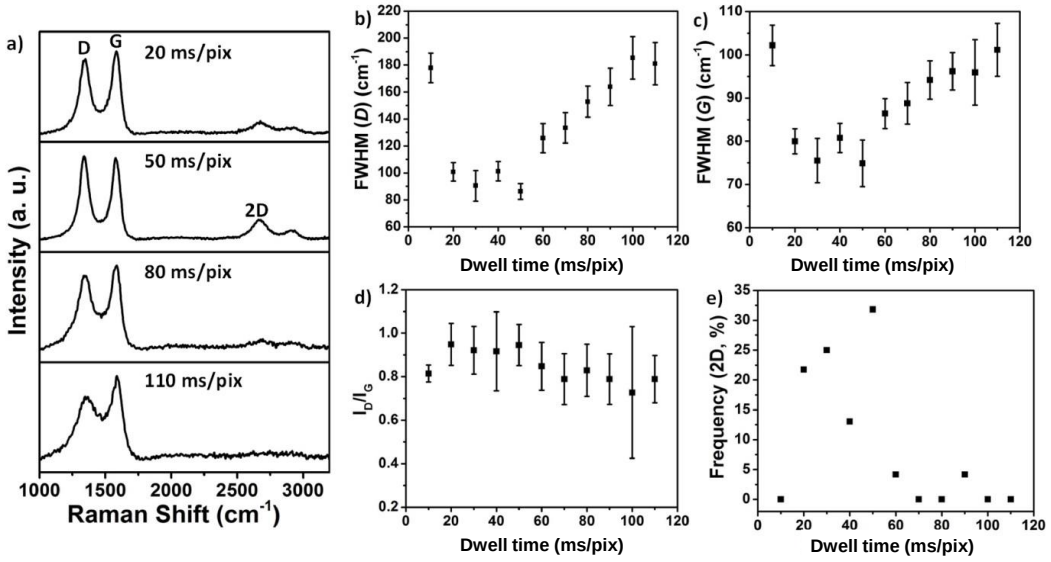


Figure 2.5. a) Representative Raman spectra of LIG electrodes fabricated at 20, 50, 80 and 110 ms/pix dwell times; b) Full width at half maximum (FWHM) intensity of the D peak vs dwell time; c) FWHM intensity of the G peak *vs* dwell time. Error bars in b) and c) represent standard error on the mean plus fit error; d) I_D/I_G ratios across dwell times; e) Frequency of 2D peak *vs* dwell times.

These observations fitted well with the trends reported by Koenig *et al.* in the first Raman study of graphite.[34] Based on studies of microcrystalline samples, the authors proposed an empirical model whereby the ratio of the intensities for the *D* and *G* peaks (I_D/I_G) scaled inversely with the crystallite size, L_a (determined from X-ray data). In this work and subsequent reports from many groups, there is an evident trend of increased I_D/I_G and broadening of both D and G peaks as the disorder in the sample increased, e.g. through ion implantation of natural graphite.[35] These authors more recently developed a model for disordered graphite with calculated disorder-induced peaks close to 1360 cm^{-1} (D peak) and 1620 cm^{-1} (now termed the D' peak), as well as the expected G peak.[33] Robertson *et al.* developed a framework to interpret this "amorphization trajectory" from pure graphite to nanocrystalline graphite to

amorphous carbon in terms of the factors that control the position, intensity, and widths of the G and D peaks.[32] For LIG structures data extracted from Lorentzian peak fits (Figure 2.5b,c and Figure S2.5) are consistent with Stage 1 of the trajectory, i.e. between highly ordered graphite and nanocrystalline graphitic domains in a disordered carbon matrix. Specifically, the G peak position (Pos(G)) remaining close to 1580 cm^{-1} (Figure S2.5b) and $I_D/I_G < 1$ (Figure 2.5d) across the entire dwell time range suggest that the laser-induced graphitization process results in nanocrystalline graphitic carbon films, with the highest order in the 20–50 ms/pix dwell time range. Furthermore, comparing the spectra acquired for 50 ms/pix dwell time with the data of Lespade *et al.* suggests grain sizes in the range 3-7 nm.[35] The presence of sharp 2D peaks provides further evidence for a higher degree of ordering. Out of more than 250 spectra acquired across all dwell times, 23 spectra showed evidence of a distinct 2D peak FWHM(2D) < 200 cm^{-1} and $I_{2D}/I_G > 0.2$, Figure S2.5e, respectively). The majority of these spectra (21 of 23) were acquired in the 20–50 ms/pix dwell time range (Figure 2.5c). Taken together, the Raman and I-V data suggest an optimum dwell time window close to 50 ms/pix. Data for low dwell times (10-20 ms/pix) are consistent with a lower degree of order due to incomplete graphitization while the data from the higher dwell times (80-110 ms/pix) are consistent with disorder arising from unwanted oxidation or ablation.

The laser-treated films were further characterized by XPS. Figure 2.6 shows XPS surveys of LIGs obtained at 20, 50, 80 and 110 ms/pix showing how the surface was mainly constituted by carbon, oxygen and nitrogen. The deconvolution of the main C_{1s} peak in its components (the main peak C-C sp^2 and C-C sp^3 carbon bonds, C-O(H) epoxides and hydroxides, carbonyls C=O, carboxyls O-C=O(H) and the π–π^* transition loss) showed low contribution from polyimide O-C=O and C=O bonds

whereas the contribution from sp^2- C-C bonds was the highest in the 20 – 80 ms/pix dwell time interval. In contrast, at 110 ms/pix the majority of carbon was sp^3-type, supporting the previous hypothesis that deterioration of the surface or ablation occurred at this high dwell time. The N_{1s} peak (shown in Figure S2.7) consists of one component at samples 20, 50 and 80 ms/pix centered at 400.1 eV whereas in the 110 ms/pix irradiated sample a second component appeared at ~402 eV, commonly assigned to oxidized nitrogen atoms. The atomic content of the constituent atoms is presented in Table 1. From the core level peaks of C1s, O1s and N1s the percentage atomic concentration of carbon, oxygen and nitrogen was determined by dividing the peak intensities with the appropriate relative sensitivity factor (RSF) after correcting them from the experimentally determined EA10 analyzer transmission characteristics. High percentages of carbon sp^2-type and low percentages of oxygen and nitrogen in the 20 -80 ms/pix dwell time interval confirmed the rapid breaking and removal of C-N, C-O, C=O and sp^2 carbon atoms occurring during the LIG process responsible for the formation of the porous morphology. Also, the C-O peak becomes more prominent than the C=O in the 20 – 50 ms/pix dwell time interval (Figure S2.6). By contrast, at 110 ms/pix, lower percentage of carbon sp^2-type, increased presence of carbon sp^3-type and atomic oxygen atomic concentration occurs. Moreover, presence of nitrogen oxide component in the N1s peak was detected at this burning condition.

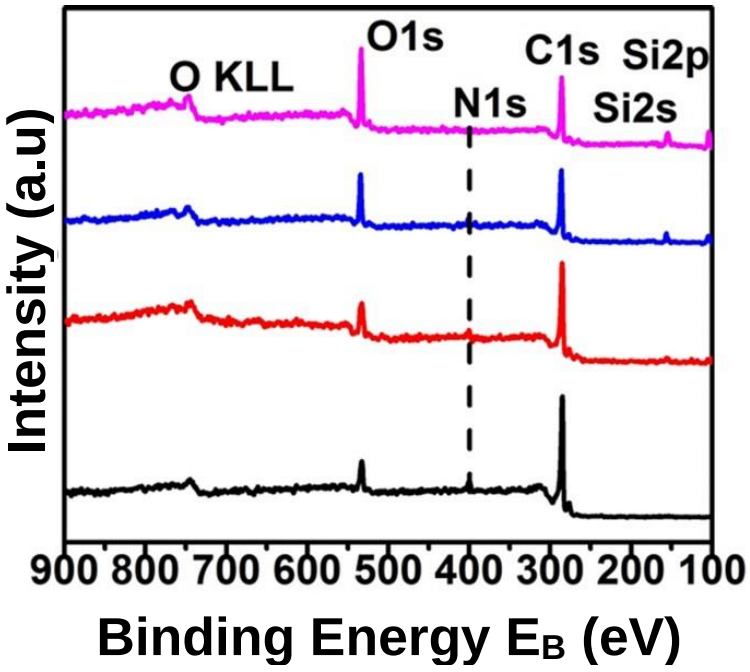


Figure 2.6. Survey scans of LIG electrodes fabricated at 20 (black line), 50 (red line), 80 (blue line) and 110 (pink line) ms/pix laser dwell times.

Table 2.1. Percentage C-C sp^2, C-C sp^3, epoxides-hydroxides, carbonyls carboxyls and π-π* bonding as derived from C1s XPS spectrum deconvolution. The % carbon, oxygen and nitrogen atomic concentration is also presented for the 20, 50, 80 and 110 ms/pix irradiated samples.

Sample (ms/pix)	% C-C sp^2	% C-C sp^3	% C-O(H)	% C=O	% C-OOH	% π-π*	%C	%O	%N
20	56.8	13.6	15.4	6.6	3.7	3.9	88.1	6.2	5.7
50	52.3	16.7	20.1	6.9	2.4	1.6	85.2	9	5.2
80	60.2	19.4	13.8	3.2	2.1	1.3	84.2	10.8	5
110	40.9	40.9	23.8	2.6	2.6	0	80	17.5	2.5

Finally, the electrochemical behavior of LIG electrodes was investigated by cyclic voltammetry measurements performed with two redox systems: outer-sphere $Ru(NH_3)_6^{3+/2+}$ and inner sphere $Fe(CN)_6^{3-/4-}$. In order to accurately monitor the electrochemical behavior of the LIG working electrode, and to accurately compare

HET values with literature data, CVs were recorded in a three-electrode system with a Pt wire as counter electrode and Ag/AgCl as reference electrode. CVs were also recorded in $[Ru(NH_3)_6]^{3+/2+}$ for systems including LIG as counter and working electrode (see Figure S2.9) to show versatility and easiness of use of the fabricated systems. Quasi-reversible behavior between 5 and 500 mV/s scan rates and monotonic increase of the oxidation peak current with the square root of the scan rate was observed for both systems (Figure S2.9).

The electrochemical characteristics of LIG working electrodes fabricated between 20 and 110 ms/pix are illustrated in Figure 2.7a. The electrodes showed decreasing values of differential peak potential (ΔE_p) until a minimum value of 74.5 mV and 85.6 mV was reached at 50 ms/pix for $[Ru(NH_3)_6]^{3+/2+}$ and $[Fe(CN)_6]^{3-/4-}$, respectively. The ΔE_p value obtained for $[Ru(NH_3)_6]^{3+/2+}$ was lower than the average 85.6 mV value reported by Nayak *et al.* for LIG structures obtained by CO_2 laser fabrication and was comparable with the average 74.5 mV value reported by the same authors for hybrid LIG/Pt electrodes.[14] In contrast, the value obtained for $[Fe(CN)_6]^{3-/4-}$ was comparable with the average value of 85.6 mV reported by Nayak *et al.* for LIG electrodes. Figure 2.7b shows CVs of a LIG working electrode fabricated at 50 ms/pix recorded between 5 and 200 mV/s for $[Ru(NH3)_6]^{3+/2+}$ showing quasi-reversible reaction *vs* Ag/AgCl reference electrode, evidenced by the monotonic increase/decrease of the oxidation/reduction peak current with square root of scan rate (inset of Figure 2.7b). Equivalent CVs for all dwell times in the interval 30 ms/pix – 120 ms/pix are showed in Figure S2.11. The average HET (k_0) value calculated by the Nicholson method[36] over three 50 ms/pix electrodes was 0.0146 $\pm$ 2.08 cm/s, comparable to other sp^2 carbon materials, such as graphene on copper electrode ($(15\pm2)\times10^{-3}$ cm/s)[37] and Q-graphene (18×10^{-3} cm/s).[38] Favorable electron

transfer kinetic was found compared to other graphene materials such as monolayer graphene (1.1×10^{-3} cm/s) and quasi-graphene (1.6×10^{-3} cm/s) and graphite based electrodes (edge plane pyrolytic graphite EPPG = 8.8×10^{-3} cm/s and basal plane pyrolytic graphite BPPG = 38×10^{-3} cm/s).[39] This is interesting because $[Ru(NH_3)_6]^{3+/2+}$ being an outer sphere redox mediator is insensitive to oxygen content and surface structure, and only sensitive to the density of electronic states (DOS). This means that the reversible redox reaction of $[Ru(NH3)_6]^{3+/2+}$ (i.e.. rapid electron transfer) on the LIG electrode, must be supported by a sufficient DOS. This in turn can only be due to the increased DOS at the edges of graphene (compared to basal planes) resulting in a faster electrode kinetics and associated to the high 3D porous network rich in edge sites. The average HET (k_0) value calculated for $[Fe(CN)_6]^{3-/4-.}$ by the Nicholson method over three electrodes was $(13\pm1)\times10^{-3}$ cm/s (data not shown), comparable with reported literature data of CVD-Gr and Q-graphene.[14].

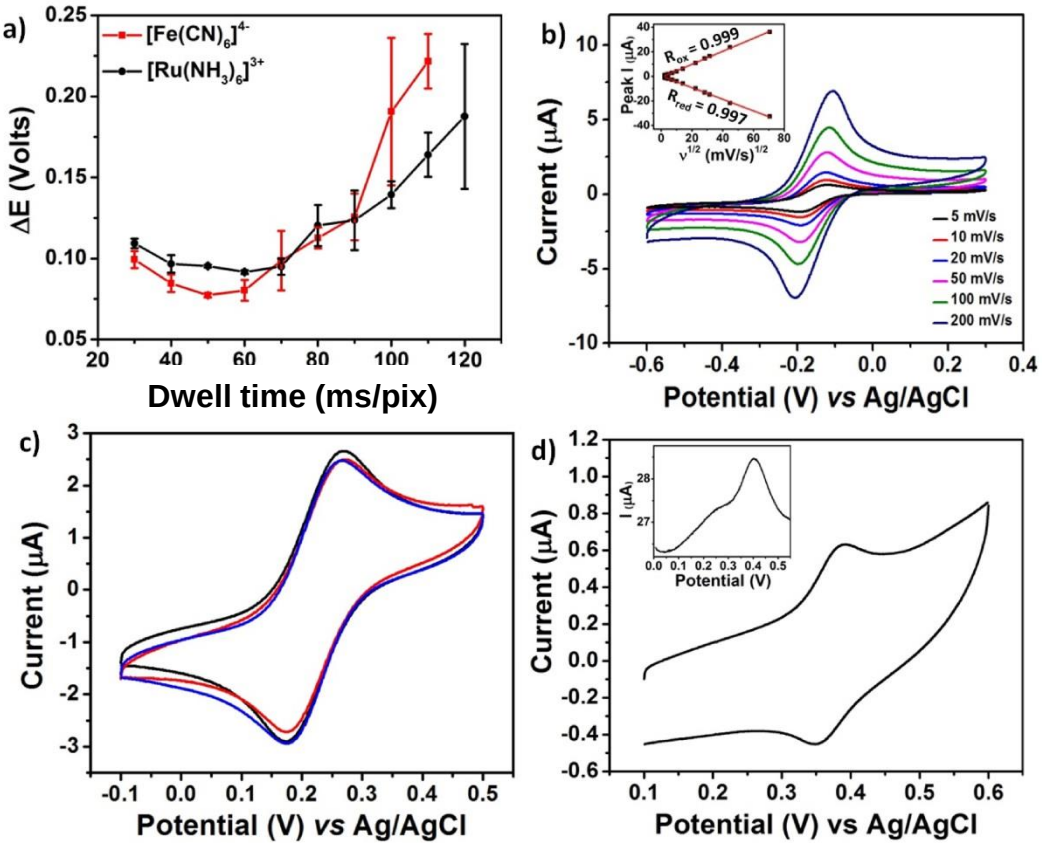


Figure 2.7. a) ΔEp values recorded in the interval 20 -120 ms/pix dwell time for 5 mM $Ru(NH_3)_6^{3+/2+}$ and $Fe(CN)_6^{3-/4-}$in 0.1 M KCl solution as supporting electrolyte at 100 mV/s; b) cyclic voltammograms at LIG electrode 50 ms/pix at different scan rates in 5 mM $Ru(NH_3)_6^{3+/2+}$ 0.1 M KCl. Inset: peak oxidation values vs square root of potential scan rate; c) repeat CVs at LIG electrode 50 ms/pix at 100 mV/s in 5 mM $Fe(CN)_6^{3-/4-}$ 0.1 M KCl; d) CV of 0.5 mM benzocaine at LIG electrode 50 ms/pix in 0.1 M KCl at 100 mV/s, pH = 2. Inset: benzocaine square wave voltammetric response measured for the same electrode.

Figure 2.7c shows CVs measured in $[Fe(CN)_6]^{3-/4-}$ for three different electrodes displaying good current reproducibility. In order to show practical applicability beyond standard redox mediators, Figure 2.7d shows electrochemical detection of benzocaine, a local anesthetic, frequently used as additive in street-samples of cocaine powder.[40]

The CV for 5 mM aqueous solution of benzocaine measured in 0.1 M KCl supporting electrolyte at pH 2 at 100 mV/s scan rate showed an oxidation peak at 0.386 mV and a reduction peak at 0.352 mV (*vs* Ag/AgCl). Peak position and sensitivity were comparable to those obtained in literature for carbon screen printed macroscopic electrodes.[40] Finally, square-wave voltammetry (SWV) was performed to characterize the electrochemical behavior of LIG electrodes with benzocaine (inset Figure 2.7d). A scan from 0 to 0.6 V vs Ag/AgCl was applied at frequency of 100 Hz, with an amplitude of 100 mV and a step potential of 1 mV. All benzocaine measurements were performed with portable potentiostat apparatus, in order to further show practical use and applicability.

2.4 Conclusions

Laser Induced graphene electrodes were fabricated on flexible polyimide sheets by direct laser irradiation with low-cost visible laser engraving machines under ambient conditions. The morphological, structural, electrical and electrochemical characteristics of LIGs obtained at different laser dwell times between 20 and 120 ms/pix were investigated. It was found that structures obtained at 40 - 50 ms/pix dwell times displayed 3D porous morphology, low sheet resistance and graphene-like carbon spectral signatures. The electrochemical characterization performed with outer-sphere $Ru(NH_3)_6^{3+/2+}$ and inner sphere $Fe(CN)_6^{3-/4-}$ redox mediators showed quasi-reversible electron transfer at the LIG working electrode and fast electron transfer kinetics with k_0 of 0.014 cm/s calculated for $Ru(NH_3)_6^{3+/2+}$ for 50 ms/pix working electrodes. Practical usability of fabricated electrodes for low-cost screening of analytes was demonstrated by the quasi-reversible electron transfer showed with all carbon systems and by the proof-of-concept detection of benzocaine obtained by low cost, lightweight and portable electrochemical readout instrumentation. These electrodes display great potential for low cost and disposable analysis and development of DIY flexible electrochemical platforms.

2.5 Experimental

Materials. Commercial polyimide films with a nominal thickness of 80 μm were purchased from Radionics and used without further treatment. Hexaammineruthenium(III) chloride, potassium hexacyanoferrate(III), potassium chloride and benzocaine were purchased from Sigma Aldrich and used without further purification. Milli-Q water (resistivity 18 MΩ.cm) was used throughout the experiments.

Electrode fabrication. LIG electrodes were fabricated with a mini-speed laser engraving machine (Colemeter DK-8 Pro-5 Square Haste Edition) equipped with a diode laser with wavelength of 405 nm. Polyimide tapes fixed on glass microscope slides for support were irradiated at 500 mW laser power and dwell times (dwell times) between 10 and 120 ms/pix. LIG electrode structures designed in Microsoft PowerPoint were fabricated by raster scanning of the laser beam to create the electrode pattern on the polyimide surface. Fabricated electrodes were washed with acetone and isopropanol and dried with a dry N_2 airflow before use.

Characterization. LIG electrodes were morphologically characterized by a cold-cathode field-emission Scanning Electron Microscope (SEM, JSM- 7500F, JEOL UK Ltd.) operating at 5 kV acceleration voltage. White light optical microscopy images of fabricated LIG electrodes were acquired with an Axioskop II, Carl Zeiss Ltd. Microscope interfaced to a charge-coupled detector camera (Coolsnap CF, Photometrics). LIG height measurements were acquired using a KLA-Tencor p17 profilometer with stylus weight 2 mg and resolution of 4 μm. Two-terminal current-voltage measurements (± 1V, 10 mV step) were obtained under ambient conditions on Transmission Line Method (TLM) structures using an Agilent E5270B parameter analyzer interfaced to a LakeShore Desert TTPX probe station. For these TLM

structures, arrays of LIG tracks were written at different dwell times ranging from 20 to 120 ms/pix. Each track had ~ 1 mm square LIG pads for electrical probing. Each TLM structure comprised 4 collinear tracks separated by contact pads allowing measurement of resistance for 4 values of track length for each device (L1= 225 µm, L2= 1335 µm, L3 = 1920 µm, L4= 2780 µm). The track resistance Ri between two consecutive pads could then be related to the track length (Li) via:

$$\boldsymbol{Ri} = \boldsymbol{Rc} + \frac{(\boldsymbol{Rs} \times \boldsymbol{Li})}{\boldsymbol{W}} \qquad \text{eq (1)}$$

where R_c is the contact resistance, R_s is the sheet resistance of the sample and W is the track width. Values for R_s and R_c were thus obtained from linear regression of Ri *vs* Li.

X-ray photoelectron spectroscopy (XPS) measurements were carried out in an ultrahigh vacuum (UHV) chamber with a base pressure ~$5x10^{-10}$ mbar equipped with a SPECS LHS-10 hemispherical electron analyzer and a dual anode Al/Mg x-ray gun. All XPS measurements were acquired using the un-monochromatized Mg Kα line at 1253.6 eV and an analyzer pass energy of 36 eV, giving a full width at half maximum (FWHM) of 0.9 eV for the Au 4f7/2 peak. The XPS core level spectra were analyzed by fitting each total spectrum to a series of individual mixed Gaussian-Lorentzian peaks following a Shirley background subtraction.

Raman measurements were performed with a Renishaw inVia Raman system equipped with a 514 nm helium–neon laser. The laser beam was focused onto the sample through a Leica 20X objective with 0.4 N.A. Acquisition time was usually 10 s and measured power was 3 mW.

Electrochemical measurements were performed with a CHI760 bi-potentiostat electrochemical system using a Pt wire as counter electrode, Ag/AgCl as reference electrode and LIG as working electrode. The three electrodes were assembled in a

Teflon cell (see Figure S2.8 for details) with a circular area of 8 mm diameter exposed to the electrolyte. Cyclic voltammetry (CV) experiments were performed in aqueous solution using inner-sphere ($[Fe(CN)_6]^{3-/4-}$) and outer-sphere ($[Ru(NH_3)_6]^{3+/2+}$) redox mediators at a concentration of 5 mM dissolved in 0.1 M KCl. Solutions were purged with N_2 for 30 min prior to measurements and during measurements. Heterogeneous electron transfer (HET) rate constants were determined from the anodic peak separation using the method of Nicholson[32] by assuming transfer coefficient $\alpha = 0.5$ and using the following diffusion coefficient $D = 6.5 \times 10^{-6}$ cm^2 s^{-1} for $[Ru(NH_3)_6]^{3+/2+}$. Benzocaine electrochemical characterization was carried out with an EmStatblue (Palmsens) portable potentiostat at a benzocaine concentration of 5 mM dissolved in 0.1 M KCl.

2.6 References

1) McCreery, R. T. Advanced Carbon Electrode Materials for Molecular Electrochemistry. *Carbon* **2008**, *108*, 2646-2687.
2) Unwin, P. R.; Güell, A. G.; Zhang. G. Nanoscale Electrochemistry of sp^2 Carbon Materials: from Graphite and Graphene to Carbon Nanotubes. *Acc. Chem. Res.* **2016**, *49*, 2041−2048.
3) Chen, D.; Feng, H.; Li, J. Graphene Oxide: Preparation, Functionalization, and Electrochemical Applications. *Chem. Rev.* **2012**, *112*, 6027-6053.
4) Wu, Z.-S.; Sun, Y.; Tan, Y.-Z.; Yang, S.; Feng, X.; Müllen, K. Three-Dimensional Graphene-Based Macro- and Mesoporous Frameworks for High-Performance Electrochemical Capacitive Energy Storage. *J. Am. Chem. Soc*. **2012**, *134*, 19532−19535.
5) Wu, M.; Meng, S.; Wang, Q.; Si, W.; Huang, W.; Dong, X. Nickel−Cobalt Oxide Decorated Three-Dimensional Graphene as an Enzyme Mimic for Glucose and Calcium Detection. *ACS Appl. Mater. Interf.* **2015**, *7,* 21089−21094.
6) Chen, Z.; Ren, W.; Gao, L.; Liu, B.; Pei, S.; Cheng, H. M. Three-Dimensional Flexible and Conductive Interconnected Graphene Networks Grown by Chemical Vapour Deposition. *Nat. Mater***. 2011**, *10*, 424-428.
7) Borini, S.; White, R.; Wei, D.; Astley, M.; Haque, S.; Spigone, E.; Harris, N.; Kivioja, J.; Ryhänen, T. Ultrafast Graphene Oxide Humidity Sensors. *ACS Nano* **2013**, *7*, 11166-11173.
8) Rai, M. A.; Kim, John, A. S.. Fabrication of Electrochemically Reduced Graphene Oxide Films on Glassy Carbon Electrode by Self-Assembly Method and Their Electrocatalytic Application. *J. Phys. Chem. C* **2013**, 117, 8, 4326-4335

9) Lawes, S.; Riese, A.; Sun, Q.; Cheng, N.; Sun, X. Printing Nanostructured Carbon for Energy Storage and Conversion Applications. *Carbon* **2015**, *92*, 150-176.

10) Lin, J.; Peng, Z.; Liu, Y.; Ruiz-Zepeda, F.; Ye, R.; Samuel, E. L. G.; Yacaman, M. J.; Yacobson, B. I.; Tour, J. M. Laser-Induced Porous Graphene Films from Commercial Polymers. *Nat. Commun.* **2014**, *5*, 5714-5719.

11) Chyan, Y.; Ye, R.; Li, Y.; Singh, S. P.; Arnusch, C. J.; Tour, J. M. Laser-Induced Graphene by Multiple Lasing: Towards Electronics on Cloth, Paper, and Food. *ACS Nano* **2018**, *12*, 2176-2183.

12) Li, L.; Zhang, J.; Peng, Z.; Li, Y.; Gao, C.; Ji, Y.; Ye, R.; Kim, N. D.; Zhong, Q.; Yang, Y.; Fei, H.; Ruan, G.; Tour, J. M. High-Performance Pseudocapacitive Microsupercapacitors from Laser-Induced Graphene. *Adv. Mater.* **2016**, *28*, 838-845.

13) Ye, R.; James, D. K.; Tour, J. M. Laser-Induced Graphene: From Discovery to Translation. *Adv. Mater.* **2019**, 31, 1803621.

14) Nayak, P.; Kurra, N.; Xia, C.; Alshareef. H. Highly Efficient Laser Scribed Electrodes for on-Chip Electrochemical Sensing Applications. *Adv. Electron. Mater.* **2016**, *2,* 1600185- 96.

15) .Zhang, C.; Xie, Y.; Zhang, C.; Lin, J. Upgrading coal to multifunctional graphene based materials by direct laser scribing. *Carbon* **2019**, 153, 585-591.

16) Fenzl, C.; Nayak, P.; Hirsh, T.; Wolfbeis, O. S.; Alshareef, H. N.; Baeumner, A. Laser-Scribed Graphene Electrodes for Aptamer-Based Biosensing. *ACS Sens*. **2017**, *2*, 616-620.

17) Cardoso, A. R.; Marquesa, A. C.; Santos, L.; Carvalho, A. F.; Costa, F. M.; Martins, R.; Goreti M.; Sales, F.; Fortunato, E. Molecularly-Imprinted Chloramphenicol Sensor with Laser-Induced Graphene Electrodes. *Biosens. Bioel.* **2019**, *124–125*, 167–175.

18) .Zhang, Z.; Song, M.; Hao, J.; Wu, K.; Li, C.; Hu, C; Visible light laser-induced graphene from phenolic resin: A new approach for directly writing graphene-based electrochemical devices on various substrates. *Carbon* **2018**, 127, 287-296.

19) Cai, J.; Watanabe, A. Laser direct writing of high-performance flexible all-solid-state carbon micro-supercapacitors for an on-chip self-powered photodetection system. *Nano Ener*. **2016**, 30, 790-800.

20) Vanegas, D. C.; Patino, L.; Mendez, C.; Alves de Oliveira, D.; Torres, A. M.; Gomes, C. L.; McLamore, E. S. Laser Scribed Graphene Biosensor for Detection of Biogenic Amines in Food Samples Using Locally Sourced Materials. Biosensors **2018**, 8, 42-61.

21) Romero, F. J.; Salinas-Castillo, A.; Rivadeneyra, A.; Albrecht, A.; Godoy, A.; Morales, D. P.; Rodriguez, N. In-Depth Study of Laser Diode Ablation of Kapton Polyimide for Flexible Conductive Substrates. *Nanomaterials* **2018**, *8*, 517-528.

22) Dong, Y.; Rismiller, S. C.; Lin, J. Molecular Dynamic Simulation of Layered Graphene Clusters Formation from Polyimides under Extreme Conditions. *Carbon* **2016**, *104*, 47-55.

23) Luo, S.; Hoang, P. T.; Liu, T. Direct Laser Writing for Creating Porous Graphitic Structures and their Use for Flexible and Highly Sensitive Sensor and Sensor Arrays. *Carbon* **2016**, 98, 522-531.

24) Li, Y.; Luong, D. X.; Zhang, J.; Tarkunde, Y. R.; Kittrell, C.; Sargunaraj, F.; Ji, Y.; Arnusch, C. Y.; Tour, J. M. Laser-Induced Graphene in Controlled Atmospheres: From Superhydrophilic to Superhydrophobic Surfaces, *Adv. Mater.* **2017**, 29, 1700496.

25) Zhou, Y.; Song, X.; Li, E.; Li, G.; Zhao, S.; Yan, H. Control Over the Wettability of Amorphous Carbon in a Large Range from Hydrophilicity to Super-hydrophobicity. *Appl. Surf. Sci.* **2006**, *253*, 2690-2694.

26) Banerjee, D.; Mukherjee, S.; Chattopadhyay, K. K. Controlling the Surface Topology and Hence the Hydrophilicity of Amorphous Carbon Thin Films. *Carbon* **2010**, *48*, 1025-1031.

27) Wei, Y.; Charles, Q. Y. Intrinsic Wettability of Graphitic Carbon. Carbon **2015**, *87*, 10-17.

28) Kim, K.; Zhao, Y.; Jang, H.; Lee, S.; Kim, J.; Kim, K.; Ahn, J.; Kim, P.; Choi, J.; Hong, B. Large-Scale Pattern Growth of Graphene Films for Stretchable Transparent Electrodes. *Nature* **2009**, *457*, 706–710.

29) Li, X.; Zhu, Y.; Cai, W.; Borysiak, M.; Han, B.; Chen, D.; Piner, R.D.; Colombo, L.; Ruoff, R.S. Transfer of Large-Area Graphene Films for High-Performance Transparent Conductive Electrodes. *Nano Lett.* **2009**, *9,* 4359–4363.

30) Romero, F. J.; Rivadeneyra, A.; Toral, V.; Castillo, E.; Garcia-Ruiz, F.; Morales, D. P.; Rodriguez, N. Design Guidelines of Laser Reduced Graphene Oxide Conformal Thermistor for IoT Applications. *Sens. Actuators A Phys*. **2018**, *274*, 148–154

31) Das, S. R.; Nian, Q.; Cargill, A. A; Hondred, J.; Ding, S.; Saei, M.; Cheng, G. J.; Claussen, J. C. 3D Nanostructured inkjet Printed Graphene via UV-pulsed Laser Irradiation Enables Paper-Based Electronics and Electrochemical Devices. *Nanoscale* **2016**, 8, 15870-15879.

32) Ferrari, C.; Robertson, J. Interpretation of Raman Spectra of Disordered and Amorphous Carbon. *Phys. Rev. B* **2000,** *61*, 14095.

33) Ferrari, A. C.; Basko, D. M. Raman Spectroscopy as a Versatile Tool for Studying the Properties of Graphene. *Nat. Nanotechnology.* **2013**, *8*, 235-246.

34) Tuinstra, F.; Koenig, J. L. Raman Spectrum of Graphite. *J. Chem. Phys.* **1970**, *53*, 1126-1130.

35) Lespade, P.; Al-Jishi, R.; Dresselhaus, M. S. Model for Raman Scattering from Incompletely Graphitized Carbons. *Carbon* **1982**, *20*, 427-431.

36) Nicholson, R. S. Theory and Application of Cyclic Voltammetry for Measurement of Electrode Reaction Kinetics. *Anal. Chem.* **1965**, *37*, 1351-1355.

37) Navarro, C. B.; Laker, Z. P.; Rourke, J. P.; Wilson, N. R. Reproducible, Stable and Fast Electrochemical Activity from Easy to Make Graphene on Copper Electrodes. *Phys. Chem. Chem. Phys.* **2015**, *17,* 29628-29636.

38) Randviir, E. P.; Brownson, D. A.; Gomez-Mingol, M.; Kampouris, D. K.; Iniesta, J.; Banks, C. A. Electrochemistry of Q-Graphene. *Nanoscale* **2012**, *4,* 6470-6480.

39) Brownson, D. A.; Varey, S. A.; Hussain, F.; Haigh, S. J.; Banks, C. E. Electrochemical Properties of CVD Grown Pristine Graphene: Monolayer-vs. Quasi-Graphene. *Nanoscale* **2014**, *6*, 1607-1621.

40) Komorsky-Lovric, S.; Vukasoeinovic, N.; Penovski, R. Voltammetric Determination of Microparticles of Some Local Anesthetics and Antithusics Immobilized on the Graphite Electrode. *Electroanalysis* **2003**, *15*, 544-547.

Supporting Information

Supporting information Fabrication and Electrochemical Properties of Three Dimensional (3D) Porous Graphitic and Graphene-like Electrodes Obtained by Low-Cost Direct Laser Writing Methods

Micheal Burke,[a] Cathal Larrigy,[a] Eoghan Vaughan,[a] George Paterakis,[b] Labrini Sygellou,[b] Aidan J. Quinn,[a] Grégoire Herzog,[d] Costas Galiotis,[c] Daniela Iacopino[a*] a Tyndall National Institute, University College Cork, Dyke Parade, Cork, Ireland b Institute of Chemical Engineering Sciences, Foundation for Research and TechnologyHellas (FORTH/ICE-HT), Patras 265 04, Greece

c Department of Chemical Engineering, University of Patras, Patras 26504, Greece d LCPME, CNRS-Université de Lorraine, 405 Rue de Vandoeuvre, 54600 Villers-lès-Nancy, France

Optical microscopy

Figure S2.1.1 Shows detailed optical microscopy images of LIG electrodes written at laser burn times between 10 and 120 ms/pix. Images captured at 10 ms/pix interval show progressive better definition and connection between individual pixels as well as progressive thickening from nominal 100 µm at 10 ms/pix to 130 µm at 120 ms/pix.

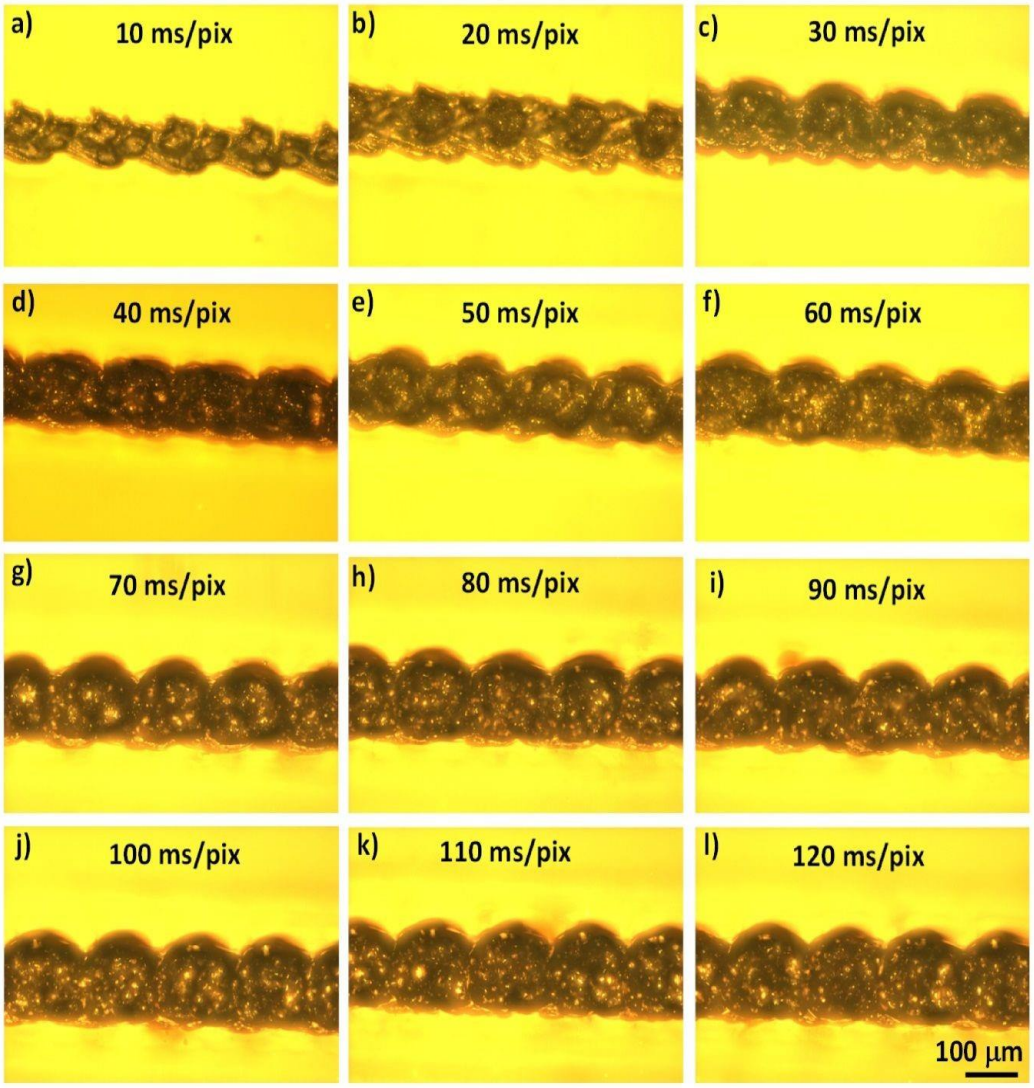


Figure S2.1 Optical microscopy images (a-l) of LIG electrodes written at laser burn times 10 - 120 ms/pix.

Scanning electron microscopy

SEM images in Figure S2.2 show progressive thickening of formed electrodes and increased pore sizes with the increase of the laser burn time from 10 to 120 ms/pix.

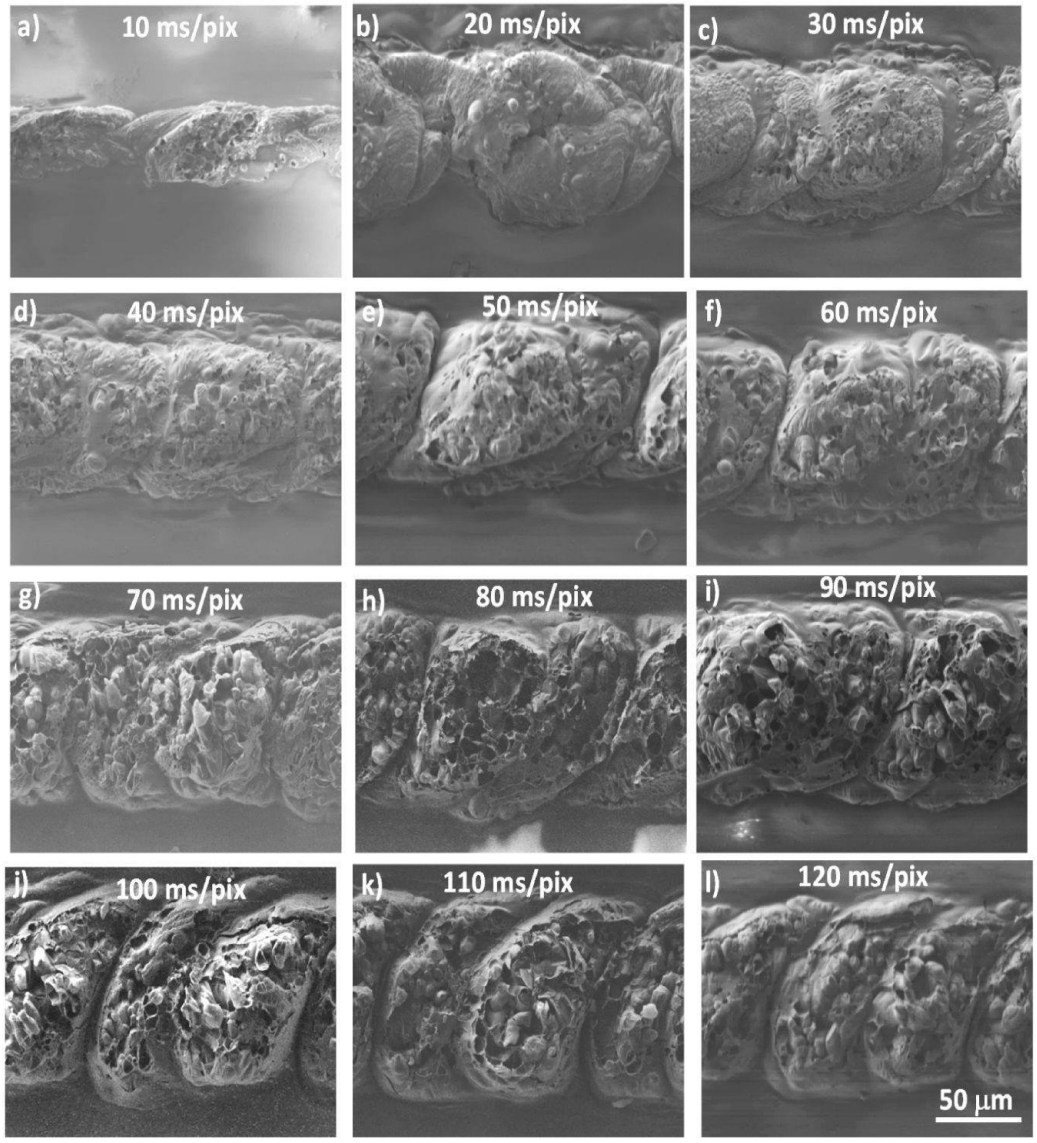


Figure S2.2. SEM images (a-l) of LIG electrodes written at laser burn times 10 -120 ms/pix.

Determination of specific surface area

The αs plot method was used for the determination of surface area. Adsorption / desorption isotherm was measured for nitrogen (N_2) using 22.6 mg of carbon scraped off from LIG structures obtained at 50 ms/pix. The results of the isotherms are shown in Fig. S3b. V_a represents the total gas volume adsorbed whereas p / p0 is the pressure ratio. The shape of the adsorption isotherm is of type I, which corresponds to microporous materials. The sharp increase of the adsorbed volume, V_a, for the low p / p0 values is due to the filling of micropores of molecular dimensions (< 1 nm). At the higher p / p0 values, the rise of V_a values might be due to the macro-porous nature of the carbon sample. For the sample analysed, the surface area was calculated to be 428 $m^2 g^{-1}$.

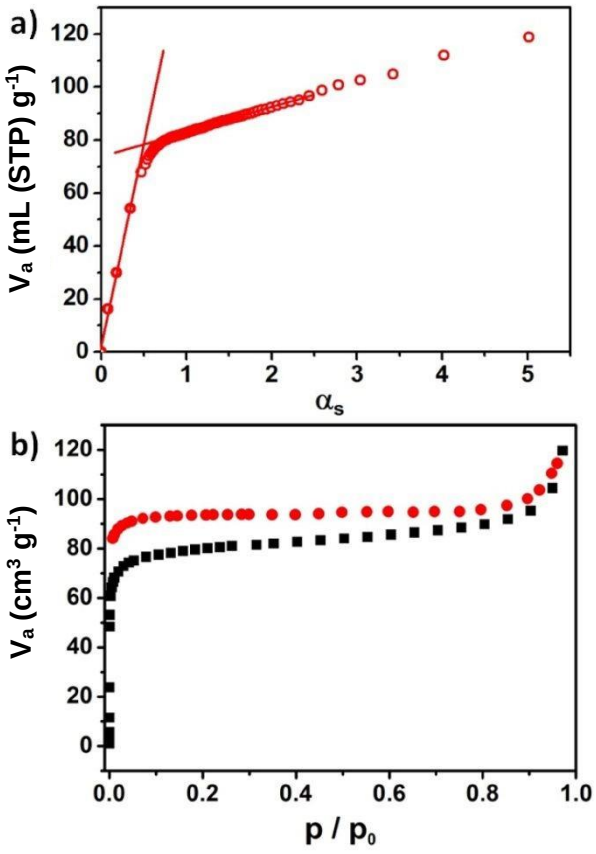


Figure S2.3. a) α_s plot for the determination of the surface area; b) Adsorption (black squares) / desorption (red circles) isotherm obtained for 50 ms/pix LIG material.

Contact angle measurements

Figure S2.4 shows details of LIG surface properties by contact angle measurements. The LIG surface showed hydrophobicity comparable to pristine Kapton tape at 20 and 50 ms/pix burn times. Higher hydrophobicity was calculated for higher burn times. The calculated contact angles (θ_c) are the following: Kapton = 91°, LIG 20 ms/pix = 85°; LIG 50 ms/pix = 94°; LIG 80 ms/pix = 146°; LIG 110 ms/pix = 128°.

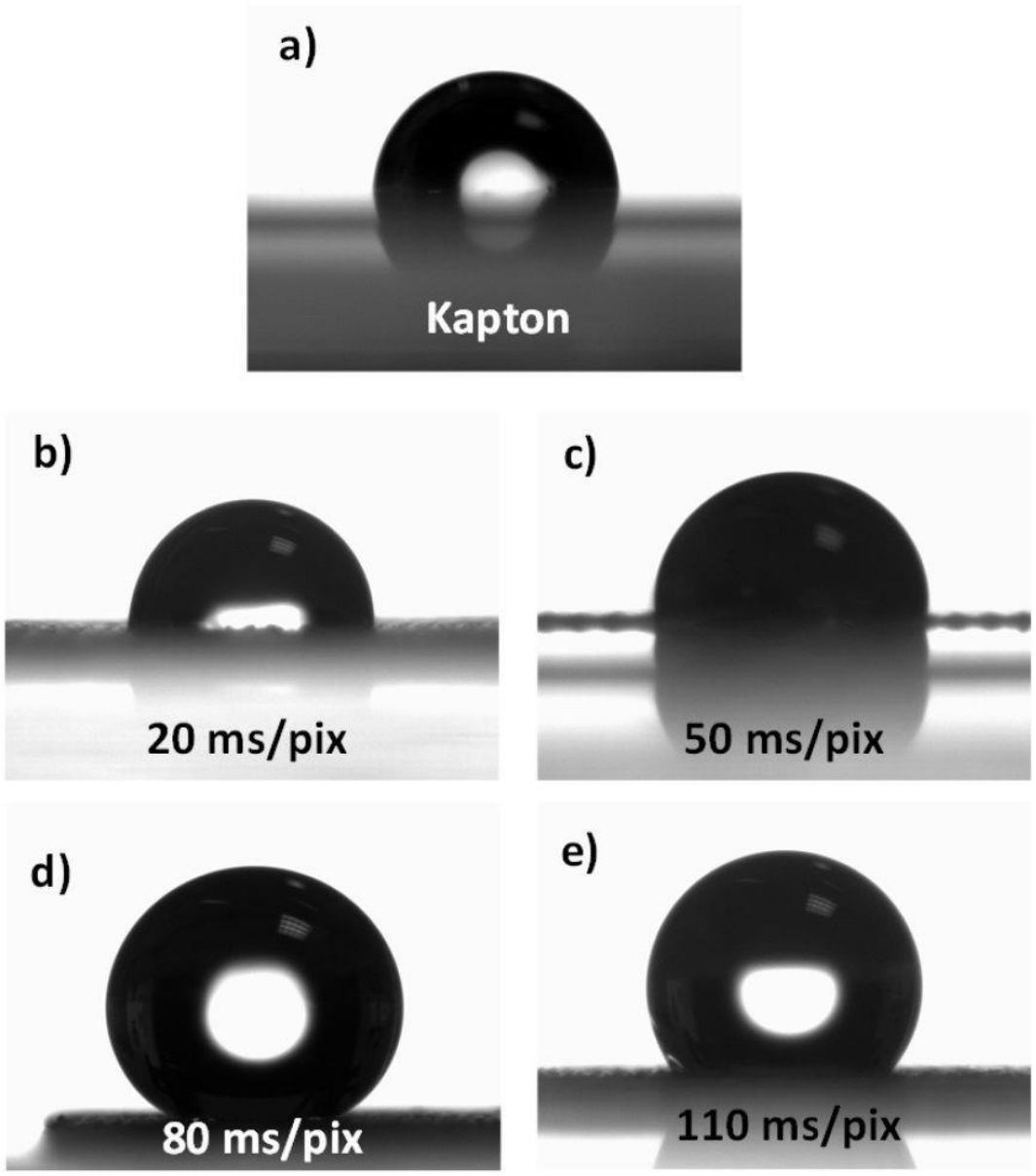


Figure S2.4. Characterization of surface property by contact angle for a) Kapton tape; b) LIG 20 ms/pix; c) LIG 50 ms/pix; d) LIG 80 ms/pix; e) LIG 110 ms/pix.

Raman analysis details

Figure S2.5 report spectral variations in D, G, 2D peak positions measured over 23 collected spectra in the 10 – 110 ms/pix burn time range. Full width-at-half-max (FWHM) measured in the 10 – 110 ms/pix burn time range for 2D peak as well as I_{2D}/I_G is also reported across burn times.

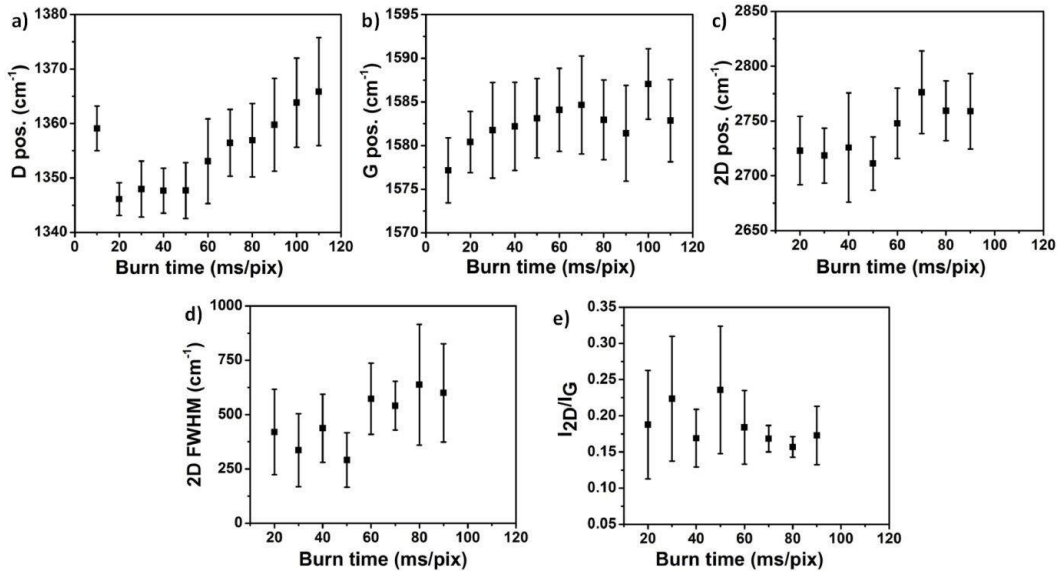


Figure S2.5. Variation of D,G and 2D peak position (a-c), 2D FWHM (d) and I_{2D}/I_G (e) trend measured from Raman spectra collected for LIG electrodes written in the interval 10 -120 ms/pix.

XPS Analysis

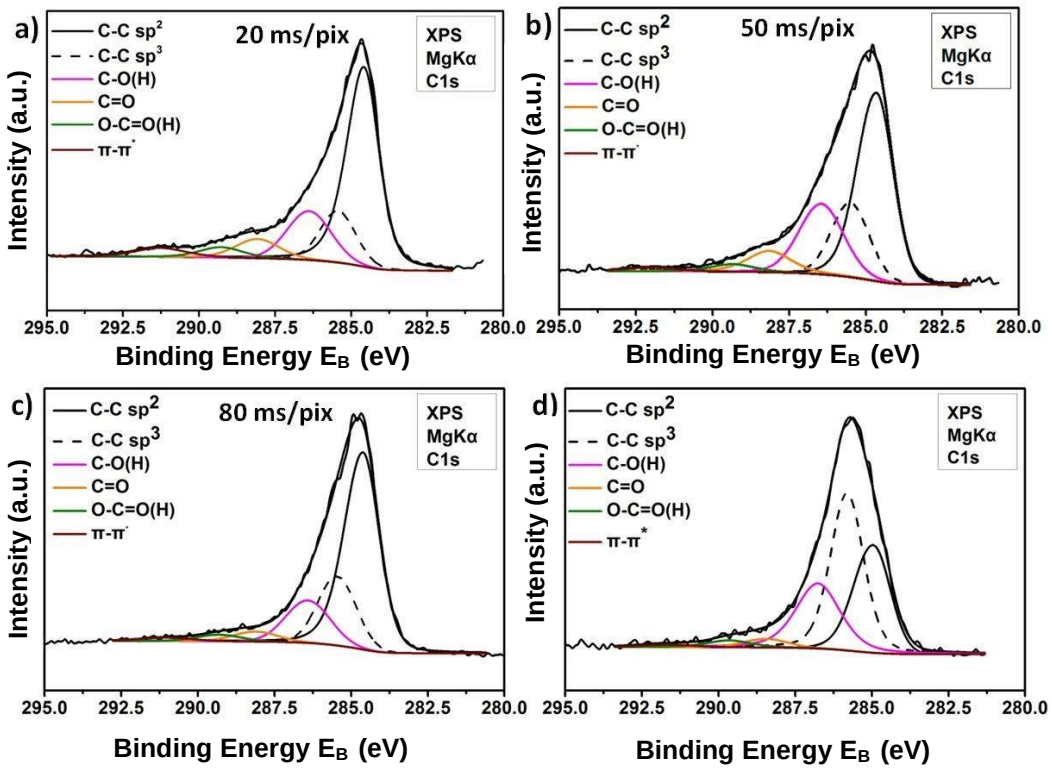


Figure S2.6. Deconvoluted C1s XPS peak of LIG electrodes fabricated at a) 20, b) 50, c) 80 and d) 110 ms/pix laser burn times.

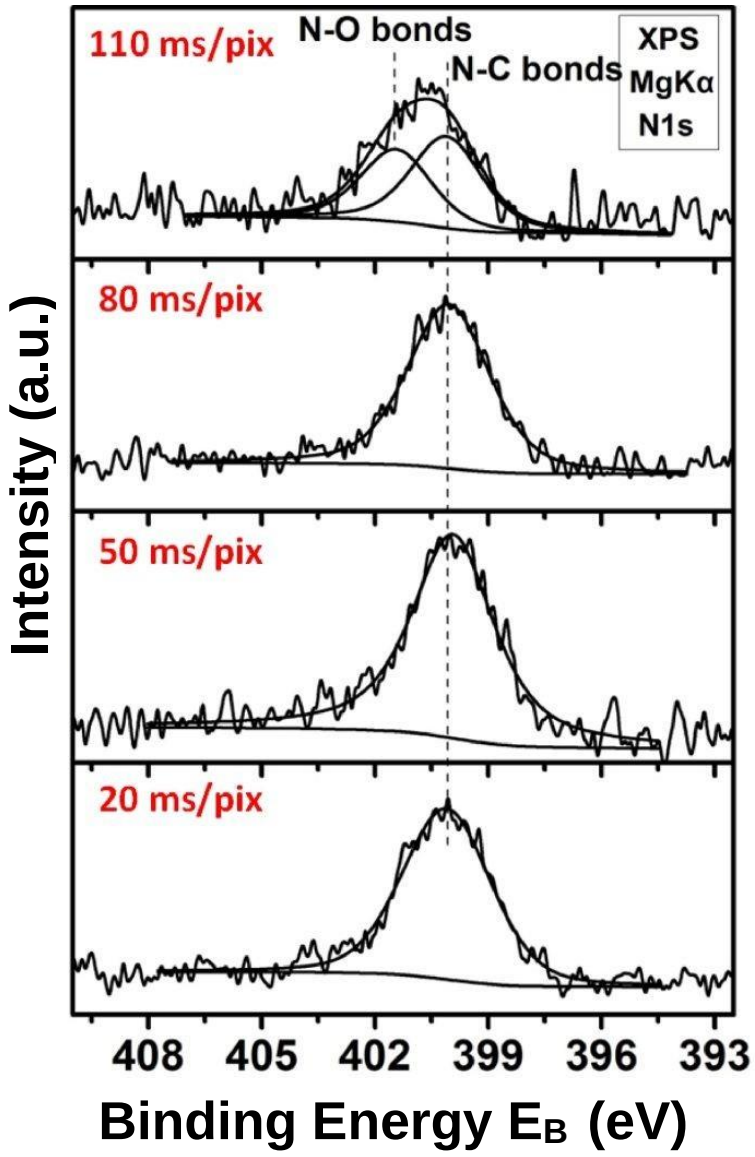


Figure S2.7. Deconvoluted N1s XPS peak of LIG electrodes fabricated at 20, 50, 80 and 110 ms/pix laser burn times.

Electrochemical setup

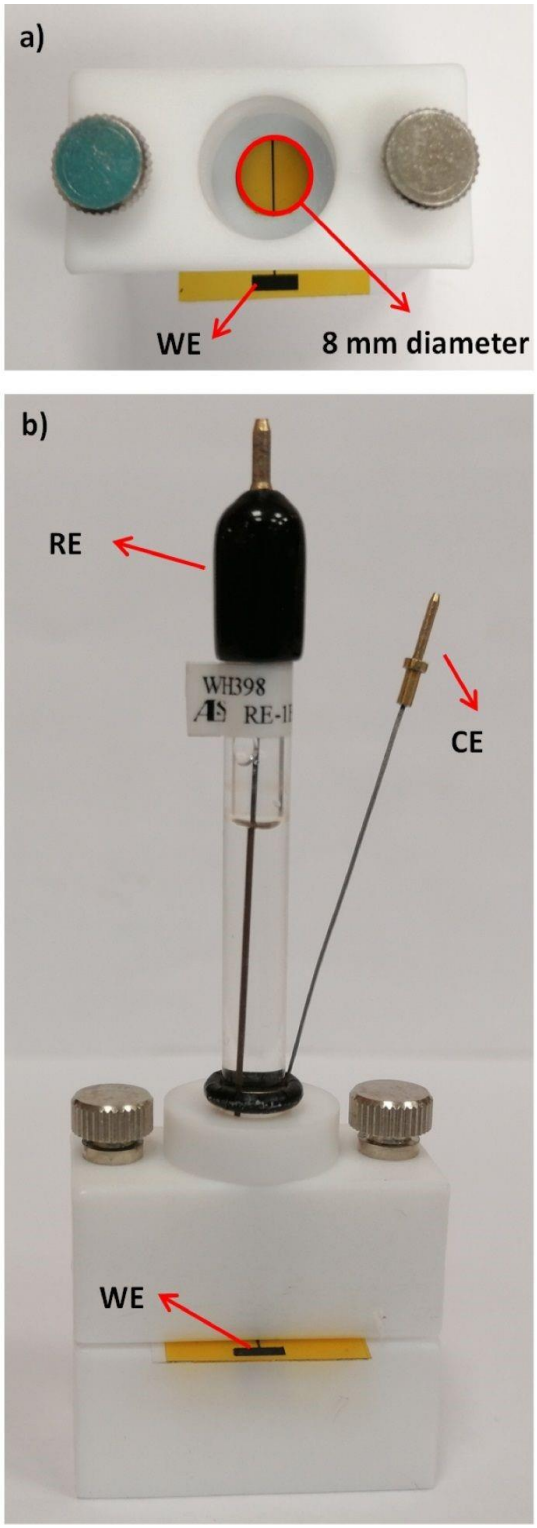


Figure S2.8. Photographs of a) one electrode electrochemical platform assembled in a Teflon electrochemical cell: b) complete electrochemical cell showing LIG working electrode (WE), Ag/AgCl reference electrode (RE) and Pt wire counter electrode (CE). Free domain photographs courtesy of author Eoghan Vaughan.

Cyclic Voltammetry

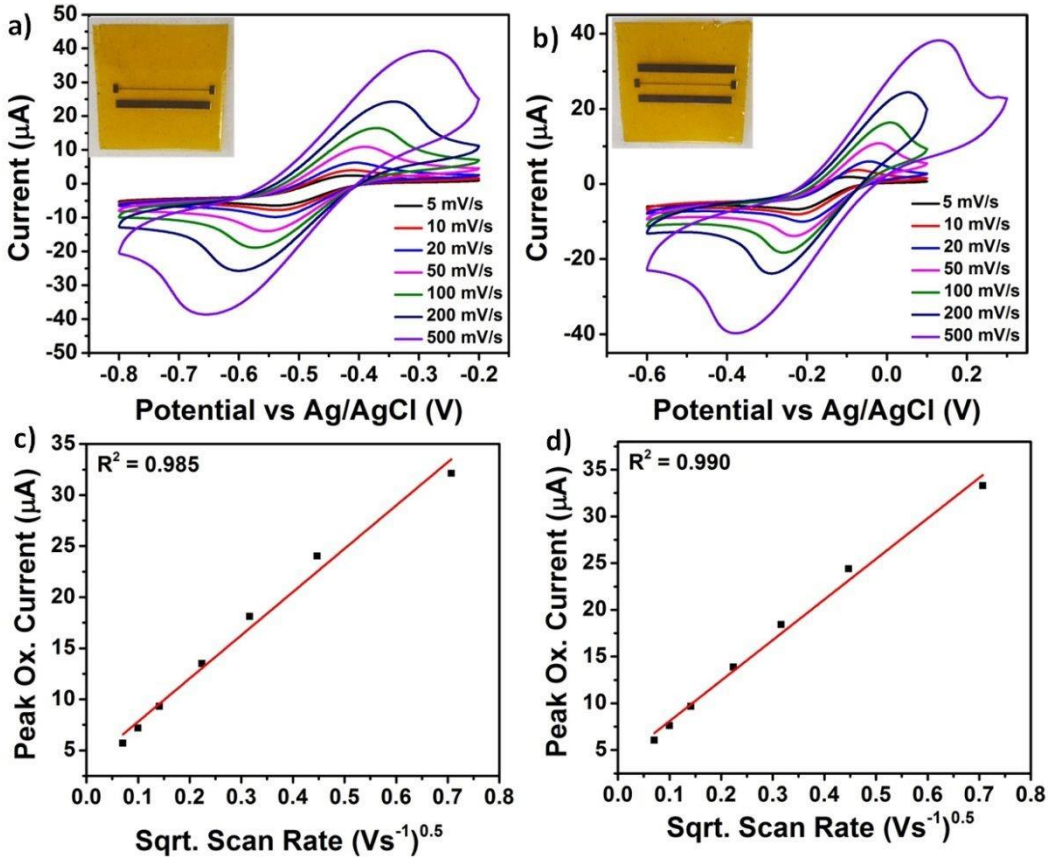


Figure S2.9. Cyclic voltammograms of 50 ms/pix LIG electrodes for 5 mM $Ru(NH_3)_6^{3+/2+}$ in 0.1 M KCl solution as supporting electrolyte recorded with a) LIG working and counter electrode and Pt wire as reference electrode; b) all carbon system. Insets: photographs of the LIG electrodes; c-d) Peak oxidation current *vs* square root of scan rate for a-b).

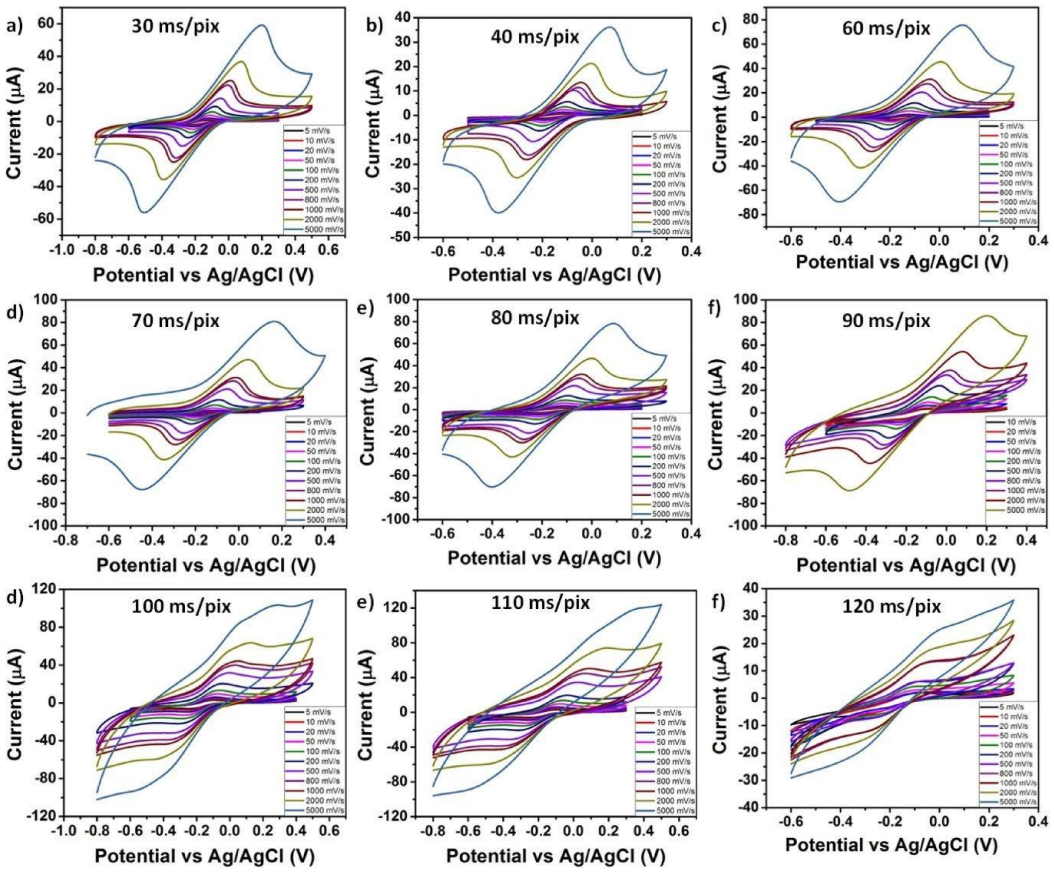


Figure S2.10. Cyclic voltammograms of LIG electrodes written between 30 and 120 ms/pix burn times (a-f) for 5 mM $Ru(NH_3)_6^{3+/2+}$ in 0.1 M KCl solution as supporting electrolyte.

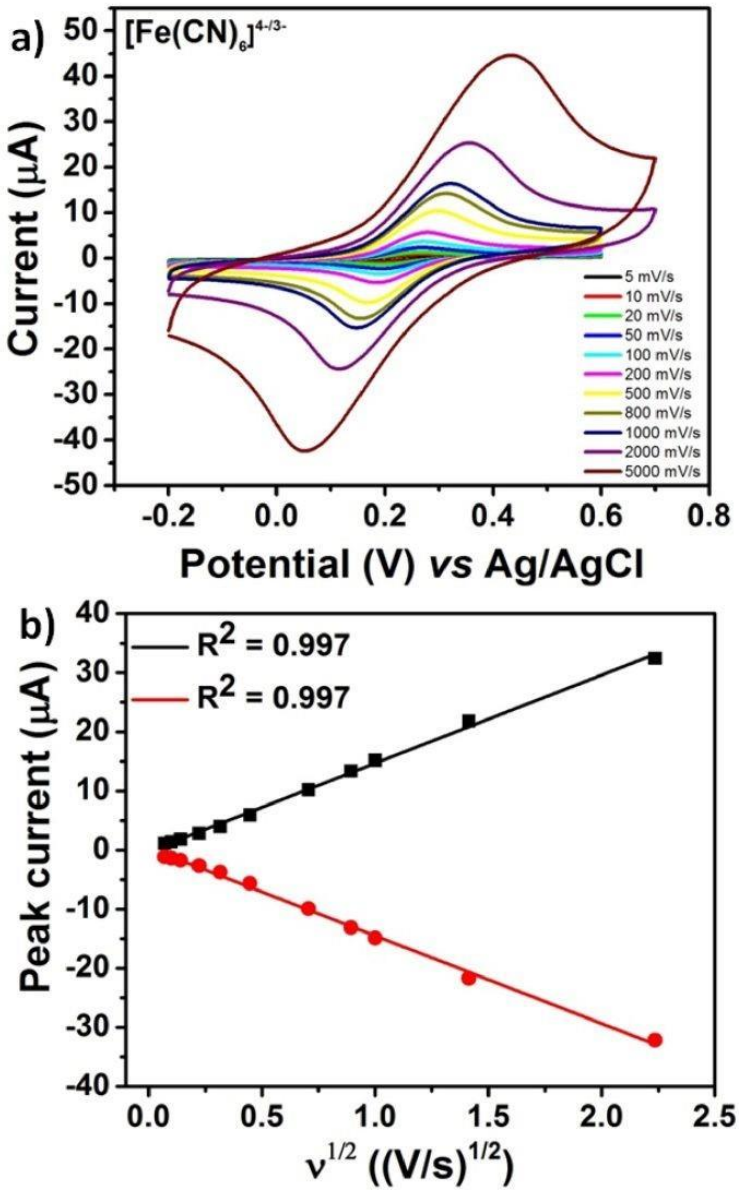


Figure S2.11. a) Cyclic voltammograms of LIG electrode 50 ms/pix at different scan rates in 5 mM $Fe(CN)_6^{3-/4-}$/ 0.1 M KCl; b) Current peak n values *vs* square root of potential scan rate.

Chapter 3: Porous 3D graphene from sustainable materials: laser graphitization of chitosan

In press publication:

Larrigy, C. et al. Porous 3D graphene from sustainable materials: laser graphitization of chitosan. Adv. Mater. Technol. doi:10.1002/admt.202201228 {in press}

Author list:

Cathal Larrigy, Micheal Burke, Alessandra Imbrogno, Eoghan Vaughan, Chiara Santillo, Marino Lavorgna, Labrini Sygellou, George Paterakis, Costas Galiotis, Daniela Iacopino, and Aidan J. Quinn.

3.1 Abstract

Laser-fabrication of graphene from cellulose-based feedstock materials often requires extensive pre-processing. This work demonstrates laser fabrication of porous, 3D graphene carbon from a new class of marine-based sustainable materials – chitosan biopolymers. The biopolymer films contain only chitosan, acetic acid, glycerol and water. FTIR studies indicate that the cured chitosan films still retain a significant water content (~30%), enabling production of flexible films. A simple 3-step laser fabrication process is presented using low-cost infrared (CO_2, 2.1 W) and visible (405 nm, 0.5 W) hobbyist laser engravers. Transient electrochemical detection of an inner sphere redox molecule is demonstrated using a graphene-like carbon working electrode fabricated on a water-soluble chitosan substrate.

3.2 Introduction

Graphene-like materials are promising candidates for the development of electrodes for ubiquitous sensing and Internet of Things applications due to good electrical conductivity, versatility of design and chemical functionalization, leading to their possible integration into physical, chemical and biological sensors.[1–3] Sustainable development goals mandate that substrate and device materials for ubiquitous sensors must have a low environmental footprint throughout their entire life cycle, including low energy production and biodegradability/compostability at end of life. Laser graphitization methods offer a promising alternative to conventional mechanical exfoliation or chemical vapor deposition for scalable fabrication of graphitic carbon electrodes and devices.[4] Specifically, Tour and co-workers rejuvenated this field through direct-write fabrication of porous 3D graphene electrodes on flexible substrates under ambient conditions by infrared laser irradiation of synthetic polyimide (trade name "Kapton").[5–7] This method can be used with commercial and also inexpensive hobbyist laser engravers (both infrared and visible/near-UV), yielding high precision electrode patterns in minutes under ambient conditions, with exciting demonstrations of energy storage and sensing functionalities.[8–10]

However, fabrication of low environmental footprint sensors will require sustainable feedstock materials. Tour and co-workers have demonstrated laser-fabricated graphene on lignin-containing, cellulose-based biomaterials (cork, potato skins, coconut shells) by multiple lasing using a CO_2 laser. The proposed formation mechanism involved the conversion of a carbon precursor to amorphous carbon during the first lasing step(s) followed by conversion to graphene during subsequent lasing step(s). Tour *et al.* noted that simply increasing the laser power was not

successful due to ablation of the substrate material. However, direct lasing of wood materials under ambient conditions led to "ashing" decomposition due to local oxygen, thus laser graphitization required an inert atmosphere.[11] Other groups have reported laser graphitization under ambient conditions using paperboard and TEMPO-modified cellulose nanofiber feedstocks.[12–14] The observed graphitization of the cellulose nanofibers with lower rates of decomposition from ablation and/or ashing was attributed to two factors. Firstly, moisture evaporation during laser irradiation could lower the local temperature and prevent ablation. Secondly, the presence of sodium ions could lower the activation energy of the dehydration step, enabling growth of carbonaceous materials that could be transformed to graphene-like carbon at higher temperatures.

Many other laser graphitization routes using wood-based feedstocks also required significant additional process steps or constraints. These included inert atmosphere,[15,16] soaking in metallic salts,[17,18] treatment with flame retardants, repeated charring to form a graphitic precursor, or significant dehydration.[18] These methods were often combined with a variety of laser treatments, including multi-stage lasing,[19] defocus lasing,[19] ultra-short laser pulses,[11,18,20] or combinations thereof to form graphitic structures. For some phenolic resin feedstocks, dye additives were required to improve the efficiency of the photophysical laser graphitization process.[21]

Here we report on a new laser graphitization route based on sustainable marine-derived feedstock materials – chitosan bioplastics. Chitosan, a copolymer of β[1,4]-linked 2-acetamido-2-deoxy-D-glucopyranose and 2-amino-2-deoxy-D-glucopyranose, obtained by chemical or enzymatic deacetylation of chitin, is one of the most abundant natural polymers on earth.[22] Chitosan's attractive properties

include high porosity; biodegradability; predictable degradation rate; structural integrity and non-toxicity to cells.[23,24] Its rich complexation and functionalization chemistry offer versatile opportunities for sensing applications,[25,26] and as a sustainable alternative for food packaging.[27,28] Interestingly, electrochemical sensors were recently fabricated on chitosan-based films by screen printing techniques and tested towards future wearable sensing applications. The electrochemical devices showed good electrochemical response, suitable Young Modulus and biocompatibility.[29]

Chitosan represents an exciting addition to the range of sustainable cellulose-derived feedstocks reported previously, in that it can be prepared as a flexible, stretchable bioplastic, offering the potential for fabrication of porous 3D graphene electrodes on conformal substrates. Here we report a simple, three-step laser process for fabrication of 3D porous graphene carbon from natural feedstock materials (chitosan, acetic acid and glycerol). We also present initial demonstrations of transient electrochemical detection using dissolvable electrodes.

3.3 Results and Discussion

Figure 3.1a-d shows a schematic process flow for the 3-step laser-graphitization process. The chitosan biopolymer formulation (chitosan, acetic acid, glycerol plasticizer and water) is sonicated, then cast or doctor-bladed onto glass substrates, followed by curing at room temperature for 3 days or at 50^{o}C for 10 hours (see Experimental Section). The films are transparent (Figure 3.1a inset) with a slight yellow hue. For our chitosan-based biopolymers, single- or multiple lasing steps using only one laser wavelength (either 10.6 µm or 405 nm) did not result in formation of graphitic carbon films. As previously reported, for substrates that proved difficult to graphitize by single pass lasing, and instead resulted in ablation, (i.e., lignin-containing, cellulose-based biomaterials) often required a multiple-pass lasing process. However, this required a heavily carbonized region to occur. [19] Figure 3.1e shows that regions which were patterned twice by the 10.6 µm CO_2 laser at 2.8 W (i.e., Step 1 and Step 3), but not were exposed to the 0.5 W 405 nm diode laser (Step 2), showed a change in hue but no optical evidence of graphitization. By contrast, regions which underwent a 2-step process comprising a pre-conditioning step with the CO_2 laser (Step 1) followed by patterning with the 405 nm diode laser (Step 2) showed a deep black color (Figure 3.1e) with 3D micro/nanoporous morphology evident in SEM micrographs (Figure 3.1h, i). Two-step processed material, however, was not entirely converted into a graphitic material, exhibiting a high level of disorder, which was apparent in the corresponding transmission electron microscopy (figure S3.1), as the material appeared to be “wax-like” and did not exhibit a wrinkle structure, indicative of some variety of graphitic material. This suggests a more amorphous carbon material present.

Chitosan formulations treated with a 3-step process (10.6 µm, 405 nm, 10.6 µm) showed increased nanostructuring of the hierarchical porous surface (Figure 3.1j, k and Figure S3.3i). Meanwhile, the TEM micrographs (figure S3.2) of 3-step process material displayed a crystalline structure with a typical wrinkle patterning representative of a graphitic material. This combined with overlapping and disorganized regions of carbon layers suggest the material formed was similar to that of a turbostratic graphite material.

The first laser exposure (Step 1) is an essential prerequisite and will be discussed in more detail later in conjunction with FTIR analysis of as-cured and 1-step processed films.

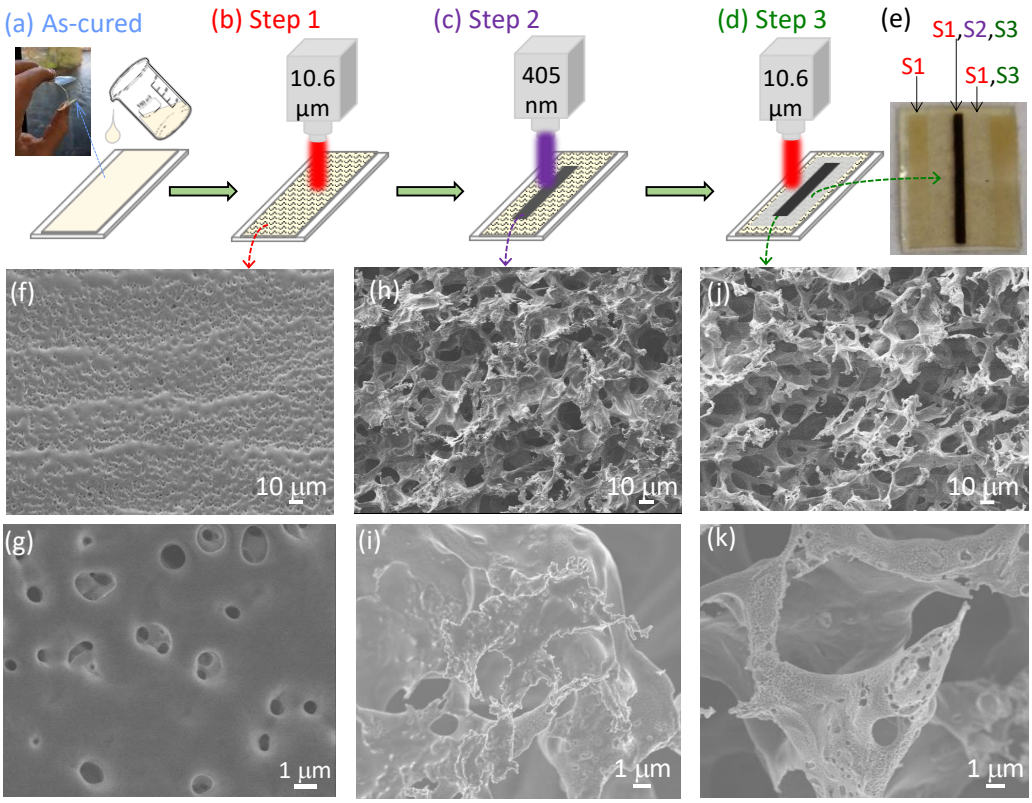


Figure 3.1. Patterning and morphology of chitosan graphene-like carbon electrodes. Schematic process flow, comprising: (a) Deposition and curing of the chitosan formulation. Inset: photo of an as-cured flexible film; (b) Step 1: pre-conditioning a specific region with a 10.6 µm CO_2 laser; (c) Step 2: direct-write graphitization of an electrode pattern within this region using a 405 nm laser; (d) Step-3 post-processing with a 10.6 µm CO_2 laser to form graphene-like carbon. (e) Photo of a typical sample showing the optical contrast associated with the various stages. (f-k) Scanning electron micrographs (SEMs) showing the morphology resulting from the different laser processing steps: (f, g) Quasi-planar film with hierarchical pore network following Step 1; (h,i) High porosity, 3-D morphology following Step 2; (j,k) Further increases in porosity and surface roughness following Step 3.

Raman spectroscopy of the two-step laser-processed films (**Figure 3.2a**) showed two broad peaks: the *G* mode centered close to 1580 cm^{-1}, assigned to in-plane bond

stretching of pairs of sp^2 carbon atoms and the *D* mode centered close to 1350 cm^{-1}, assigned to a defect-activated breathing mode of six-atom rings (A_{1g} symmetry).[30] The "2-step" spectra are consistent with formation of nanocrystalline graphitic carbon domains in an amorphous carbon matrix.[30,31] These 2-step data are qualitatively similar to previous Raman spectra measured on graphitic carbon formed by laser irradiation of polyimide using the same 500 mW 405 nm laser at similar dwell times (110 ms/pixel).[7] XPS measurements of those graphitic carbon films revealed a significant fraction of sp^3 carbon.[7]

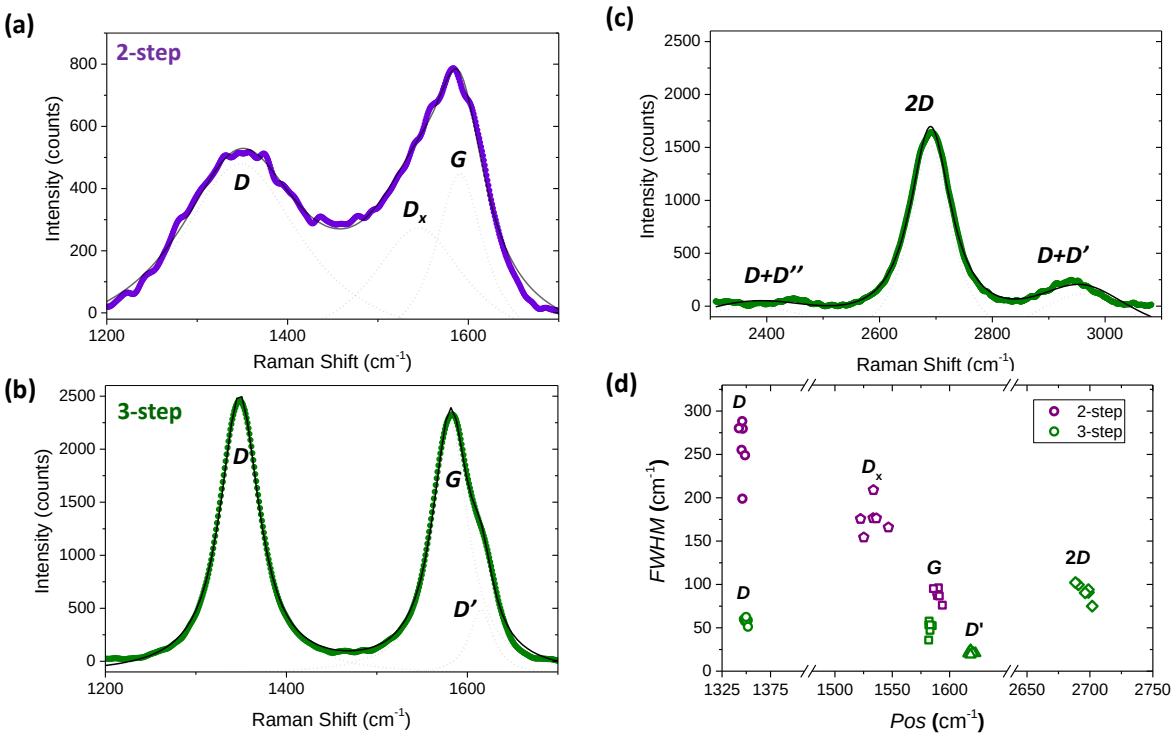


Figure 3.2. First order peaks in Raman spectra of laser-graphitized chitosan films following (a) 2-step processing; (b) 3-step processing. (c) Second order Raman peaks for the 3-step processed film. (d) Lorentzian fit values for full-width at half maximum intensity (*FWHM*) plotted vs peak position.

No clear peaks were observed in the 2nd order Raman region (2300 – 3100 cm^{-1}) for the 2-step processed chitosan films, again consistent with formation of nanocrystalline graphitic (but not graphene-like) carbon inclusions in an amorphous carbon matrix. By contrast, chitosan formulations treated with a three-step laser process (10.6 µm, 405 nm, 10.6 µm) showed distinct *D* and *G* peaks (Figure 3.2b), as well as a sharp *2D* peak centered close to 2700 cm^{-1} (Figure 3.2c). These data are consistent with formation of laser-fabricated graphene-like carbon.

Table 3.1. Results for Lorentzian fits to Raman spectra (Figure 3.2a-c)

Peak	*D*		*D_x*		*G*		*D'*		*2D*	
	Pos [a] [cm^{-1}]	*FWHM* [b] [cm^{-1}]	*Pos* [cm^{-1}]	*FWHM* [cm^{-1}]	*Pos* [cm^{-1}]	*FWHM* [cm^{-1}]	*Pos* [cm^{-1}]	*FWHM* [cm^{-1}]	*Pos* [cm^{-1}]	*FWHM* [cm^{-1}]
2-step	1348	167	1544± 4 [c]	128± 6	1591	66±4	-	-	-	-
3-step	1348	52	-	-	1581	48	1615	32±2	2690	90±1

[a] *Pos*: Peak Centre; [b] *FWHM*: Full-width at half-maximum intensity; [c] Fit results quoted as *value* ± *standard error* (standard error not quoted if < 1 cm^{-1}).

To compare the 1st order Raman data for the 2-step vs 3-step material, three unconstrained Lorentzian peaks were used to fit each dataset over the 1200-1700 cm^{-1} range; see Table 1. The fit to the 2-step data (Figure 3.2a) reveals a broad *D* peak, i.e., large full-width at half-maximum, *FWHM*(*D*) ~167 cm^{-1}, and also the presence of another peak (termed D_x) located between the *D* and *G* peaks. Similar Raman data have been reported for disordered carbon (including soot and conductive carbon blacks).[32] Figure 3.2b shows the fit to the 3-step data. The maximum in the *D* region can be fit with a single, sharp Lorentzian (*FWHM*(*D*) ~52 cm^{-1}), indicative of increased order relative to the 2-step processed material. The peak close to 1580 cm^{-1} represents a convolution of the *G* peak with a *D*' peak. [33] In early Raman studies of graphite, *D*' peak signatures were observed in high-quality polycrystalline graphite and also by creating defects in natural graphite single crystals.[31,34] *D*' shoulders similar to the data shown in Figure 3.2b were observed in polycrystalline graphite with domain sizes (or scattering coherence lengths) ~ 7-12 nm.[31,34] Again, the sharp G peak and presence of a *D*' peak indicate increased order in the 3-step processed material.

Detailed studies by Casiraghi and co-workers established empirical relationships between the intensity ratios of the *D* to *D*' peaks and the nature of the defects for exfoliated monolayer graphene with deliberately introduced defects, and also for natural graphite: $I(D)/I(D') \sim 13$ for sp^3 defects; $I(D)/I(D') \sim 7$ for vacancy defects and $I(D)/I(D') \sim 3.5$ for boundary defects in natural graphite. [35] For the 3-step spectra, 4 of the 6 locations showed $I(D)/I(D')$ values between 3.5 and 7, again consistent with low disorder. Figure 3.2c shows the corresponding Raman data for the 2300 – 3100 cm^{-1} range for the 3-step processed material. Again, three unconstrained Lorentzians were used to fit the data. A sharp *2D* peak is evident, with two weaker peaks which can be ascribed to *D*+*D*'' and *D*+*D*' modes, respectively.[33] The *FWHM*(*2D*) value (90 cm^{-1}) compares well with the minimum values for laser-fabricated graphene-like carbon formed from polyimide using single-step processes: *FWHM*(*2D*) ~ 120 cm^{-1} using a 405 nm laser (500 mW) and *FWHM*(*2D*) ~ 60 cm^{-1} using a 10.6 μm CO_2 laser.[7]

Figure 3.2d shows collated fit results for 2-step and 3-step processed regions on the same chitosan film (Figure 3.1e). For the 2-step process, 7 spectra were acquired at different locations across 2 separate regions, while 6 spectra were acquired over 2 regions for the 3-step process. The results show the same trends described above for the individual peak fits for the 3-step vs the 2-step process: substantially reduced *FWHM*(*D*), lower *FWHM*(*G*) and the emergence of strong, sharp *2D* peaks with *FWHM*(2*D*) < 100 cm^{-1}. The lower values for the *G*:*D* peak intensity ratio (I_D/I_G) and peak area ratio (A_D/A_G) for the 3-step vs the 2-step process are also consistent with increased order (Figure S3.5).

For the 3-step processed chitosan, the well-resolved, narrow *D*, *G* and *2D* lineshapes are consistent with formation of graphene-like carbon with relatively low disorder

(albeit with greater disorder than for laser-graphitized polyimide). The symmetric *2D* lineshape contrasts with the asymmetric *2D* peak reported for Bernal-stacked (ABAB) multilayer graphene or graphite,[36,37] and suggests this laser-fabricated graphene-like carbon comprises few-layer graphene structures with rotational and/or vertical stacking disorder. This additionally can be confirmed by transmission electron microscope imagery (figure S3.2). TEM data (figure S3.2) show a typical wrinkle structure representative of a graphitic material with layer spacing ~0.34 nm, as expected for a graphitic material. The overall structure of the LIG observable in the figure S3.2b highlights the unstructured, and overlapping of the carbon fibers, indicating the material is similar to a turbostratic graphite.

The near-surface composition for material from 3-step vs 2-step processed films was investigated using X-ray photoelectron spectroscopy (XPS). Figure 3.3a shows the carbon 1*s* data for 2-step processed material. The data were fitted using three peaks (solid black lines) plus a background curve (dashed curve), see Table 2. The three components were assigned to C-C and C-H bonds; C-O bonds; and N–C=O bonds, respectively.[38]

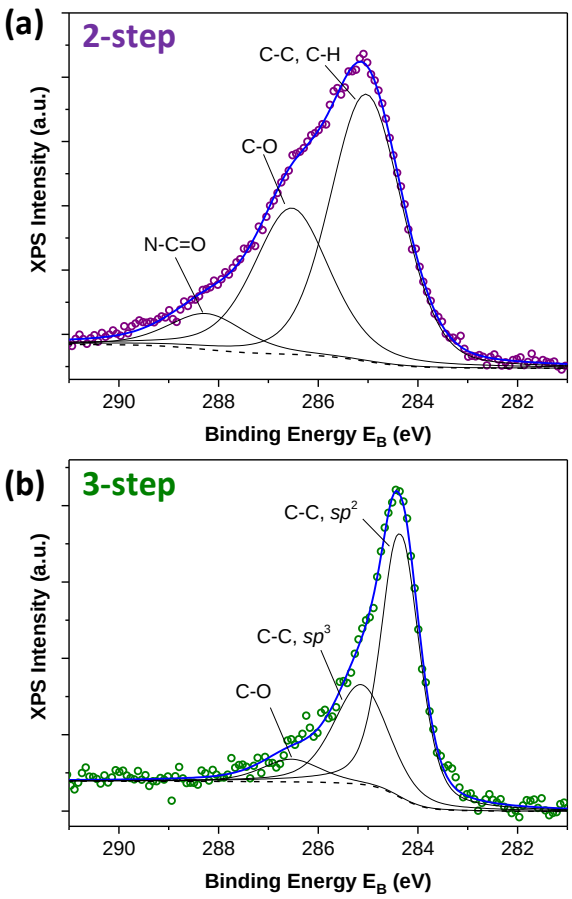


Figure 3.3. C1*s* XPS data (circles) of (a) 2-step laser-processed chitosan; (b) 3-step laser-processed chitosan. The fit for each spectrum (colored line) was deconvoluted into 3 peaks (solid black lines) plus a background term (dashed line).

For the 3-step processed material, a much narrower C1s spectrum was observed (Figure 3.3b). The three fit peaks were assigned to sp^2 hybridized C-C bonds, sp^3 C-C bonds and C-O bonds, respectively. In contrast to the data for the 2-step material, no N–C=O peak was observed, suggesting a significant reduction in the number of amide groups. The fit data in Table 2 highlight that the C-O peak for the 3-step material (10% of C 1*s* peak) is much weaker than for the 2-step material (33% of C 1*s* peak). Considering both spectra, there is a significant increase in the ratio of sp^2 to sp^3 carbon for the 3-step processed material.

XPS measurements in the energy range corresponding to the nitrogen 1s peak (Figure S3.6) showed a clear maximum for the 2-step material (*BE*: 400 eV), which was assigned to chitosan amine and amide bonds.[39] Only traces of nitrogen were detected for the 3-step material. The C:N and C:O atomic ratios for both 2-step processed, and 3-step processed chitosan laser graphitized material were calculated from the peak areas of the C 1*s*, and N 1*s* peaks divided by the Scofield sensitivity factors and the transmission function of the analyzer, respectively. For the 3-step material, contributions from the underlying indium tin oxide (ITO) substrate used for the XPS measurements were detected so the exact oxygen composition could not be calculated. However, given the diminished C–O peak contribution to the carbon 1*s* spectrum for the 3-step vs the 2-step material, it is clear that the oxygen content for the 3-step material is substantially reduced. The C 1*s* to N 1s peak area ratio for the 3-step material (1:0.03) is also substantially reduced vs the 2-step material (1:0.12) indicating a clear reduction in nitrogen content.

Additionally, the conversion to laser-induced graphene, and reduction in disorder arising from subsequent laser treatments can be seen in thermogravimetric analysis (TGA) measurements (figure S3.7), transmission electron microscopy images (figure S3.1), and X-ray diffraction measurements (figure S3.8) of the various stages. TGA highlight the presence of bound water in chitosan heavier films (figure S3.7a, b) as noted from thermal degradation at ~70^{o}C and ~150 ^{o}C, which shows less degradation in carbon heavier films. Also notable is the removal of the bulk of chitosan in film in favor of disorder carbon (figure S3.7c), and laser-induced graphitic structures (figure S7d), with the typical thermal degradation of chitosan occurring ~265 ^{o}C. Comparing the TEM micrographs of 2-step (figure S3.1) and 3-step material (figure S3.2) further insights into the change in disorder can be examined. In 2-step, due to the high level

of disorder, a high amount of distortion was observed, as it was a waxy like substance. Whereas, 3-step, shows a typical wrinkle structure representative of a graphitic structure.

Taken together with the fit results for the Raman data (Figure 3.2d), this indicates that the 2-step processed material comprises nanocrystalline graphitic carbon inclusions within an amorphous carbon matrix.[30] The XPS and Raman data indicate that the 3-step processing leads to an increase in the relative abundance of sp^2 graphitic carbon and the sharp *2D* Raman peak provides clear evidence for the emergence of graphene-like carbon.[33] These data provide encouraging evidence for the potential to form graphene-like carbon electrodes and sensors from marine-derived sustainable materials.

Table 3.2. Fit results from XPS Data

	Composition Ratios		Percentage contribution to C 1*s* peak					
	C:N [1:*x*]	C:O [1:*x*]		C-C sp^2	C-C sp^3	C-C	C-O	N-C=O
Elemental composition ratios from chitosan molecular formula ($C_{56}H_{103}N_9O_{39}$)	0.16	0.70						
2-step process: Elemental composition ratios from XPS C,N,O 1*s* peak areas	0.12	0.30	2-step process: % contribution to C 1s	-	-	58%	33%	9%
			Binding Energy (E_B)	-	-	285.0 eV	286.6 eV	288.3 eV
3-step process: Elemental composition ratios from XPS peak areas	0.03	N/A [a)]	3-step process: % contribution to C 1s	65%	25%	-	10%	-
			E_B	284.4 eV	285.2 eV	-	286.6 eV	-

[a)] Oxygen signal from underlying ITO substrate detected so exact oxygen content could not be calculated.

Concerning the need for a 3-step laser process to form graphene-like carbon from chitosan, a number of factors may contribute to this. While earlier work has shown that graphene-like carbon can be formed by single-step direct writing of polyimide in air using a 500 mW 405 nm laser or a 10.6 µm CO_2 laser,[4,7] this chitosan formulation requires a multi-step process and requires both wavelengths. One factor that may influence the laser graphitization process is the water content of the films. Figure 3.3a shows FTIR spectra averaged from multiple locations across two separate regions on the same film – one unprocessed (i.e., as-cured) region and another region which was exposed to a 10.6 µm CO_2 laser (1-step process). Both spectra show good agreement with published work on chitosan and chitosan acetate films,[40–44] see Table 3.3.

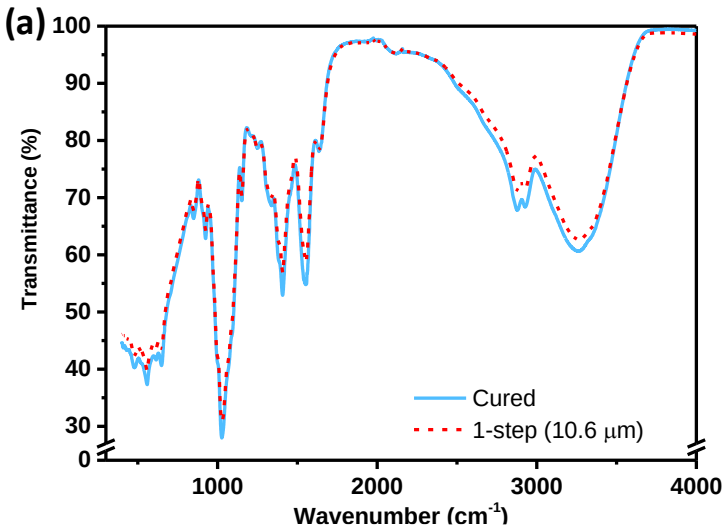


Figure 3.4. FTIR spectra for a region of an as-cured chitosan film (solid curve) and for a different region from the same film which was exposed to 1-step laser treatment with a 10.6 μm CO_2 laser (dashed curve). Each spectrum is the average of individual spectra acquired at 5 different locations across the as-cured and 1-step treated regions, respectively.

Table 3. Peak assignations for FTIR spectra shown in Figure 3.4. [40–44]

Peak position or range [cm^{-1}]	Assignation	Intensity
2600–3600	O−H stretching vibrations of interstitial sorbed water	Strong
2800–3000	C−H stretching vibrations	Moderate
3000–3600	O−H stretching vibrations (pyranose ring hydroxyl groups)	Weak
3000–3300	N−H stretching vibrations	Weak
1645	carbonyl stretching of secondary amides (Amide I band)	Weak
1500–1600 1540 1556 1558 1588	Convolution of: 'NH_3^+ band Carboxylate –COO^- band Amide II band NH_2 deformation peak	Strong
1410	–CH_2 bending	
1390	–CH_3 symmetrical deformation	
1025	Skeletal vibration of C-O stretching	Strong

The broad IR absorbance in the ~2600–3600 cm^{-1} region is dominated by the O−H stretching vibrations of interstitial sorbed water,[40] but also contains additional contributions, see Table 3.3. Interstitial water is usually classified into (i) non-freezable bound water (ii) freezable bound water and (iii) freezable free (bulk) water.[40,43,45] In particular, the data show strong similarities with recent work on hydrated water structure in chitosan films.[40,43] Qiao *et al.* recently reported FTIR data for hydrated chitosan films as function of water content (up to 27%).[43] The broad feature (~3000–3600 cm^{-1}) for the as-cured spectrum with minimum transmittance close to 3280 cm^{-1} suggests the presence of a significant water content (>27%), as expected for a film cured under ambient conditions.[43] These interstitial networks of water molecules (including pentamers, distorted pentamers and tetramers), which are linked by transient hydrogen bonds, interact with the polysaccharide backbone and can have a significant influence on the mechanical properties of the biopolymer, including flexibility and stretchability.[40]

The appreciable increase in transmission over the ~3000–3600 cm^{-1} range between the as-cured and 1-step processed chitosan films suggest that local desorption of water is one potential contributory factor to the increase in transmission following exposure to the 10.6 µm laser pre-conditioning step. The increased transmission for the peaks close to 1550 cm^{-1} and 1400 cm^{-1} after 1-step processing was also observed by Qiao et al. for chitosan films with reduced water content and was attributed to reduced hydrogen-bonded interactions between the chitosan side-groups and interstitial networks of water molecules.[43]

Thermogravimetric analysis of the chitosan films additionally shows the dehydration of bound and semi bound water (figure S3.7). Thermal degradation at ~70^{o}C, occurring due to surface level semi- bound water molecules and ~150 ^{o}C, occurring due to higher bound interstitial water, is indicative of this dehydration process. Notably, for 2-step (figure S3.7c) and 3-step processed regions (figure S3.7d), the rate of thermal degradation is significantly lower than as-cured (figure S3.7a) and 1-step (figure S3.7b), like due to film undergoing a dehydration and conversion process from laser induction into a graphitized material.

SEM data acquired at the boundary between an as-cured region and a 1-step processed region show significant morphology differences (Figure S3.9a). The as-cured region shows a relatively smooth surface with higher magnification images showing island-like features several microns in diameter (Figure S3.9b). The 1-step processed regions shows surface structuring (~ 200 µm feature sizes) likely due to laser-induced melting and/or ablation (Figure S3.9d, e). Higher magnification images of the 1-step processed region (Figure 3.3f, g) show a high density of pores at the surface with pore diameters ranging from 200 nm to ~ 1 µm. These data, together with the FTIR results suggest that the first laser step may result in local superheating and desorption of interstitial water leading to formation of a micro/nano-pore network. This dehydration and

increased surface area could also improve the efficiency of the subsequent graphitization step using the 405 nm laser. As mentioned above, it was not possible to form graphitic carbon by single or multiple exposures of the chitosan films using only the 405 nm laser. Site-specific dehydration and pore formation by CO_2 laser-preconditioning (Step 1) as part of a laser graphitization process may thus offer a versatile route towards integration of high-performance carbon electrodes into conformal or flexible bioplastic substrates. This local dehydration offers advantages over non-local methods such as thermal annealing which can compromise mechanical integrity. It is interesting that a combination of infrared and visible laser sources is required to form graphene-like carbon, indicating that both photophysical and photothermal processes play essential roles at specific stages in the process.

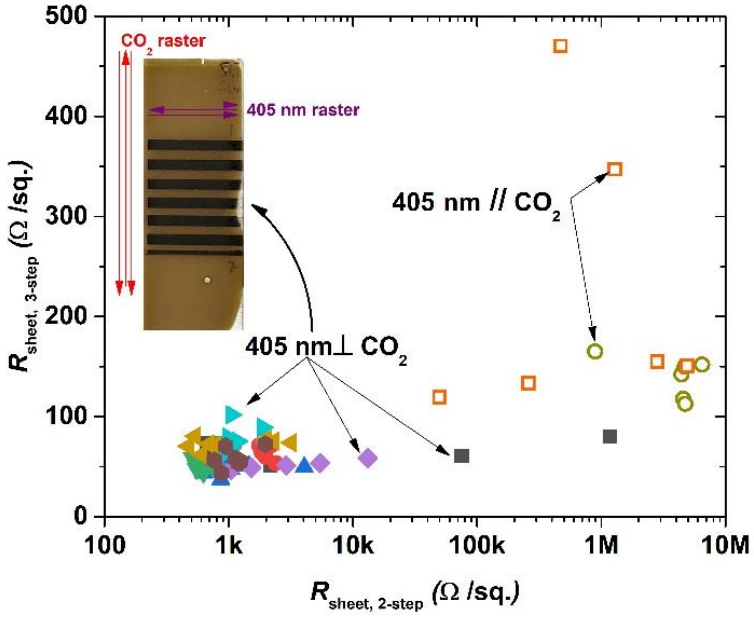


Figure 3.5. Sheet resistance data for bar structures (inset photo) following 3 laser processing steps ($R_{\text{sheet, 3-step}}$), plotted vs. data following 2 laser processing steps ($R_{\text{sheet, 2-step}}$). Open symbols: Data from 12 devices across 2 substrates where the raster direction for the 405 nm laser pattern (Step#2) was parallel to the direction for CO_2 laser pattern (Steps #1 & #3). Filled symbols: Data from 57 devices across 8 substrates where raster direction for 405 nm pattern was perpendicular to raster direction for CO_2 pattern.

Millimetre-scale electrical test structures were fabricated from chitosan films using both two-step and three-step laser graphitization (Figure 3.5, inset). Aspect ratios ≥8 were used to minimize the influence of contact resistance.[46] Initial devices prepared using drop-casting yielded sheet resistances, $R_{\text{sheet}} > 1$ kΩ/sq. for 3-step processed sub-mm structures (Figure S3.10). These values were significantly larger than measured data for graphene-like carbon electrodes formed by laser irradiation of polyimide films using the 405 nm laser, $R_{\text{sheet}} \geq 80$ Ω/sq. for bar structures formed by a single laser pass (~ 120 µm wide),[7] or mm-width bar structures formed by raster-patterned CO_2 laser graphitization of polyimide, $R_{\text{sheet}} \sim 15$ Ω/sq.[46] Two complementary approaches led

to a significant reduction in sheet resistance for the chitosan laser-induced graphene. Firstly, doctor-blading chitosan biofilms onto microscope slides yielded thinner and more uniform films vs drop-casting, with a lower density of macro-scale defects, e.g., bubbles. Measurements taken after two laser processing steps (10.6 μm CO_2, 405 nm) yielded sheet resistances ranging from $R_{\text{sheet, 2-step}} \sim 50$ kΩ/sq. to $R_{\text{sheet, 2-step}} \sim 10$ MΩ/sq. (open symbols in Figure 3.5). After the 3rd laser processing step (10.6 μm CO_2), these devices showed sheet resistances in the range $R_{\text{sheet, 3-step}} \sim 100 – 500$ Ω/sq., with the majority of devices showing $R_{\text{sheet, 3-step}} \sim 100 – 200$ Ω/sq., a significant improvement over devices from drop-cast films. For these drop-cast and doctor-bladed devices, the raster direction for the CO_2 laser processing steps (Step 1 and Step 3) was approximately parallel to the raster direction for the 405 nm laser (Step 2). The large variation in measured values for $R_{\text{sheet, 2-step}}$ (Figure 3.5, open symbols) suggest that structural disorder resulting from overlaying parallel laser raster patterns could lead to formation of a set of quasi-1-dimensional current paths, where the disorder cannot be completely mitigated by the 3rd laser step (also parallel).

To address this issue, a final set of 57 devices across 8 substrates was fabricated using orthogonal raster directions for the 405 nm laser step (Step#2) *vs* the CO_2 laser steps (Steps #1 & #3). In general, these devices showed substantially lower sheet resistances after 2-step processing with $R_{\text{sheet, 2-step}} < 10$ kΩ/sq. for 54 of the 57 devices (Fig. 5, filled symbols). More importantly, the sheet resistance following the final laser step also decreased vs the "parallel-raster" devices with $R_{\text{sheet, 3-step}} \leq 80$ Ω/sq. for 55 of the 57 devices (Figure S3.11), with a minimum measured value $R_{\text{sheet, 3-step}} \sim 37$ Ω/sq. These results suggest that further reductions in sheet resistance may be possible by optimizing the laser patterning process to enable formation of 2-dimensional conduction paths.

Chitosan graphene-like carbon electrodes were also employed for preliminary demonstrations of electrochemical functionality: Cyclic voltammetry of an inner sphere redox molecule, $Fe(CN)_6^{3-/4-}$ in aqueous KCl. Initial experiments on electrodes fabricated from drop-cast chitosan films (Figure S3.12) showed quasi-reversible behaviour. The peak oxidation current ($I_{p,ox}$) increased monotonically but non-linearly with the square root of the scan rate ($\nu^{½}$), possibly due to electrode degradation arising from substrate dissolution (Figure S3.12c) as well as the large access resistance. Recent electrochemistry studies on graphene-like carbon fabricated by irradiating polyimide with a 450 nm laser have demonstrated that the *iR* drop from a large access resistance (~ kΩ) increases the separation between the oxidation and reduction peaks (ΔE_p) and also reduces the peak oxidation current, $I_{p,ox}$.[47]

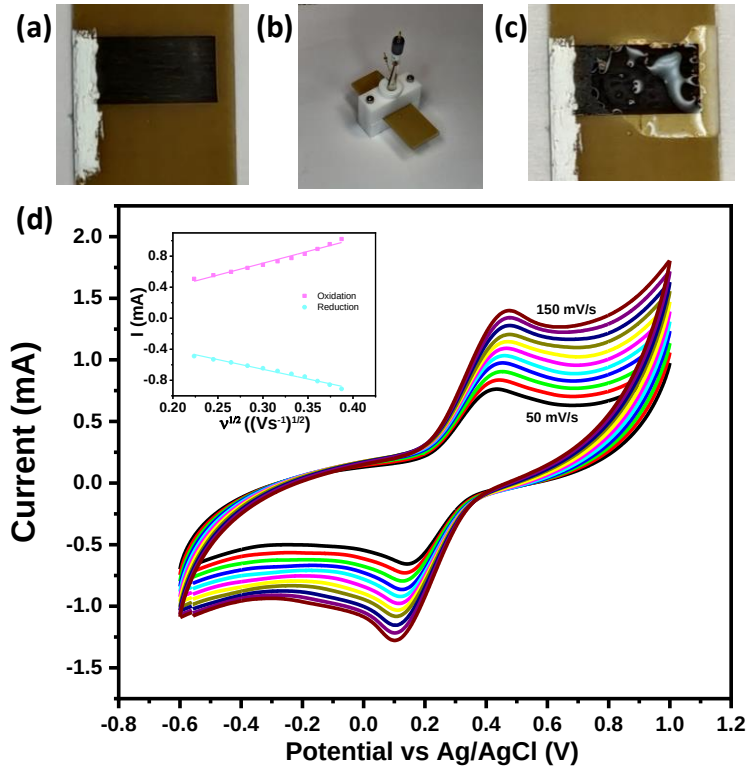


Figure 3.6. Proof of concept demonstration of transient electrochemical sensing using 3-step laser fabricated graphene-like carbon electrodes from a doctor-bladed chitosan biopolymer. Photos of: an as-prepared single working electrode (a); the 3-electrode electrochemical cell (b); the working electrode following ~40 minutes electrochemical cycling (d) cyclic voltammograms from the working electrode in a 5 mM solution of $Fe(CN)_6^{3-/4-}$ in 1 M KCl

Electrochemical performance was improved by utilising thinner doctor-bladed chitosan films and orthogonal laser writing to fabricate electrodes, as described above. The electrode area was also increased to minimize the contact area between the electrolyte and the ungraphitized chitosan substrate (Figure 3.6a-c). Cyclic voltammetry data (Figure 3.6d) showed reversible behaviour with the expected linear relationship for $I_{p,ox}$ vs $\nu^{1/2}$. Using the Randles-Ševčík equation,[48] this yields an effective electrochemical area ~60% larger than the geometric area (81 mm^2 vs 50 mm^2). The electrochemical peak separation (ΔE_p ~ 290 mV at ν= 50 mV/s) is within

the range reported for graphene electrodes on polylactic acid biopolymer substrates (100 – 400 mV),[49] reflecting a kinetic activation barrier for the redox reaction, in addition to *iR* potential drops from the factors mentioned above: access resistance and electrode degradation. While the ΔE_p values are larger than results reported for optimized electrodes derived from synthetic carbon black inks on biopolymer substrates or biomass-derived laser-induced graphene dispersions on glassy carbon supports,[49] these results highlight the potential for direct-write fabrication of compostable or dissolvable graphene-like carbon sensors from sustainable feedstock materials. Our chitosan formulations yield flexible films that are stable in air for more than a year, thus future work will focus on controlling the solubility of the chitosan film through blending and/or neutralization.[50]

3.4 Conclusions

In conclusion, we have developed a new family of sustainable feedstock materials for laser graphitization and have shown how multi-wavelength laser processing can be used for direct-write formation of graphene-like carbon for these aqueous biopolymer formulations. Our results highlight the potential of chitosan-based materials for development of new generations of biodegradable sensors with low environmental footprint across the entire life cycle. These sensors could enable environmentally responsible Internet of Things applications in environmental monitoring, sustainable packaging, and wearable sensors.

3.5 Experimental

Materials. Chitosan (medium molecular weight), acetic acid (> 99.8% purity), glycerol, potassium hexacyanoferrate(III) were purchased from Sigma Aldrich and used without further purification. Milli-Q water (resistivity 18 MΩ.cm) was used throughout the experiments.

Chitosan film preparation. Chitosan films were obtained by dissolving 5 g of chitosan in 100 mL of acetic acid solution (5% v:v), followed by addition of 2 mL of glycerol. The obtained solution was heated at 70°C to homogenize components and sonicated for at least 2 hours to remove trapped air bubbles. The sonicated solution was cast to fill a glass petri dish (100 mm diameter, 20 mm depth), and air dried at room temperature (~16°C) in a laminar flow fume cupboard for 5 days. The thickness of the final dried chitosan film was ca. 0.4 mm. Thinner films (0.1–0.15 mm) were prepared by doctor-blading chitosan formulations onto glass microscope slides and curing, either at room temperature for several days or else in an oven at 50 °C for ~10 hours.

Laser graphitization. Electrodes were fabricated using a combination of a commercial CO_2 hobbyist laser system (10.6 μm wavelength, 30 W maximum power, HQ-3020B, GuangZhou Amonstar Trade Co. Ltd) and a mini-speed laser engraving machine (Colemeter DK-8 Pro-5 Square Haste Edition, 405 nm diode laser, 500 mW power). Electrodes designed in Microsoft PowerPoint were fabricated by raster scanning of the laser beam to create the electrode pattern on the cured chitosan biopolymer surface. Graphene-like carbon structures were fabricated by a three-step multi-wavelength process whereby an initial pre-conditioning of the chitosan film was obtained by raster scanning the CO_2 laser (2.1 W, 110 mm/s scan speed, Step 1), followed by direct-write graphitization within the preconditioned area with a 405 nm

laser (500 mW, dwell time 120 ms/pix, Step 2), followed by post-processing with CO_2 laser (2.1 W, 110 mm/s, Step 3).

Characterization. Laser-fabricated graphene-like carbon electrodes were morphologically characterized by a cold-cathode field-emission Scanning Electron Microscope (SEM, JSM- 7500F, JEOL UK Ltd.) operating at 5 kV acceleration voltage. ATR-FTIR analysis was carried out with a portable Bruker ALPHA II's Platinum ATR single reflection diamond ATR. Raman measurements were performed with a Renishaw inVia Confocal Raman mircoscope equipped with a 514 nm helium–neon laser. The laser beam was focused onto the sample through a Leica 20X objective with 0.4 N.A. Acquisition time was usually 10 s and measured power was 3 mW. X-ray photoelectron spectroscopy (XPS) measurements were carried out in an ultrahigh vacuum (UHV) chamber with a base pressure ~$5x10^{-10}$ mbar equipped with a SPECS LHS-10 hemispherical electron analyzer and a dual anode Al/Mg x-ray gun. All XPS measurements were acquired at room temperature using the un-monochromatized Mg Kα source in a Constant Analyzer Energy mode with pass energy of 10 eV, giving a full width at half maximum (FWHM) of 0.85 eV for the Ag $3d_{5/2}$ peak (recorded from a sputter-cleaned silver sample after linear background subtraction). Laser graphitized carbon flakes scraped off the chitosan surface were diluted in dimethylformamide (DMF), drop-cast on indium tin oxide (ITO)-coated glass substrates and dried under N_2 flow. The ITO was first treated with oxygen plasma in a medium vacuum chamber at P = 10^{-2} mbar O_2 and rf power 10.5 W in order to remove carbon contamination of the surface and to improve the coating homogeneity. The XPS core level spectra of C1s and N1s were analyzed using a fitting routine, where each spectrum was

decomposed into a series of individual mixed Gaussian-Lorentzian peaks following a Shirley background subtraction.

Current-voltage characterization. Two-terminal current-voltage measurements (± 1V, 10 mV step) were obtained under ambient conditions on mm-scale dumbbell structures using an Agilent E5270B parameter analyzer interfaced to a LakeShore Desert TTPX probe station.

Thermal degradation of materials was evaluated by *thermo-gravimetric analysis* (TGA) that was carried out in air flow (flow rate = 40 ml/min) using a TGAQ500-TA Instruments, at heating rate of 10°C/min in the temperature range from 35°C to 1000°C.

Bright field transmission electron microscopy (TEM) analysis was performed by means of a FEI Tecnai G12 Spirit Twin (LaB6 source) at 120 kV acceleration voltage. TEM images were collected on a FEI Eagle 4 k CCD camera.

X-ray diffraction was measured using a Panalytical X'Pert Pro diffractometer equipped with PixCel 1D detector (operative conditions: CuKα1/ Kα2 radiation, 40 kV, 40 mA, 2Θ range from 5° to 80°, step size 0.0131° 2Θ, counting time 40 s per step).

Electrochemical analysis. Cyclic voltammetry (CV) measurements were performed with a CHI760 bi-potentiostat electrochemical system using a Pt wire as counter electrode, Ag/AgCl as reference electrode and Laser-fabricated graphene-like carbon as working electrode. The three electrodes were assembled in a Teflon cell with a circular area of 8 mm diameter exposed to the electrolyte. The redox systems used were $[Ru(NH_3)_6]^{3+}$ (5 mM) in KCl (1M) and $[Fe(CN)_6]^{4-}$ (5 mM) in KCl (1 M). Electrolyte solutions were purged with N_2 for 30 min prior to measurements.

3.6 References

[1] H. Wahab, V. Jain, A. S. Tyrrell, M. A. Seas, L. Kotthoff, P. Johnson, *Carbon N. Y.* **2020**, *167*, 609.

[2] M. Dosi, I. Lau, Y. Zhuang, D. S. A. Simakov, M. W. Fowler, M. A. Pope, *ACS Appl. Mater. Interfaces* **2019**, *11*, 6166.

[3] A. F. Carvalho, A. J. S. Fernandes, C. Leitão, J. Deuermeier, A. C. Marques, R. Martins, E. Fortunato, F. M. Costa, *Adv. Funct. Mater.* **2018**, *28*, 1.

[4] J. Lin, Z. Peng, Y. Liu, F. Ruiz-Zepeda, R. Ye, E. L. G. Samuel, M. J. Yacaman, B. I. Yakobson, J. M. Tour, *Nat. Commun.* **2014**, *5*, 5.

[5] F. J. Romero, A. Salinas-Castillo, A. Rivadeneyra, A. Albrecht, A. Godoy, D. P. Morales, N. Rodriguez, *Nanomaterials* **2018**, *8*, 1.

[6] R. Srinivasan, B. Braren, R. W. Dreyfus, *J. Appl. Phys.* **1987**, *61*, 372.

[7] M. Burke, C. Larrigy, E. Vaughan, G. Paterakis, L. Sygellou, A. J. Quinn, G. Herzog, C. Galiotis, D. Iacopino, *ACS Omega* **2020**, *5*, 1540.

[8] D. X. Luong, K. Yang, J. Yoon, S. P. Singh, T. Wang, C. J. Arnusch, J. M. Tour, *ACS Nano* **2019**, *13*, 2579.

[9] F. Tehrani, M. Beltrán-Gastélum, K. Sheth, A. Karajic, L. Yin, R. Kumar, F. Soto, J. Kim, J. Wang, S. Barton, M. Mueller, J. Wang, *Adv. Mater. Technol.* **2019**, *1900162*, 1.

[10] T. Han, A. Nag, R. B. V. B. Simorangkir, N. Afsarimanesh, H. Liu, S. C. Mukhopadhyay, Y. Xu, M. Zhadobov, R. Sauleau, *Sensors (Switzerland)* **2019**, *19*, 13.

[11] R. Trusovas, K. Ratautas, G. Račiukaitis, G. Niaura, *Appl. Surf. Sci.* **2019**, *471*, 154.

[12] W. R. de Araujo, C. M. R. R. Frasson, W. A. Ameku, J. R. Silva, L. Angnes, T. R. L. C. L. C. Paixão, *Angew. Chemie* **2017**, *129*, 15113.

[13] S. Lee, S. Jeon, *ACS Sustain. Chem. Eng.* **2019**, *7*, 2270.

[14] S. Lee, J. Eun, S. Jeon, *Nano Energy* **2020**, *68*, 104364.

[15] Y. Li, D. X. Luong, J. Zhang, Y. R. Tarkunde, C. Kittrell, F. Sargunaraj, Y. Ji, C. J. Arnusch, J. M. Tour, *Adv. Mater.* **2017**, *29*, 1.

[16] R. Ye, Y. Chyan, J. Zhang, Y. Li, X. Han, C. Kittrell, J. M. Tour, *Adv. Mater.* **2017**, *29*, 1.

[17] X. Han, R. Ye, Y. Chyan, T. Wang, C. Zhang, L. Shi, T. Zhang, Y. Zhao, J. M. Tour, *ACS Appl. Nano Mater.* **2018**, *1*, 5053.

[18] T. S. D. Le, S. Park, J. An, P. S. Lee, Y. J. Kim, *Adv. Funct. Mater.* **2019**, *29*, 1.

[19] Y. Chyan, R. Ye, Y. Li, S. P. Singh, C. J. Arnusch, J. M. Tour, *ACS Nano* **2018**, *12*, 2176.

[20] S. Wang, Y. Yu, S. Luo, X. Cheng, G. Feng, Y. Zhang, Z. Wu, G. Compagnini, J. Pooran, A. Hu, *Appl. Phys. Lett.* **2019**, *115*.

[21] Z. Zhang, M. Song, J. Hao, K. Wu, C. Li, C. Hu, *Carbon N. Y.* **2018**, *127*, 287.

[22] M. Rinaudo, *Prog. Polym. Sci.* **2006**, *31*, 603.

[23] H. Yoon, J. Nah, H. Kim, S. Ko, M. Sharifuzzaman, S. C. Barman, X. Xuan, J. Kim, J. Y. Park, *Sensors Actuators, B Chem.* **2020**, *311*, 127866.

[24] F. Croisier, C. Jérôme, *Eur. Polym. J.* **2013**, *49*, 780.

[25] L. H. Chen, T. Li, C. C. Chan, R. Menon, P. Balamurali, M. Shaillender, B. Neu, X. M. Ang, P. Zu, W. C. Wong, K. C. Leong, *Sensors Actuators, B Chem.* **2012**, *169*, 167.

[26] W. Wu, J. Shen, P. Banerjee, S. Zhou, *Biomaterials* **2010**, *31*, 8371.

[27] H. Wang, J. Qian, F. Ding, *J. Agric. Food Chem.* **2018**, *66*, 395.

[28] M. Aider, *LWT - Food Sci. Technol.* **2010**, *43*, 837.

[29] Y. H. Lin, P. L. Kang, W. Xin, C. S. Yen, L. C. Hwang, C. J. Chen, J. T. Liu, S. J. Chang, *Comput. Ind.* **2018**, *100*, 1.

[30] A. C. Ferrari, J. Robertson, *Phys. Rev. B - Condens. Matter Mater. Phys.* **2000**, *61*.

[31] P. Lespade, R. Al-Jishi, M. S. Dresselhaus, *Carbon N. Y.* **1982**, *20*, 427.

[32] A. Sadezky, H. Muckenhuber, H. Grothe, R. Niessner, U. Pöschl, *Carbon N. Y.* **2005**, *43*, 1731.

[33] A. C. Ferrari, D. M. Basko, *Nat. Nanotechnol.* **2013**, *8*, 235.

[34] R. J. Nemanich, J. T. Glass, G. Lucovsky, R. E. Shroder, *J. Vac. Sci. Technol. A Vacuum, Surfaces, Film.* **1988**, *6*, 1783.

[35] A. Eckmann, A. Felten, A. Mishchenko, L. Britnell, R. Krupke, K. S. Novoselov, C. Casiraghi, *Nano Lett.* **2012**, *12*, 3925.

[36] M. A. Pimenta, G. Dresselhaus, M. S. Dresselhaus, L. G. Cançado, A. Jorio, R. Saito, *Phys. Chem. Chem. Phys.* **2007**, *9*, 1276.

[37] D. R. Lenski, M. S. Fuhrer, *J. Appl. Phys.* **2011**, *110*.

[38] S. S. Silva, S. M. Luna, M. E. Gomes, J. Benesch, I. Pashkuleva, J. F. Mano, R. L. Reis, *Macromol. Biosci.* **2008**, *8*, 568.

[39] G. M. Liao, C. C. Yang, C. C. Hu, Y. L. Pai, S. J. Lue, *J. Memb. Sci.* **2015**, *485*, 17.

[40] M. Grossutti, J. R. Dutcher, *Biomacromolecules* **2016**, *17*, 1198.

[41] G. Lawrie, I. Keen, B. Drew, A. Chandler-Temple, L. Rintoul, P. Fredericks, L. Grøndahl, *Biomacromolecules* **2007**, *8*, 2533.

[42] G. C. Ritthidej, T. Phaechamud, T. Koizumi, *Int. J. Pharm.* **2002**, *232*, 11.

[43] C. Qiao, X. Ma, J. Zhang, J. Yao, *Carbohydr. Polym.* **2019**, *206*, 602.

[44] M. Al Kobaisi, P. Murugaraj, D. E. Mainwaring, *J. Polym. Sci. Part B Polym. Phys.* **2012**, *50*, 403.

[45] H. Hatakeyama, T. Hatakeyama, *Thermochim. Acta* **1998**, *308*, 3.

[46] R. Murray, M. Burke, D. Iacopino, A. J. Quinn, *ACS Omega* **2021**, *6*, 16736.

[47] E. Vaughan, C. Larrigy, M. Burke, L. Sygellou, A. J. Quinn, C. Galiotis, D. Iacopino, *ACS Appl. Electron. Mater.* **2020**, *2*, 3279.

[48] N. Elgrishi, K. J. Rountree, B. D. McCarthy, E. S. Rountree, T. T. Eisenhart, J. L. Dempsey, *J. Chem. Educ.* **2018**, *95*, 197.

[49] E. Vaněčková, M. Bouša, Š. Nováková Lachmanová, J. Rathouský, M. Gál, T. Sebechlebská, V. Kolivoška, *J. Electroanal. Chem.* **2020**, *857*.

[50] E. Szymańska, K. Winnicka, *Mar. Drugs* **2015**, *13*, 1819.

Supporting Information

Porous 3D graphene-like carbon from sustainable materials: laser graphitization of chitosan

*Cathal Larrigy[§], Micheal Burke[§], Alessandra Imbrogno, Eoghan Vaughan, Labrini Sygellou,[b] George Paterakis,[b] Costas Galiotis,[c] Daniela Iacopino, and Aidan J. Quinn**

Dr. M. Burke, C. Larrigy, Dr. A. Imbrogno, E. Vaughan, Dr. D. Iacopino, Dr. A. J. Quinn

Tyndall National Institute, University College Cork, Lee Maltings, Dyke Parade, Cork T12 R5CP, Ireland.

Dr. G. Paterakis, Dr. L. Sygellou, Institute of Chemical Engineering Sciences, Foundation for Research and Technology-Hellas (FORTH/ICE-HT), Patras 265 04, Greece

Dr. C. Galiotis, Department of Chemical Engineering, University of Patras, Patras 26504, Greece

(a)

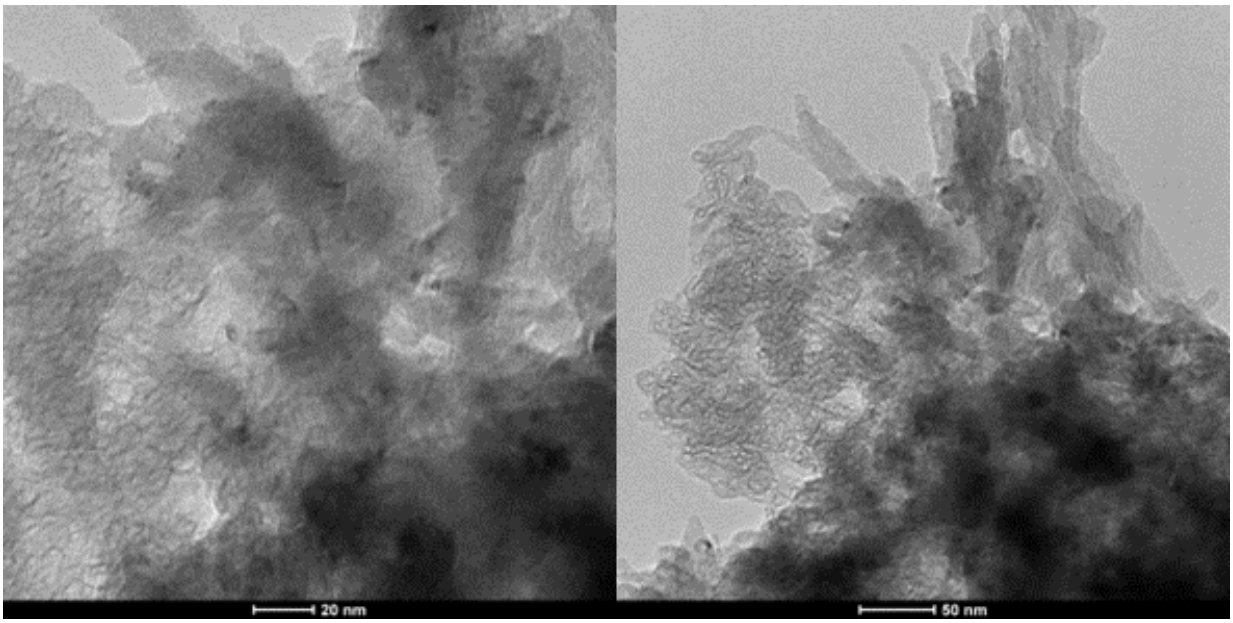


Figure S3.1. Transmission electron microscopy of 2-step chitosan-based laser-induced graphene material.

A) B)



C)

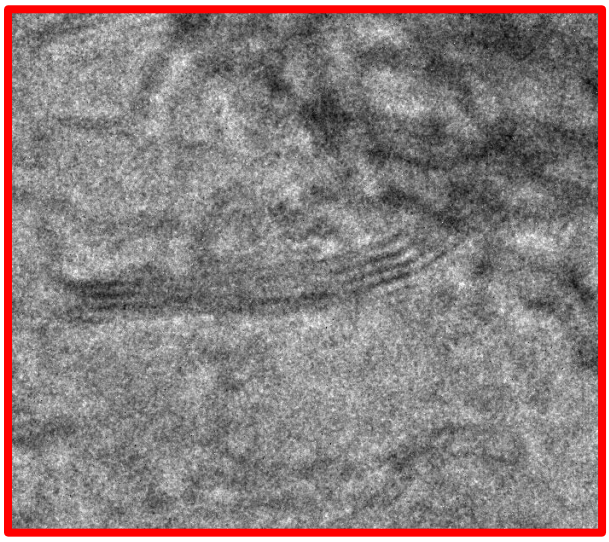


Figure S3.2. (A-C) Transmission electron microscopy of 3-step chitosan-based laser-induced graphene material. Highlighted area (C) shows a wrinkle structure, with layering, indicative of graphitic structure.

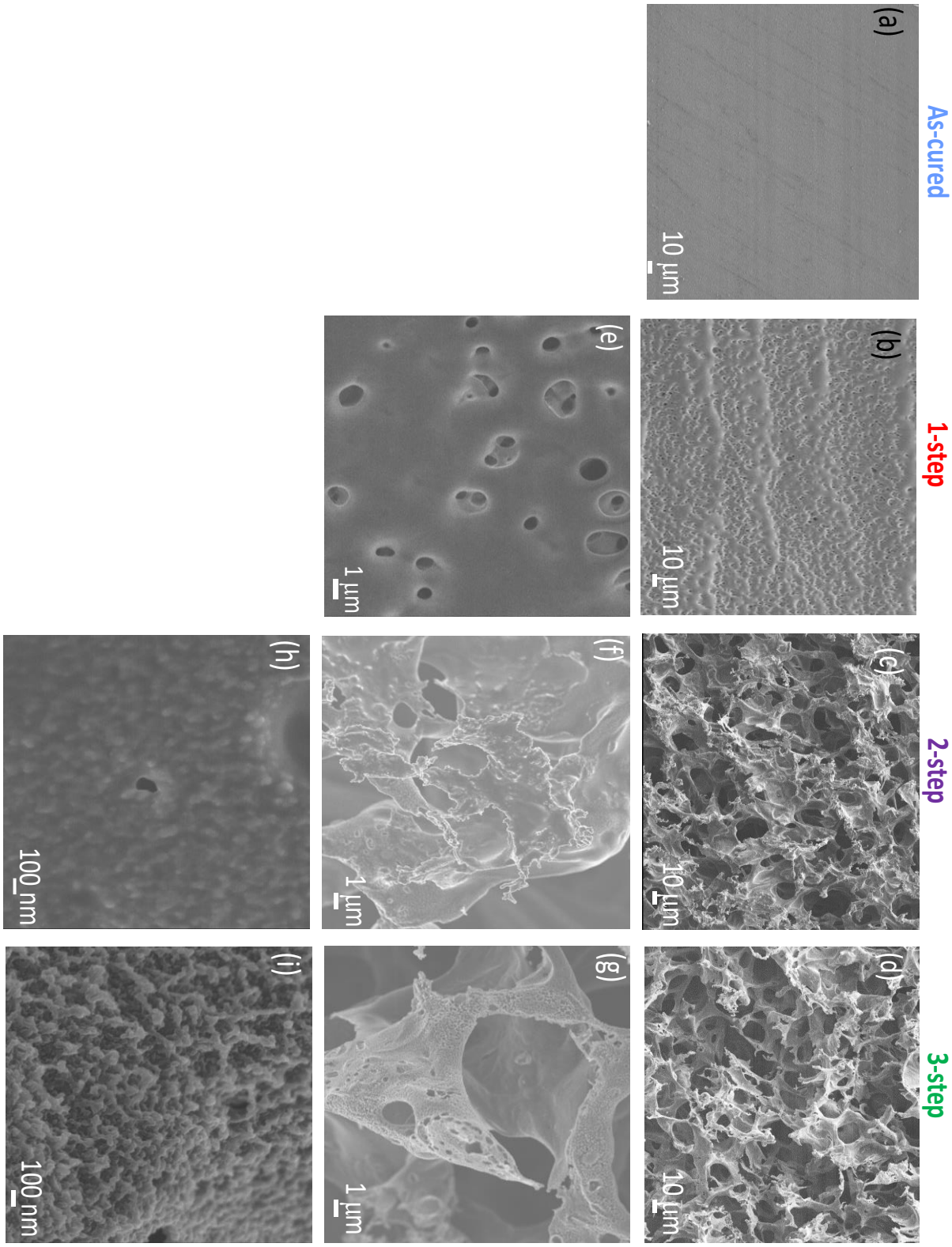
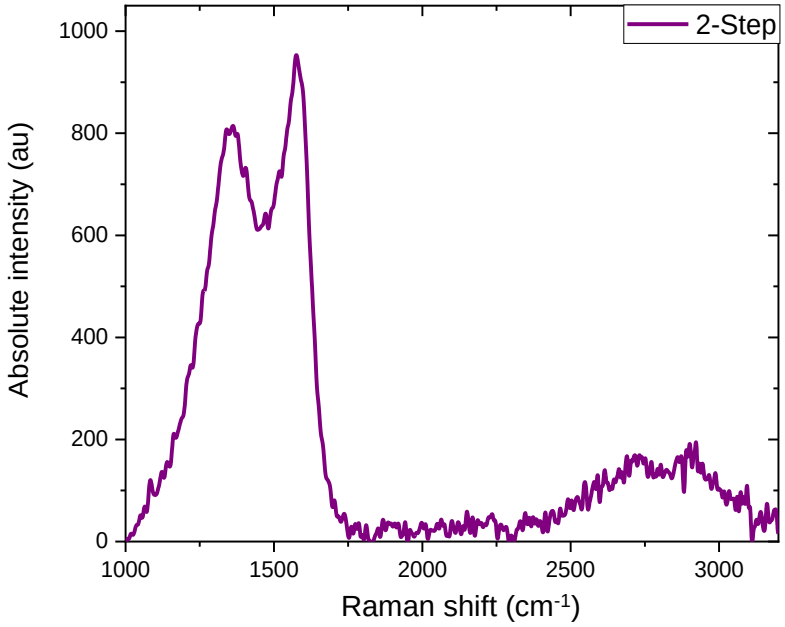


Figure S3.3. SEM image collage showing changes in surface morphology at different stages of the 3-step chitosan laser-fabricated graphene-like carbon process.

A)



B)

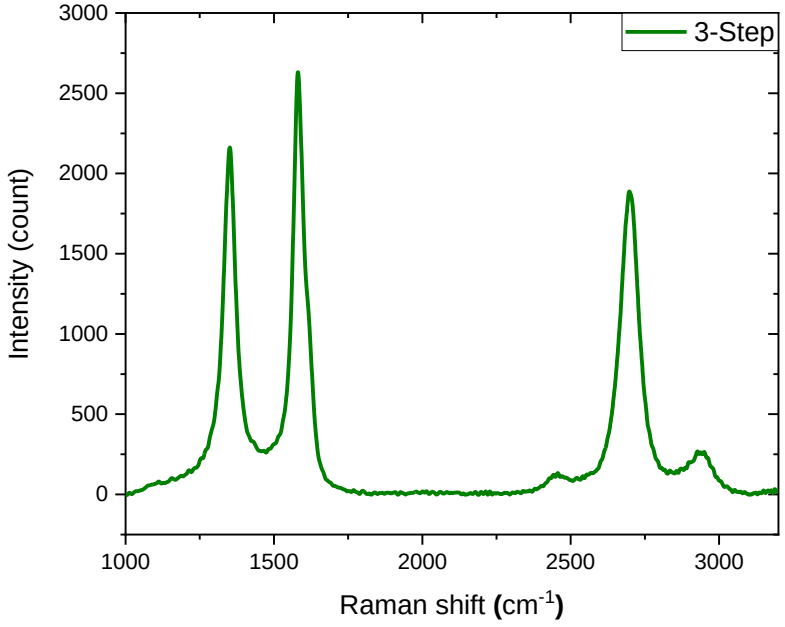
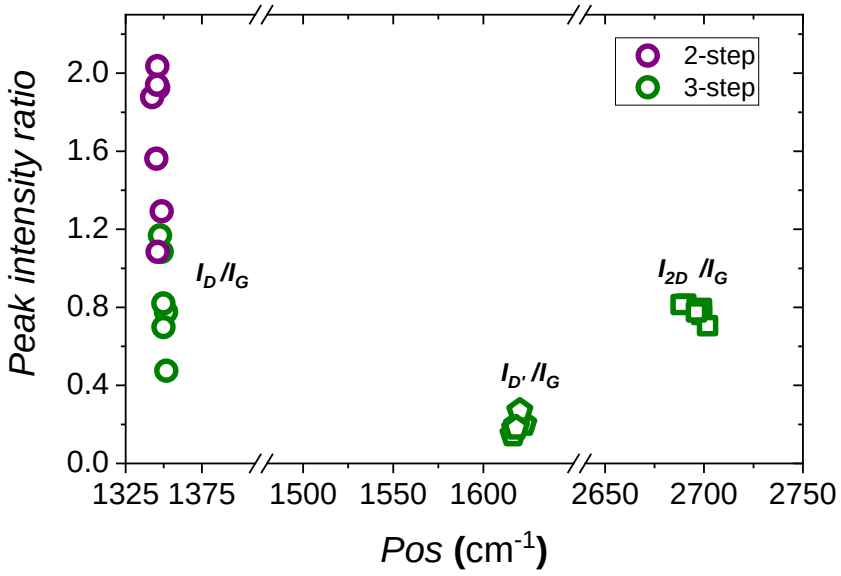


Figure S3.4. Full Raman spectroscopy of (a) 2-step and (b) 3-step processed material.

(a)



(b)

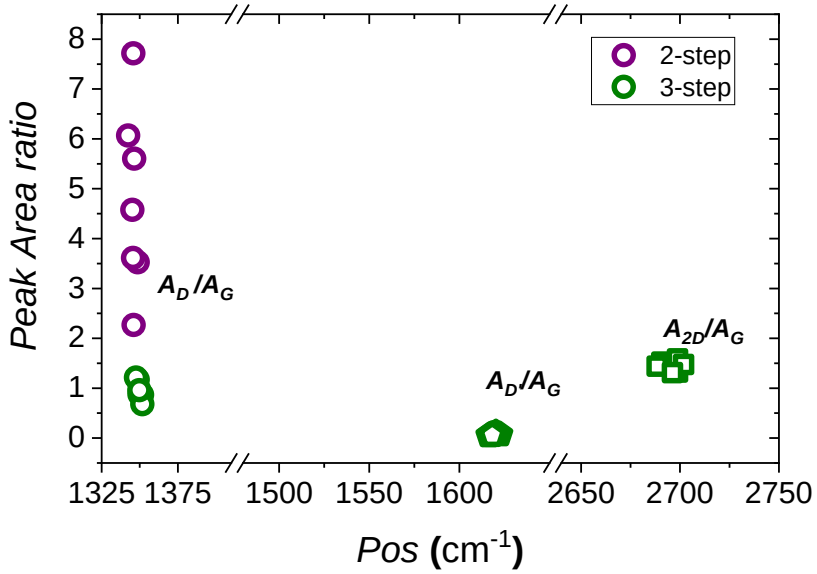


Figure S3.5. Maps of Raman fit results for (a) peak intensity ratios of the *D*, *D´*and 2*D* peaks, each normalised to the intensity of the *G* peak for both 2-step and 3-step processed chitosan. (b) Corresponding area ratios.

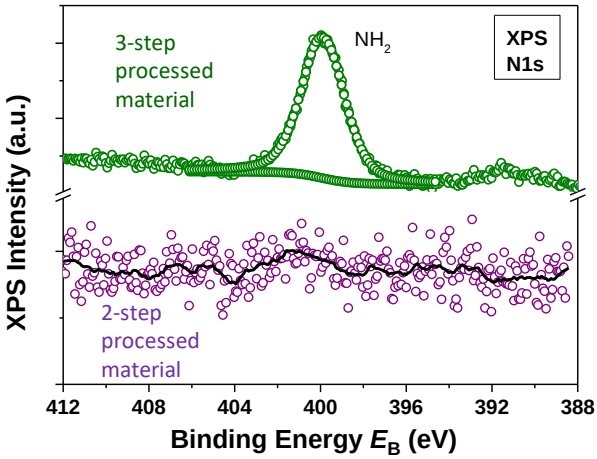


Figure S3.6. Nitrogen 1s XPS spectra for 2-step processed material (bottom) and 3-step processed material (top).

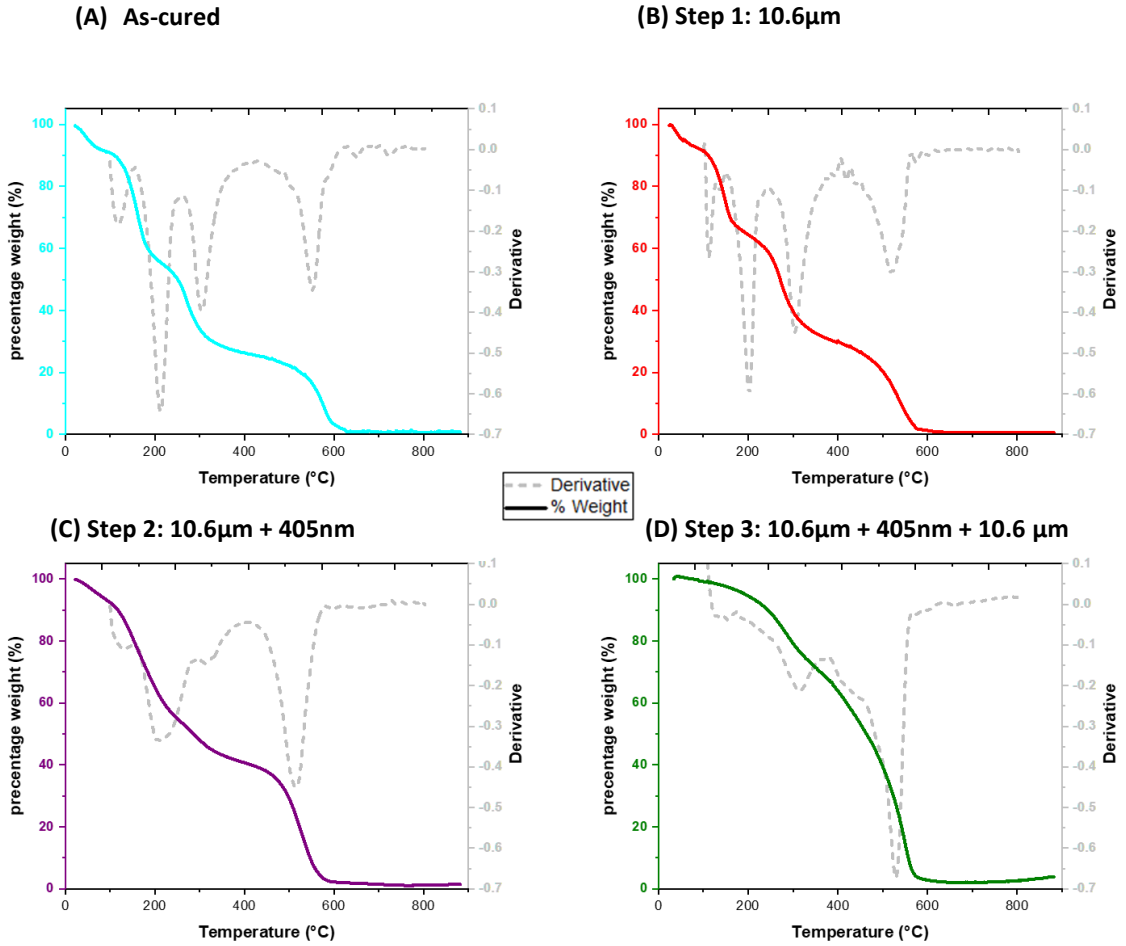


Figure S3.7. Single Thermogravimetric analysis (TGA) measurements conducted in air, (solid) with corrosponding derivative weight (Dashed), of various stages of Chitosan LIG prodction; a) as cured (light blue) , b) 1-step processed (red) , c) 2-step processed (purple) and d) 3-step processed (green).

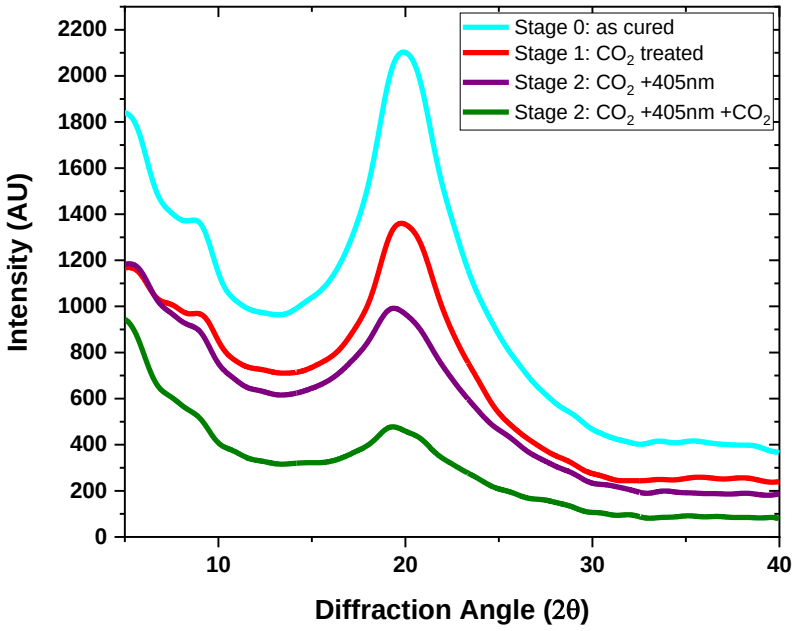


Figure S3.8. X-Ray diffraction measurements of various stages of chitosan LIG fabrication; as cured (light blue), 1-step processed (red), 2-step processed (purple) and 3-step processed (green).

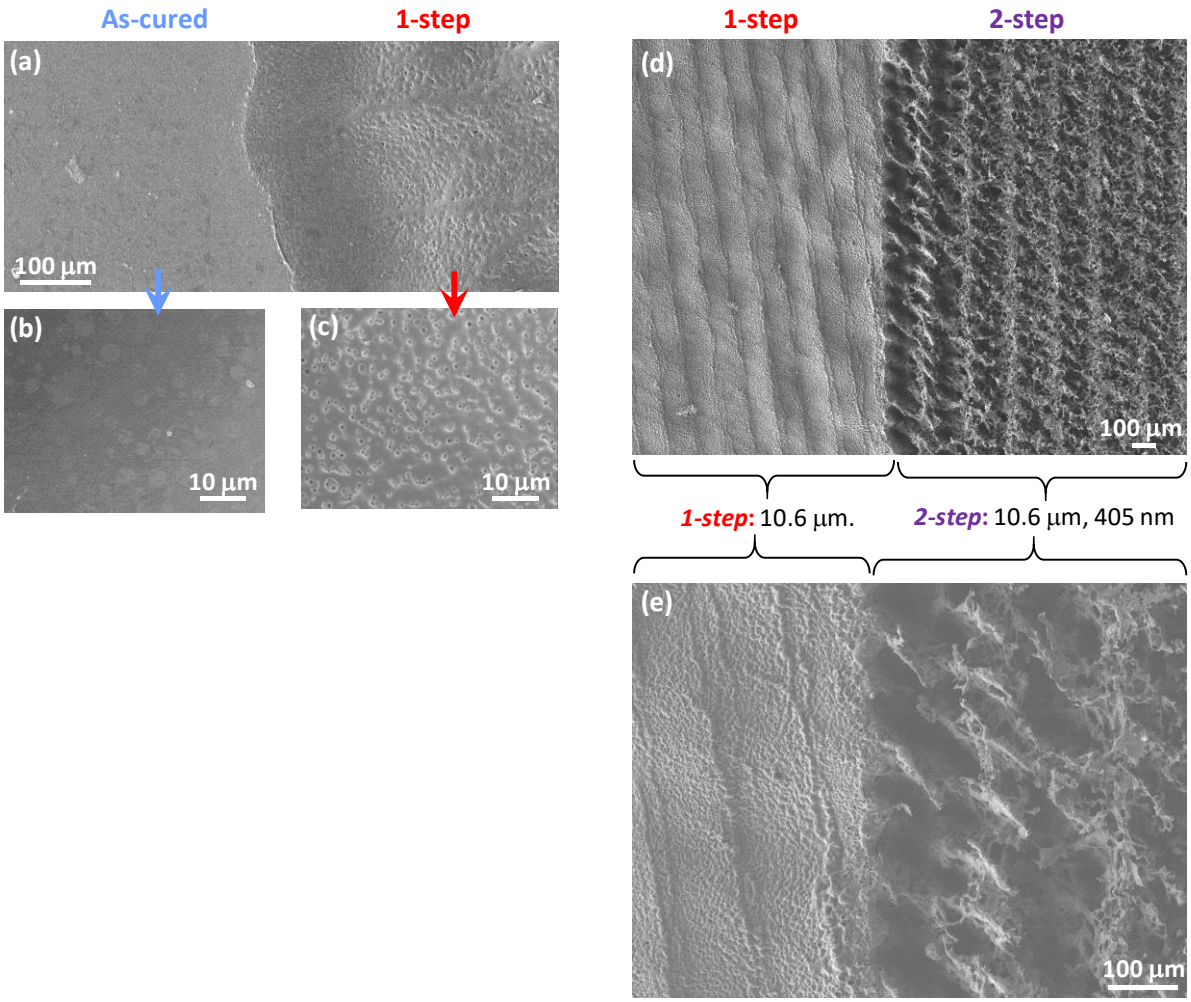


Figure S3.9. (a-c) Scanning Electron Micrographs (SEMs) of a laser-processed chitosan bioplastic film acquired at boundary between an as-cured region (left) and a 1-step processed region (right). (d,e) SEMs acquired at the boundary between a 1-step processed region (left) and a 2-step processed region (right). 1-step process: 10.6 µm CO_2 laser, ~2.8 W power, 110 mm/sec write speed. 2-step process: 1-step process followed by irradiation with 405 nm laser, 0.5 W power, 120 ms/pixel dwell time.

Electrical test structures from drop-cast chitosan films. Millimetre-scale dumbbell laser-fabricated graphene-like carbon electrical test structures were also fabricated using both two-step and three-step processing by raster-scanning over a rectangular region of a cured chitosan film using the CO_2 laser (1st step), raster-writing the dumbbell structure using the 405 nm laser (2nd step) and raster-scanning over a rectangular region containing the dumbbell structure using the CO2 laser (3rd step). Comparing SEM images of the same structure acquired after the 2nd step (**Figure S3.10a**) and the 3rd step (**Figure S3.10b**) shows that the width of the central bar remains roughly the same (~550 µm), while the length is reduced from ~1050 µm to ~800 µm. Measured current-voltage (*I*-*V*) data show a linear response from -1 V to 1 V for both the 2-step and 3-step devices with corresponding resistance values ~5.2 kΩ (2-step) and 1.7 kΩ (3-step).

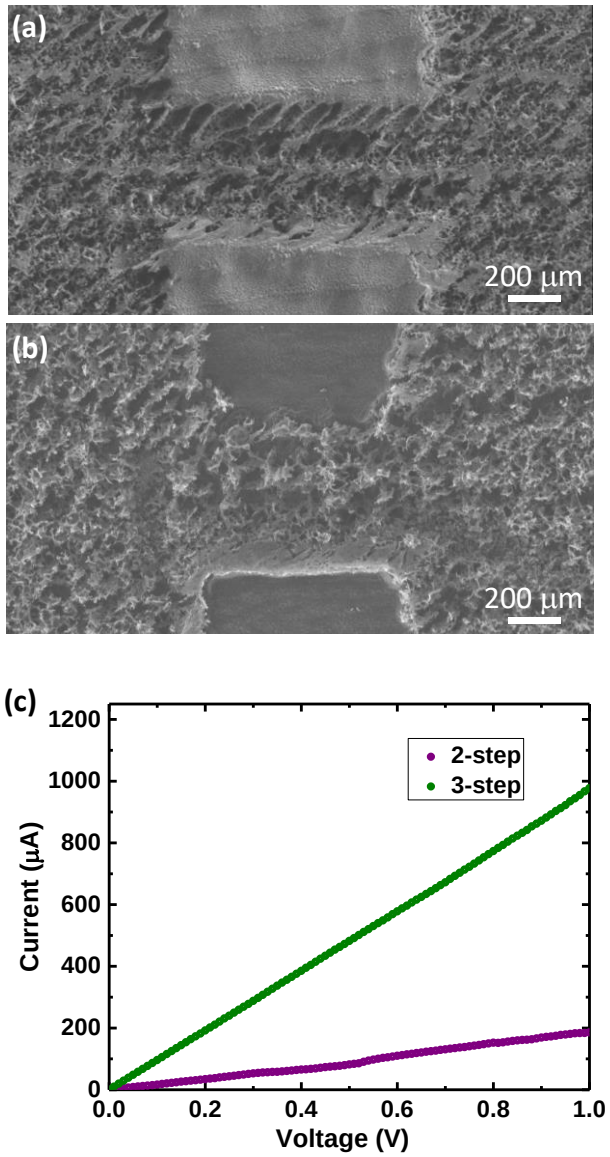


Figure S3.10. (a,b) SEM images showing: A 2-step patterned "H" structure (a); the same region following the 3rd step (exposure of the entire region using a CO_2 laser) (b). (c) 0-1 V segment of current-voltage (*I*-*V*) data acquired for the 2-step patterned device shown in (a) and for the same device following the 3rd step.

Electrical test structures from doctor-bladed chitosan films.

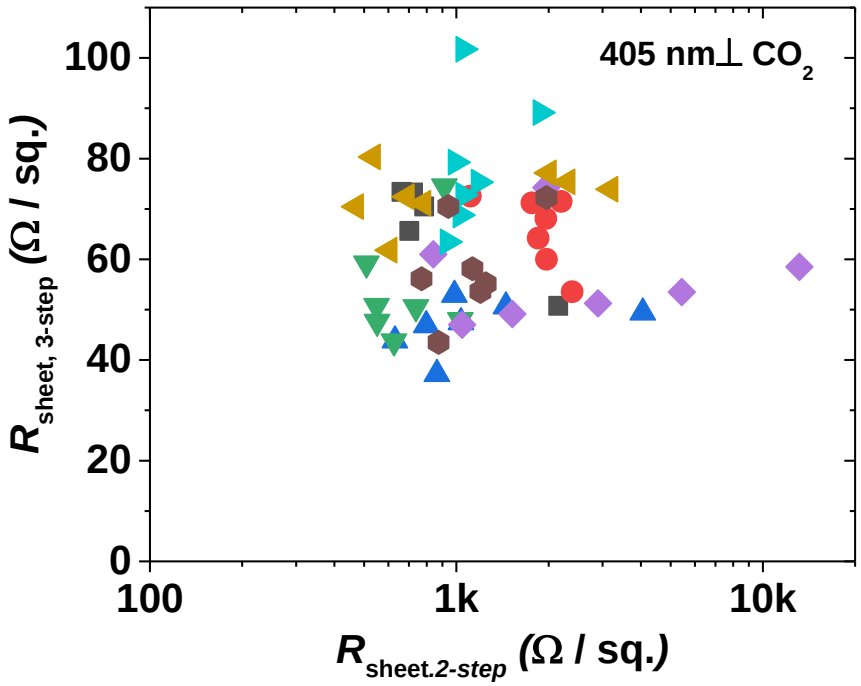


Figure S3.11. Electrical conductivity test of doctor-bladed Chitosan-based Laser-induced graphene structures, (for 54 of the 57 devices which were under 20 kΩ/sq.) displaying the change in the sheet resistance between 2-step (x-axis) and 3-step process (y-axis).

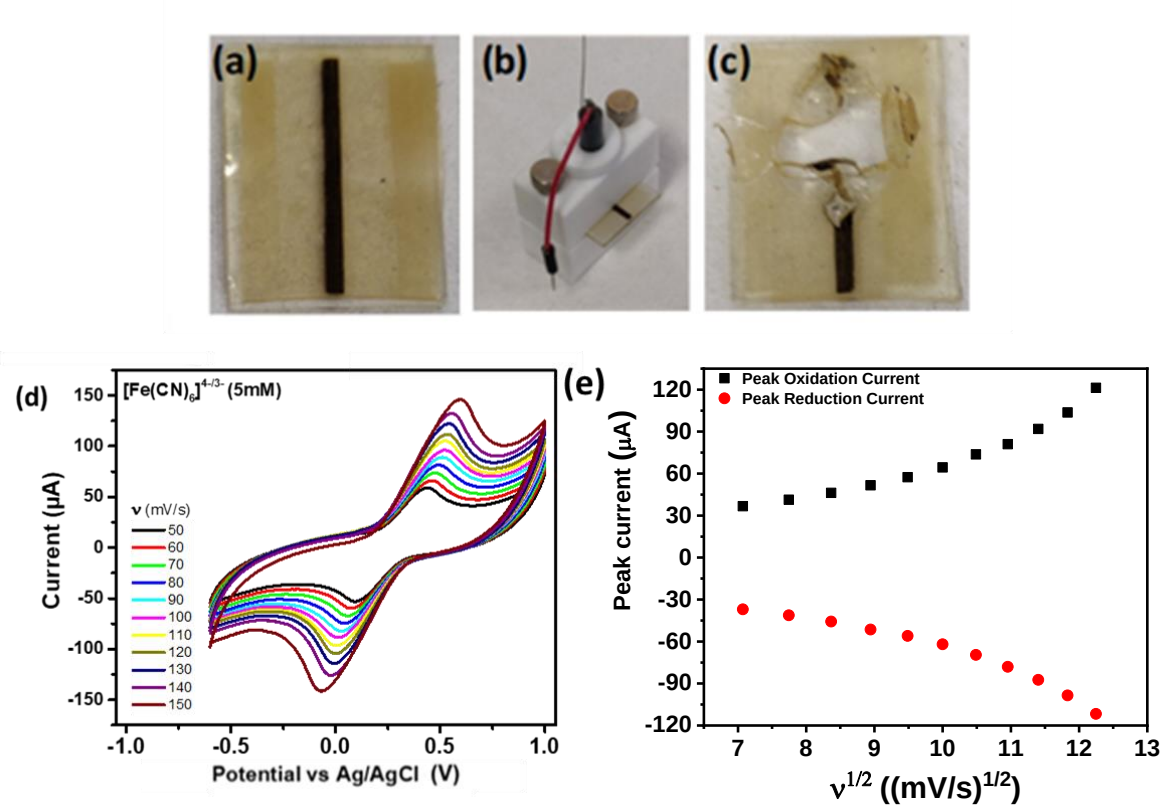


Figure S3.12. Proof of concept demonstration of transient electrochemical sensing using 3-step laser fabricated graphene-like carbon electrodes from a drop-cast chitosan biopolymer. Photos of: an as-prepared single working electrode (a); the 3-electrode electrochemical cell (b); the working electrode following ~20 minutes electrochemical cycling **(d)** cyclic voltammograms from the working electrode in a 5 mM solution of $Fe(CN)_6^{3-/4-}$ in 1 M KCl. **(e)** Peak oxidation and reduction values vs square root of potential scan rate, for cyclic voltammograms of 1 mM $Fe(CN)_6^{3-/4-}$ in 1 M KCl.

Chapter 4: VOC, solvent and humidity sensors from sustainable Chitosan- based Laser-induced graphitic carbon materials

Aimed for publication in:

Advanced functional materials

Author list:

Cathal Larrigy, Richard Murray, Michael Nolan, Arbresha Muriqi, and Aidan J. Quinn.

4.1 Abstract

Chitosan-based laser-induced graphene shows great promise as a potential method for device fabrication with a low environmental footprint across its entire life cycle. One potential application is in the development of environmentally friendly humidity and gas sensing devices. Chitosan's attractive properties (in particular; biodegradability; predictable degradation rate; structural integrity and non-toxicity to cells) make for an interesting prospect for green packaging. Adding a sensing element via a low-cost and low carbon footprint method such as laser-induced graphene fabrication provides an ideal scenario for a potential candidate for green intelligent packaging.

To demonstrate, chitosan-based laser-induced graphene 2-terminal impedance style sensors were fabricated and tested against various controlled humidities; first via standard aqueous salt solutions, then via humidity-controlled nitrogen gas flow. It was noted that level of humidity influenced the resistance of the sensor, increasing humidity resulting in decreasing resistance.

The chitosan-based laser-induced graphene 2-terminal impedance style sensors were also exposed to various solvent vapours, to test for sensitivity. It was noted that molecules which could create hydrogen bonds and were polar decreased the resistance of the sensor, whereas those with were non-polar and had no hydrogen capability did not have a great effect on the resistance.

4.2 Introduction

Laser-induced graphene-like materials have been a potential target for integration into physical, chemical, and biological sensors. However, the bulk of the research towards LIG based materials has focused on utilizing polyimide as a target substrate[1]. Lately, due to pressing issues surrounding environmental conservation, alternative laser graphitization routes have been explored, chiefly those that come from a sustainable, renewable, and more environmentally friendly approach[2–4]. One such example is chitosan-based laser-induced graphene. Chitosan, a copolymer of β[1,4]-linked 2-acetamido-2-deoxy-D-glucopyranose and 2-amino-2-deoxy-D-glucopyranose, obtained by chemical or enzymatic deacetylation of chitin, is one of the most abundant natural polymers on earth[5]. Chitosan's attractive properties include high porosity; biodegradability; predictable degradation rate; structural integrity and non-toxicity to cells[6,7]. Currently, chitosan has been used in a variety of applications such as sensing applications[8], food packaging[9], and medical devices [10]. Chitosan-based laser-induced graphene (CLIG) provides a potential avenue for a sustainable sensing platform, which would be of particular interest to packaging methods. This work highlights the possibilities of using CLIG as a method of determining changes in humidity, or the presence of certain volatile organic compounds.

Traditional packaging has typically four key aspects; protection, containment, communication, and convenience[11]. Lately however, a need for more advanced packaging has been highly sought after, namely intelligent packaging[12]. Current packaging has many aspects of intelligent packaging (examples range from simple barcodes to more complex RFID tags), however these aspects are often either not cost-effective or deliver minimal information. Current efforts in intelligent packaging look to both reducing packaging fabrication costs, and/or increasing the quality and quantity of information that can be gathered[12]. This includes incorporating smart packaging in the form of such sensors as time-temperature indicators,

biosensors, and of course gas and humidity indicators. By utilizing smart packaging, item shelf life, and viability can be assessed remotely. For example, foodstuffs that require a certain humidity to improve shelf life, or foodstuff that can produce certain gas compositions as they deteriorate can be detected and measured in real time[13–15].

There are two variations of humidity sensing: Relative humidity sensors measure the amount of water vapour present in the air, relative to the saturation concentration at that temperature. Absolute humidity represents the ratio of mass of water vapour to the mass of dry air. The majority of humidity sensors tend to be relative humidity sensors[16]. Of these, there are three distinct types:

- Ceramic, which depend on adsorbed water on their surface to protonically conduct electricity[17].
- Semiconductor, which depend on water adsorption to reduce (in the case of p-type) or increase (in the case of p-type) conduction through the material[18].
- Polymer, which use water adsorption to either increase or decrease overall conductance or alter the dielectric constant of the polymer[19].

While the distinct advantage of having many measurement paths is of great benefit, a common flaw between all of the above sensors is the lack of sustainable, or environmentally friendly variants. Many require materials which are not widely recyclable, or compostable, and often require steps in fabrication which are energy and resource intensive. Similarly for sensing of solvents and Volatile Organic Compounds (VOCs), little consideration is given in terms of the environmental footprints associated with fabrication and materials used. Development of sustainable sensors, therefore, could lead to a reduction in the carbon footprint of the fabrication, as well as the materials used.

This work aims to provide such an alternative. Laser-induced graphene provides an additive fabrication technique which is resource and energy efficient, and can produce porous 3D graphitic structures, from which electrodes and sensing devices can be designed. Combining this with a sustainable and natural feedstock material, in the form of chitosan, as a precursor, laser-induced graphene can be fabricated on a biodegradable material, which has a predictable degradation rate, structural integrity and is non-toxic to cells. By utilizing a 2-terminal impedance style device fabricated via chitosan-based laser-induced graphene methods, an environmentally friendly device capable of detecting variations in relative humidity and detect the presence of certain VOCs is demonstrated here.

4.3 Results and Discussion

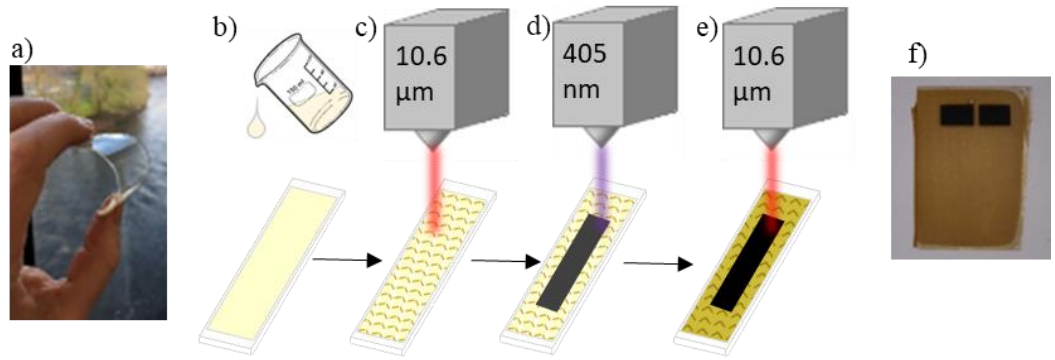


Figure 4.1. Chitosan-based Laser-induced graphene fabrication process flow for 2-terminal impedance style sensors. a) example of as cured chitosan film, b-e) Chitosan LIG fabrication process b) chitosan film deposited and cured to glass slides, c) Step 1: pre-treatment of chitosan film with 10.6µm CO_2 laser; d) step 2: direct write graphitization of required pattern using 405nm laser; e) step 3: post-processing step with 10.6µm CO_2 laser. f) example of chitosan-based laser-induced graphene fabricated 2-terminal impedance style sensor with 0.8 mm interelectrode gap.

The 2-terminal impedance sensors were fabricated on chitosan-based laser-induced graphene, the process steps of which can be seen in figure 4.1. As the chitosan film cannot be converted directly into LIG, the material requires a multi-stage lasing process, as described in chapter 3. Briefly, an aqueous chitosan bioplastic formulation was doctor-bladed onto glass slides for mechanical support and ease of transport (figure 4.1b). Following curing, the chitosan bioplastic was exposed to one pass of a CO_2 laser, which dehydrates the surface layer (figure 4.1c) and increases the porosity (see Chapter 3). The target electrode design is then written using a visible 405 nm laser (figure 4.1d). Finally, another pass of the CO_2 laser converts the carbonised material into a graphitized structure (figure 4.1e). Figure 4.1f shows a photo of a typical device.

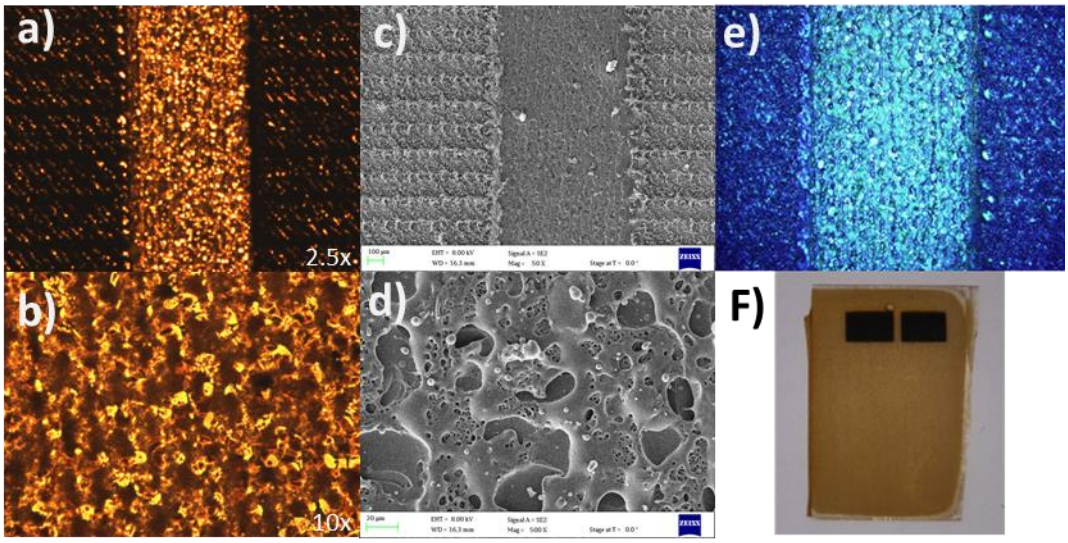


Figure 4.2. Imagery of 2-terminal chitosan-based LIG impedance style sensors. a-b) microscope images of centre gap region. c-d) Scanning electron microscopy of centre gap region. e) Fluorescent microscopy images of centre gap region. f) macro photo of sensor

The 2-teminal style sensors consist of two laser-induced graphene tracks with an aspect ratio of 1:1.6, on a chitosan-based bioplastic substrate which can be seen in Figure 4.2 f). The LIG tracks are arranged as such that there is a gap between the two of ~800µm. This distance is confirmed by scanning electron microscopy images. Scanning electron microscopy (figure 4.2c, d) shows the variation in the LIG and gap sections of CLIG sensor. The LIG regions, which were exposed to all three-laser fabrication stages, shows a micro/nanoporous morphology consistent with previous laser-induced graphene formations. The gap region, which did not undergo a carbonization step in fabrication shows a porous structure due to exposure to both CO_2 lasing steps as a result of the surface layers of the material dehydrating. Additionally, possibly due to both the proximity of the carbonised regions and due to the path of the 2-step lasing process (passing over the gap region), some minor carbon occlusions can be observed. This is evident in both the high magnification scanning electron micrographs, as well as the fluorescence micrographs. Away from the gap region on the chitosan bioplastic,

which was exposed to both CO_2 lasing steps, these carbon occlusions are not observed. It is likely for impedance style measurements, these occlusions aid responses from target analytes, by providing additional leakage paths for electrons between the two carbon electrodes.

Humidity detection

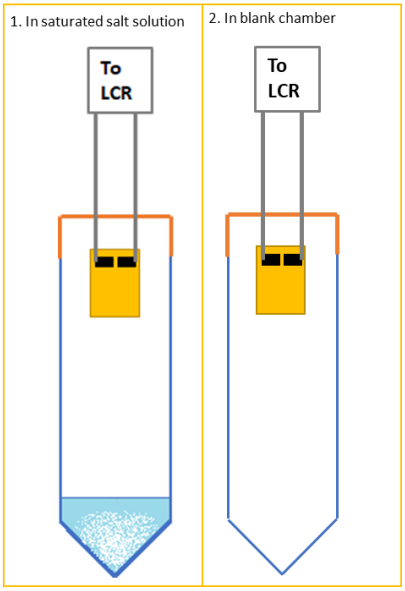


Figure 4.3. Humidity detection scheme for chitosan-based laser-induced graphene fabricated 2-terminal impedance style sensors when exposed to aqueous saturated salt solutions.

CLIG based humidity detection was completed by exposing the fabricated devices to aqueous saturated salt solutions, with known relative humidity concentrations at room temperature[20]. The CLIG device was connected into Agilent E53708B LCR Meter. The measuring voltage was set to 100mV AC, with a frequency of 1kHz. The capacitance and resistance of the devices were all measured in parallel. Prior to measurement of the aqueous saturated salt solutions relative humidity, the initial resistance and capacitance of each device was recorded in the open (Relative room humidity ~63%, room temperature ~20ºC). CLIG device was first placed in a sealed vessel with the required aqueous saturated salt solution. Resistance and capacitance of

the device was recorded over a 1-hour period, with at known time intervals. Following exposure, the device was placed in an empty vessel, and the recovery period was recorded in a similar method. This gave both a response and recovery curve for required humidity.

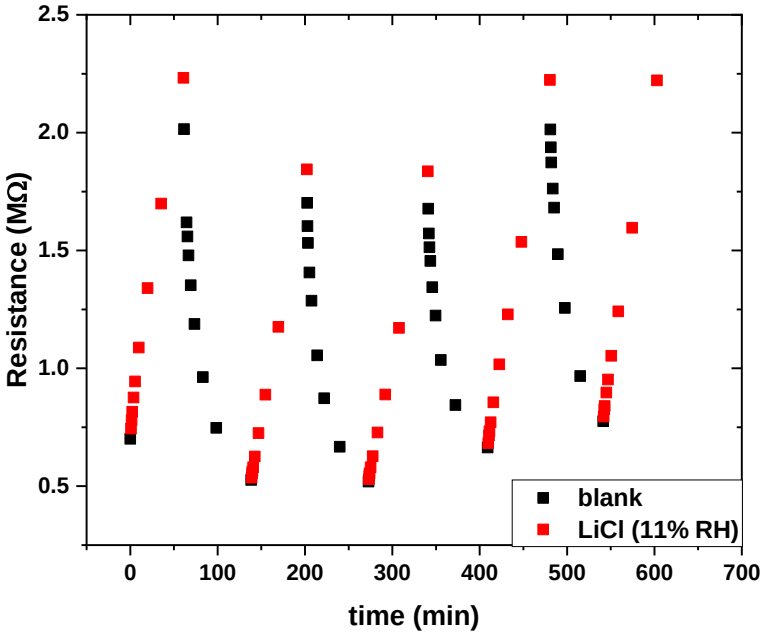


Figure 4.4 Repeated resistance measurements from 2-terminal CLIG impedance sensors exposed to consistent humidity from an aqueous saturated salt solution of lithium chloride (11% RH).

To show the device stability over multiple measurements, the CLIG devices was first exposed to a repeated series of the same aqueous saturated salt solution. For this purpose, Lithium chloride was used, with a relative humidity of 11% at room temperature. The results of one device can be seen in figure 4.4, showing repeating experiment of exposure to saturated Lithium chloride aqueous salt solutions, with recovery periods between each exposure in room humidity conditions. Despite mild fluctuations in response magnitudes, the overall shape of exposure and recovery curves, similarities between all measurements can be observed, showing stability of electrode after repeated testing. The variability in the response can be accounted for

by the varying room humidity, and indeed the chitosan bioplastic itself undergoing mild changes after repeated exposure.

Notably once the device goes from a high humidity (i.e., in the open or blank vessel (~60% RH)) to a lower humidity (in the lithium chloride containing vessel (~11% RH)) a change in the devices capacitance and resistance can be observed. While in the lower humidity the resistance increases (figure 4.4), and the capacitance decreases (figure S4.1). As the CLIG devices, and non-graphitized material contains a considerable amount of water (likely >30% see Chapter 3), exposing the device to a low relative humidity environment is expected to further dehydrate the surface chitosan, including the gap region between the electrodes. Once the device is moved to the ambient recovery vessel, and exposed to a higher humidity, the resistance and capacitance returns to previous levels, likely due to readsorption of water molecules.

A possible reason for this change in conductivity can be a result of a Grotthuss mechanism. Unaltered chitosan molecules contain several hydroxyl and amine groups. Water molecules can bond to these groups via hydrogen bonding, which allows chitosan to reversibly adsorb water molecules. Grotthuss mechanism have been proposed to explain protonic conduction – one example is proton hopping of a H^+ ion via switching of hydrogen and covalent bonds[21,22]. This occurs along "proton wires", an example of which can be networks of water molecules connected via hydrogen bonds.[23]. In addition, as the chitosan here is previously treated with acetic acid, the anime groups in this formulation are protonated. The polarity of water molecules reduces the ionic interactions between amine groups and protons. This promotes deprotonation of protonated amine groups. This then increases the density of mobile protons, increasing protonic conduction. Changing humidity from the blank vessel at room humidity, to the low humidity saturated salt solution, results in a lower surface concentration of water

molecules present, reducing the effective number of protonic conduction channels between the electrodes. This presents as an increase in the device resistance.

CLIG based humidity sensors were also exposed to a series of aqueous saturated salt solutions, as shown in figure 4.3, each with an increasing relative humidity at room temperature: lithium chloride (11% RH), magnesium chloride (33% RH), potassium carbonate (43% RH), copper chloride (67% RH), sodium chloride (78% RH), and potassium chloride (85% RH)[20]. These standards were each contained within a sealed modified 50mL centrifuge tube, with ample head space. The CLIG sensor was placed inside the corresponding chamber for 1 hour at a time, with 1-hour recovery periods in a "blank" chamber (ambient environment). Device capacitance and resistance values (1 kHz excitation) were recorded at regular intervals.

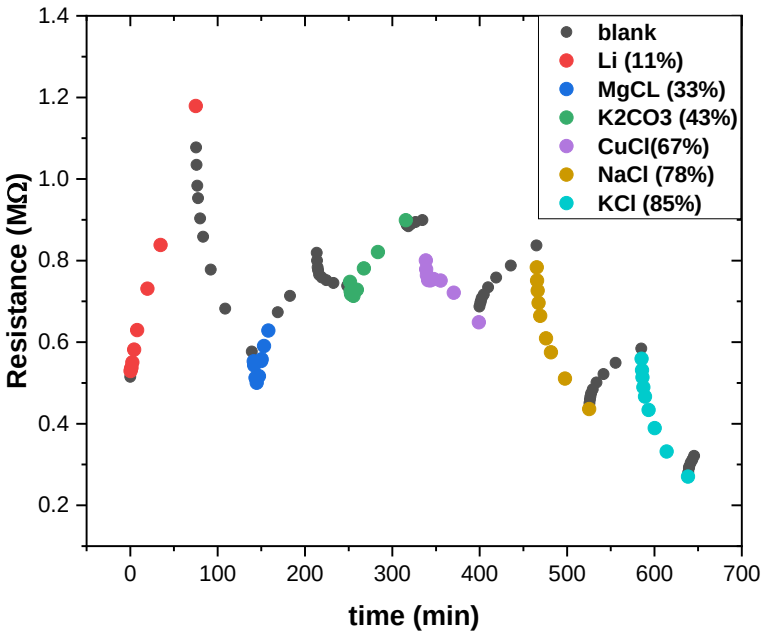


Figure 4.5 Resistance measurements, from 2-terminal impedance Chitosan based-LIG sensor measurements when exposed to a series of aqueous saturated salt solutions.

Figure 4.5 shows the change in resistance of a sensor in one trial. Focusing on the capacitance, a change in magnitude can be observed as the sensor passes into differing humidity. Resistance initially increases when exposed to low humidity environment. As this humidity increases, the amount that the resistance increases is reduced. A change occurs between potassium carbonate (~43% RH) and copper chloride (~67% RH), where the resistance starts to decrease. This is likely due to these two humidity standards falling either side of the ambient room humidity (averaged ~ 65% RH for this experiment). Following this switch, the resistance decreases as the humidity increases. Capacitance (figure S4.2) shows a similar response pattern, however with the capacitance decreasing at lower RH values, and increasing for higher RH. Likewise, a switch is observed around room humidity, as seen in the resistance. This is also shown in examining the percentage responses of both resistance and capacitance (Figure S4.3), where a linear trend of the responses can be observed.

As previously mentioned, the change in resistance with RH can be explained via the Grotthuss mechanism.[21,22] Water adsorption on chitosan results in hydrogen bond network formation with a greater density of conduction channels as the surface density of water molecules increases (as a result of increasing RH). [23]

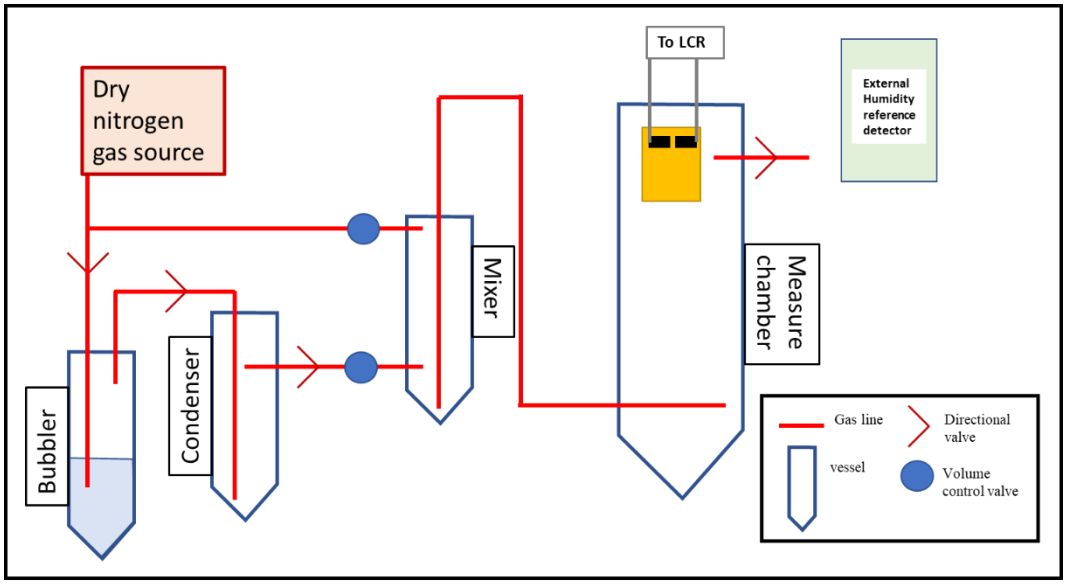
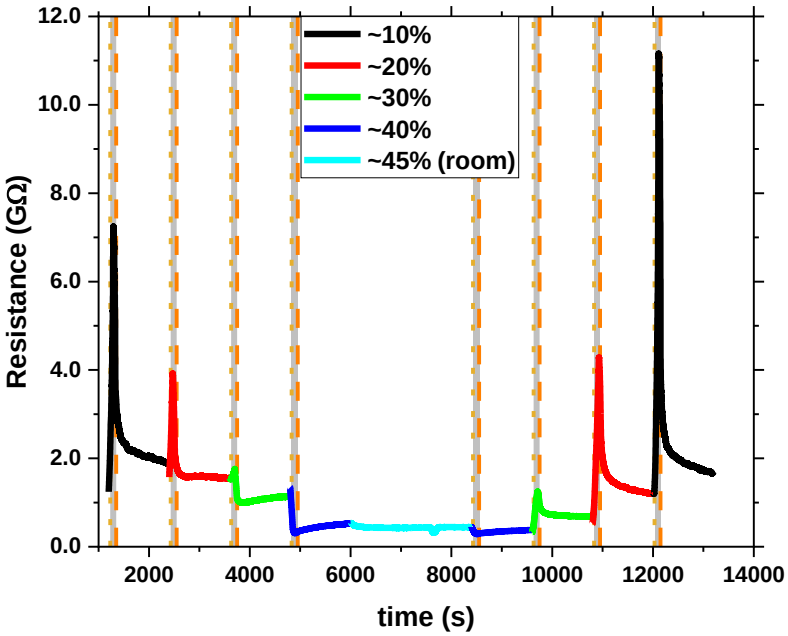


Figure 4.6 Humidity detection scheme with humidity-controlled nitrogen gas flow for chitosan-based laser-induced graphene fabricated 2-terminal impedance style sensors.

Additionally, improvements to experimental design by Richard Murray allowed for a closed chamber to be filled with humidified nitrogen gas flow as can be seen in figure 4.6. This was achieved by passing pressurised nitrogen gas through a bubbling system containing deionized water. This allowed for the carrying of water moisture via the gas flow. The gas flow was condensed and recombined with dry nitrogen gas flow before entering the measurement chamber. The relative humidity in the measurement chamber was controlled by controlling the amount of dry to wet gas allowed to pass through the system. The measurement chamber could then reach the required relative humidity, with excess gas expelled from the system via a one-way valve. To confirm internal relative humidity, an auxiliary humidity sensor recorded the humidity being expelled from the one-way valve.

(a)



(b)

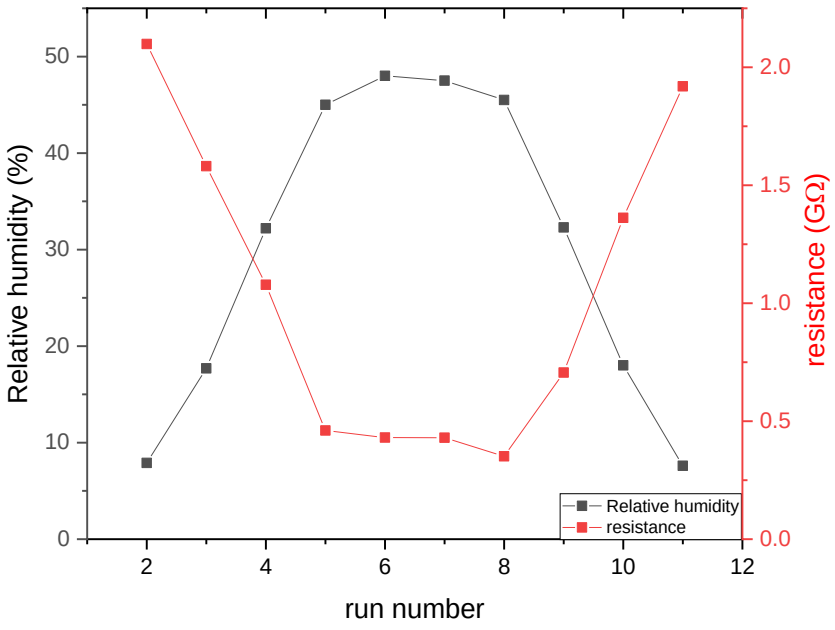


Figure 4.7 Humidity detection resistance response of chitosan-based laser-induced graphene fabricated 2-terminal impedance style sensors to humidity-controlled nitrogen gas flow

Figure 4.7a shows the real-time resistance variation (R_s signal for 1 kHz excitation) of the chitosan-based laser-induced graphene fabricated 2-terminal impedance style sensors under increasing and decreasing relative humidity environments. The current design set up only allows for a relative humidity range between ~0.2% to ~45% RH. Figure 4.7b shows the resistance value recorded 900 s after the humidified nitrogen was introduced. Notably, as seen with the aqueous saturated salt solutions, as the humidity increases, the resistance decreases, and vice versa. This figure also shows that the sensor can irreversibly desorb water moisture, when exposed to decreasing relative humidity environments.

Solvent VOC detection

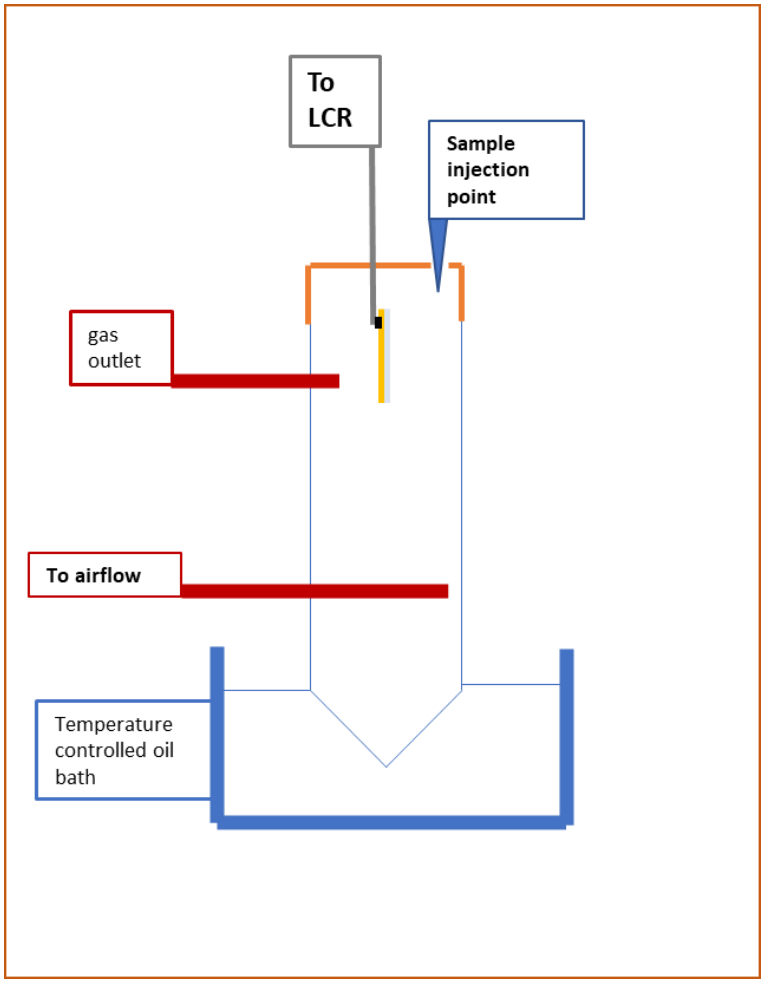


Figure 4.8. solvent detection scheme for chitosan-based laser-induced graphene fabricated 2-terminal impedance style sensors.

CLIG based solvent-VOC detection was completed by exposing the fabricated devices to known quantities of analyte, in a scheme shown in figure 4.5. CLIG-based 2-terminal impedance sensors were placed in a detection vessel. The CLIG device was connected into Agilent E53708B LCR Meter. The measuring voltage was set to 100mV AC, with a frequency of 1kHz. The capacitance and resistance of the devices were all measured in parallel. Analytes in question were inserted at an input port at the top of the vessel at known time, ensuring that the solvent did not come into contact with the device or top walls of vessel. Following saturation, the system was purged with pressurised humidified nitrogen airflow. The capacitance and resistance of the device was recorded in real time for both the exposure to the

analyte and the purge process, giving both a response and recovery curve for CLIG-based 2-terminal impedance sensors.

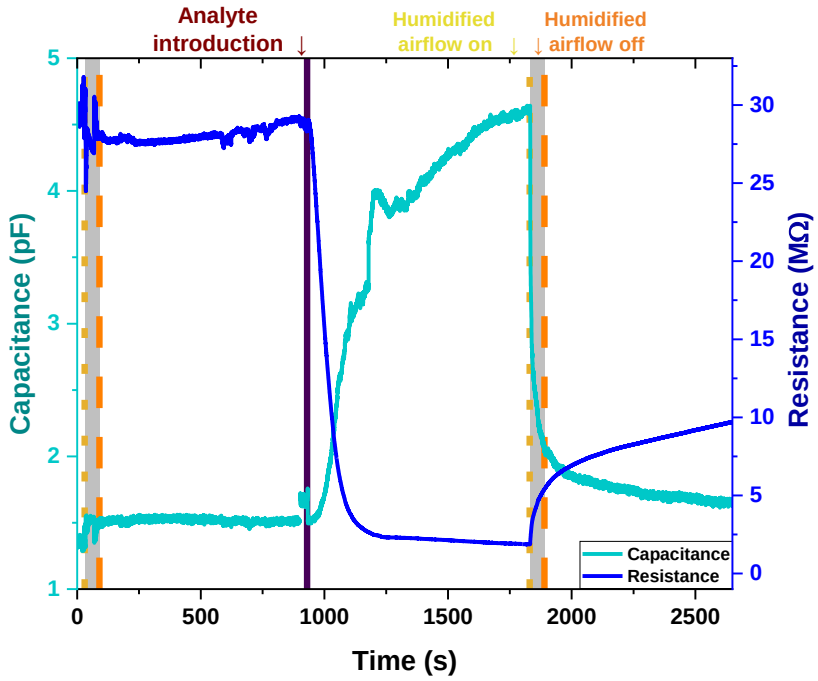


Figure 4.9 Resistance and capacitance measurements of a 2-terminal impedance chitosan based-LIG sensor measurement when exposed to 20 µL of ethanol in a 50mL vessel. Purple solid reference line representing analyte introduction, and grey representing purging via pressurized nitrogen gas (light orange dotted line; gas on, dark orange dash line: gas off)

An example of the reaction of one solvent (ethanol) when introduced into the measurement vessel, with the chitosan-based LIG sensor can be seen above, in figure 4.9. At the point of introduction, it can be observed that the conductance of the LIG sensor increases rapidly, before saturating due to the vapour being absorbed by the sensor. Additionally, the capacitance of the devices rapidly increases at the point of introduction, until it too saturates. Following a purging step, the ethanol in the system is evacuated, and the devices conductance and capacitance decreases, as the device recovers in the now analyte free vessel.

For comparison, various solvents were measured in a similar fashion as above, to show the devices potential selectivity for certain VOCs. Notably the magnitude of change of the devices resistance and capacitance can be noted between methanol, ethanol, isopropanol, and in particular acetone. In addition, the rates at which these solvents saturate the devices resistance and capacitance differs.

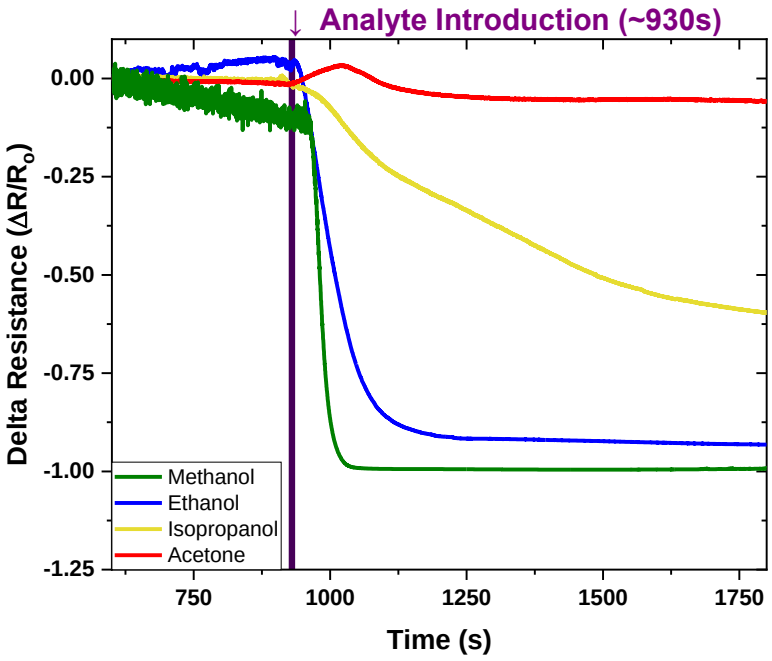


Figure 4.10 Comparison of delta resistive responses from 20µL various VOC solvents; methanol (green), ethanol (blue) isopropanol (yellow), and acetone (red). Purple solid reference line representing analyte introduction, and grey area representing purging via humidity controlled pressurized nitrogen gas (light orange dotted line; gas on, dark orange dash line: gas off)

The difference in resistance between solvents can also be explained by the Grotthuss mechanism. Similarly, to water, solvents with hydroxyl groups also are capable of forming hydrogen bonds, which in turn can form hydrogen bond networks. Hydrogen bond networks

form “proton wires”, which allow Grotthuss mechanisms to occur. However, for solvents not all hydrogen bonds are formed equally. Water readily can form hydrogen bonds with hydroxyl groups, whereas other molecules can’t. Hansen solubility parameter is a measure of a molecules capability to form hydrogen bonds, and a breakdown of various molecule’s Hansen parameter can be seen below in table 4.1

Table 4.1 Values of Hansen’s solubility parameter for selected solvents*

Solvent	Hansen solubility parameter δ_h[$MPa^{1/2}$]
Water	42.3
Methanol	22.3
Ethanol	19.4
Isopropanol	16.4
Acetone	7

*reproduced from ref. [24]

A smaller Hansen parameter means the molecule in question is less capable of forming hydrogen bonds. Less hydrogen bonds means a smaller hydrogen bond network is formed. A smaller hydrogen bond network results in less “proton wires”, reducing the possible protonic conductance.

Similarly, as previously mentioned, the polarity of water inhibits interactions between amine groups and protons. This means water can readily disassociate protons from protonated amine groups. This increases the density of mobile protons and increases the protonic conductance available. Some solvents however have a lower polarity. Examining the dielectric constant for individual molecules, their polarity can be determined. A breakdown of the various molecule’s dielectric constant can be seen below.

Table 4.2 Values of dielectric constants for selected solvents*

Solvent	Dielectric constant ε
Water	78.2
Methanol	33
Ethanol	24.9
Isopropanol	18.23
Acetone	20.7

*reproduced from ref.[25]

As the other solvents in this series have a lower dielectric constant and can be considered in comparison non-polar. As they are non-polar, they can't dissociate the protons from the protonated amine groups. This reduces the possible number of mobile protons in the system and reducing the possible protonic conductance.

4.4 Conclusions

To conclude, we have shown that chitosan-based laser-induced graphene two-terminal impedance devices can be used for detection of relative humidity and also volatile organic compounds. These results show encouraging progress towards sustainable fabrication of biodegradable sensing devices using low cost and low carbon footprint fabrication methods, ensuring a low environmental footprint across the entire life cycle of the device.

Chitosan-based laser-induced graphene 2-terminal impedance style sensors were shown to have a lower resistance in high humidity environments. Resistance increased in lower humidity environments. This was confirmed by both aqueous saturated salt solution standards, and controlled humidity nitrogen gas flows. Charge transport through the porous chitosan gap region can be explained by Grotthuss protonic conduction mechanisms, possibly aided by carbon inclusions in the gap region.

Similarly, the detection of solvent vapours was possible with chitosan-based laser-induced graphene 2-terminal impedance style sensors. The devices responded to the presence of most solvents by exhibiting a decrease in resistance following analyte introduction. The magnitude and rate of resistance change were both solvent-dependent, with the largest response observed for methanol, followed by ethanol, isopropyl alcohol and acetone. The data suggest that solvent adsorption may result in “blocking” of proton conduction channels, leading to increases in device resistance.

4.5 Experimental

Materials

Chitosan (medium molecular weight), acetic acid (> 99.8% purity), glycerol, methanol, ethanol, isopropanol, acetone and the standard salt were purchased from Sigma Aldrich and used without further purification. Milli-Q water (resistivity 18 MΩ.cm) was used throughout the experiments.

Chitosan film preparation

Chitosan films were obtained by dissolving 5 g of chitosan in 100 mL of acetic acid solution (5% v:v), followed by addition of 2 mL of glycerol. The obtained solution was heated at 70°C to homogenize components and sonicated for at least 2 hours to remove trapped air bubbles. Films (of thickness 0.1–0.15 mm) were prepared by doctor-blading chitosan formulations onto glass microscope slides and curing in an oven at 50 °C for ~10 hours.

Chitosan based laser-induced graphene sensors

2-teminal impedance style were fabricated using a combination of a commercial CO_2 hobbyist laser system (10.6 µm wavelength, 30 W maximum power, HQ-3020B, GuangZhou Amonstar Trade Co. Ltd) and a mini-speed laser engraving machine (Colemeter DK-8 Pro-5 Square Haste Edition, 405 nm diode laser, 500 mW power). Electrodes designed in Microsoft PowerPoint were fabricated by raster scanning of the laser beam to create the sensor pattern on the cured chitosan biopolymer surface. Graphene-like carbon structures were fabricated by a three-step multi-wavelength process whereby an initial pre-conditioning of the chitosan film was obtained by raster scanning the CO_2 laser (2.1 W, 110 mm/s scan speed, Step 1), followed by direct-write graphitization within the preconditioned area with a 405 nm laser (500 mW, dwell time 120 ms/pix, Step 2), followed by post-processing with CO_2 laser (2.1 W, 110 mm/s, Step 3).

Material characterisation

The morphological characterization of obtained sensors was performed Field-Emission Scanning Electron Microscopy (FESEM, Zeiss SUPRA 35 VP).

Humidity sensor characterisation

Chitosan-based laser-induced graphene sensors were placed inside varying vessels containing saturated salt solutions, producing standard humidity environments according to the E104-02 standard, that is, LiCl: 11% $MgCl_2$: 33.1% RH; K_2CO_3: 43.2% RH; NaCl: 75.5% RH; KCl 85.1% RH.37. Vessel volume was 50mL, with ample headspace between analyte and sensor. Between humidity standard measurements, sensors were placed in an empty vessel to allow for recovery, The capacitive and resistive response was measured using an AC potential sweep (Agilent E53708B LCR Meter, 1 kHz), at known time intervals.

Solvent sensor characterisation

Chitosan-based laser-induced graphene sensors were placed inside a measuring vessel of volume 50mL, with gas flow control inputs and outputs, used for purging the system. Vessel was semi-immersed in a temperature-controlled oil bath to aid evaporation of analytes in question, set to 60^{o}C. Analytes were introduced via micro syringe (Hamilton 50µL) and following saturation system of was purged via humidity control pressurised nitrogen flow and allowed device to recover. The capacitive and resistive response was measured using an AC potential sweep (Agilent E53708B LCR Meter, 1 kHz), measured in real time.

4.6 References

[1] J. Lin, Z. Peng, Y. Liu, F. Ruiz-Zepeda, R. Ye, E. L. G. Samuel, M. J. Yacaman, B. I. Yakobson, J. M. Tour, *Nat. Commun.* **2014**, *5*, 1.

[2] R. Ye, Y. Chyan, J. Zhang, Y. Li, X. Han, C. Kittrell, J. M. Tour, *Adv. Mater.* **2017**, *29*, 1.

[3] Y. Chyan, R. Ye, Y. Li, S. P. Singh, C. J. Arnusch, J. M. Tour, *ACS Nano* **2018**, *12*, 2176.

[4] S. Lee, S. Jeon, *ACS Sustain. Chem. Eng.* **2019**, *7*, 2270.

[5] J. Brugnerotto, J. Lizardi, F. M. Goycoolea, W. Argüelles-Monal, J. Desbrières, M. Rinaudo, *Polymer (Guildf).* **2001**, *42*, 3569.

[6] H. Yoon, J. Nah, H. Kim, S. Ko, M. Sharifuzzaman, S. C. Barman, X. Xuan, J. Kim, J. Y. Park, *Sensors Actuators, B Chem.* **2020**, *311*, 127866.

[7] F. Croisier, C. Jérôme, *Eur. Polym. J.* **2013**, *49*, 780.

[8] W. Wu, J. Shen, P. Banerjee, S. Zhou, *Biomaterials* **2010**, *31*, 8371.

[9] G. G. Chen, X. M. Qi, Y. Guan, F. Peng, C. L. Yao, R. C. Sun, *ACS Sustain. Chem. Eng.* **2016**, *4*, 1985.

[10] M. Dash, F. Chiellini, R. M. Ottenbrite, E. Chiellini, Chitosan - A versatile semi-synthetic polymer in biomedical applications. *Prog. Polym. Sci.* **2011**, *36*, 981–1014.

[11] N. Jabeen, I. Majid, G. A. Nayik, *Cogent Food Agric.* **2015**, *1*, 1.

[12] J. P. Kerry, M. N. O'Grady, S. A. Hogan, *Meat Sci.* **2006**, *74*, 113.

[13] Y. Xu, W. Cheung, C. L. Winder, R. Goodacre, *Anal. Bioanal. Chem.* **2010**, *397*, 2439.

[14] B. Fletcher, K. Mullane, P. Platts, E. Todd, A. Power, J. Roberts, J. Chapman, D. Cozzolino, S. Chandra, *CYTA - J. Food* **2018**, *16*, 1037.

[15] W. Chang, F. Liu, H. R. Sharif, Z. Huang, H. D. Goff, F. Zhong, *Food Hydrocoll.* **2019**, *90*, 50.

[16] Z. Chen, C. Lu, *Sens. Lett.* **2005**, *3*, 274.

[17] E. Traversa, *Sensors Actuators B. Chem.* **1995**, *23*, 135.

[18] H. J. Kim, J. H. Lee, *Sensors Actuators, B Chem.* **2014**, *192*, 607.

[19] Y. Sakai, Y. Sadaoka, M. Matsuguchi, *Sensors Actuators, B Chem.* **1996**, *35*, 85.

[20] ASTM International, *ASTM Stand.* **2003**, *E104-85*, 32.

[21] S. Cukierman, *Biochim. Biophys. Acta - Bioenerg.* **2006**, *1757*, 876.

[22] T. Miyake, M. Rolandi, *J. Phys. Condens. Matter* **2016**, *28*, 0.

[23] J. Zou, K. Zhang, Q. Zhang, *IEEE Sens. J.* **2016**, *16*, 8884.

[24] C. Zhang, T. Wen, M. Jiang, Y. Xu, H. Wang, J. Ouyang, J. Xu, *J. Mol. Liq.* **2022**, *346*, 118300.

[25] P. Marchetti, A. Butté, A. G. Livingston, *J. Memb. Sci.* **2012**, *415–416*, 444.

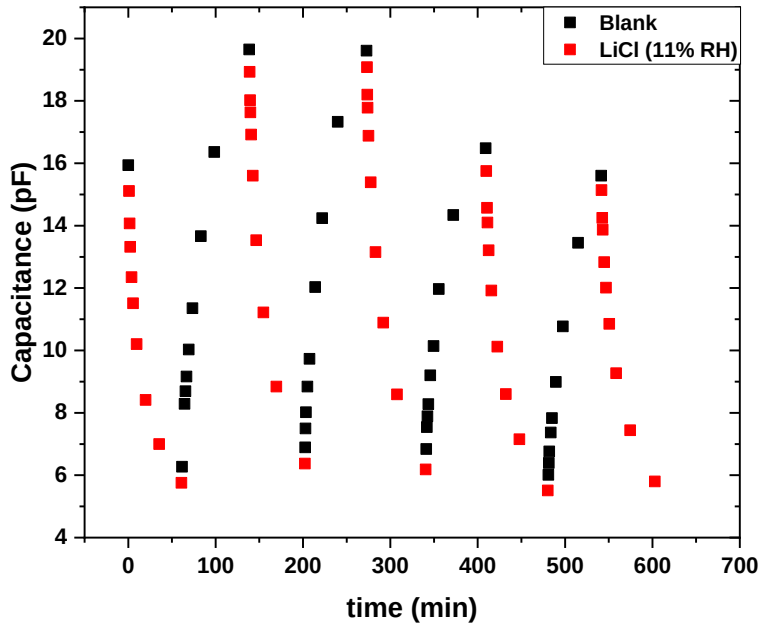


Figure S4.1 Repeated capacitance measurements from 2-terminal CLIG impedance sensors exposed to consistent humidity from an aqueous saturated salt solution of lithium chloride.

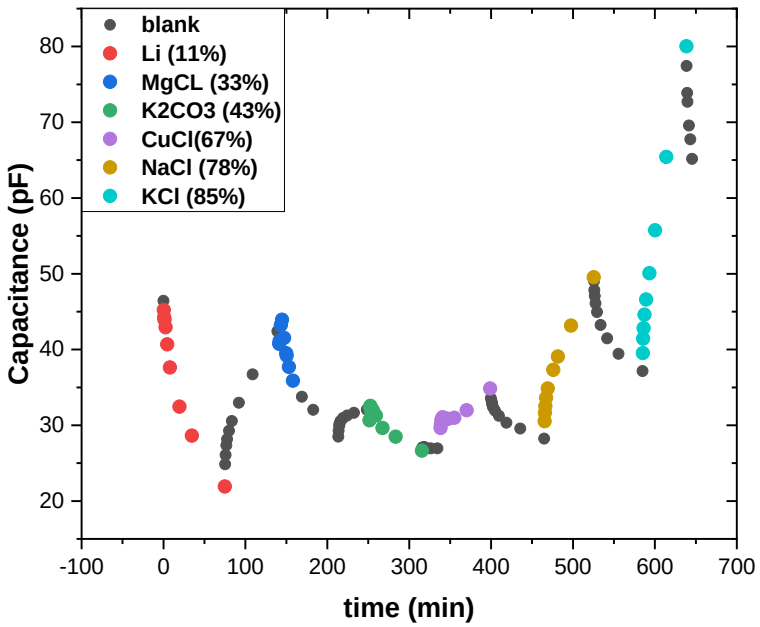


Figure S4.2 Capacitance measurements, from 2-terminal impedance Chitosan based-LIG sensor measurements when exposed to a series of aqueous saturated salt solutions.

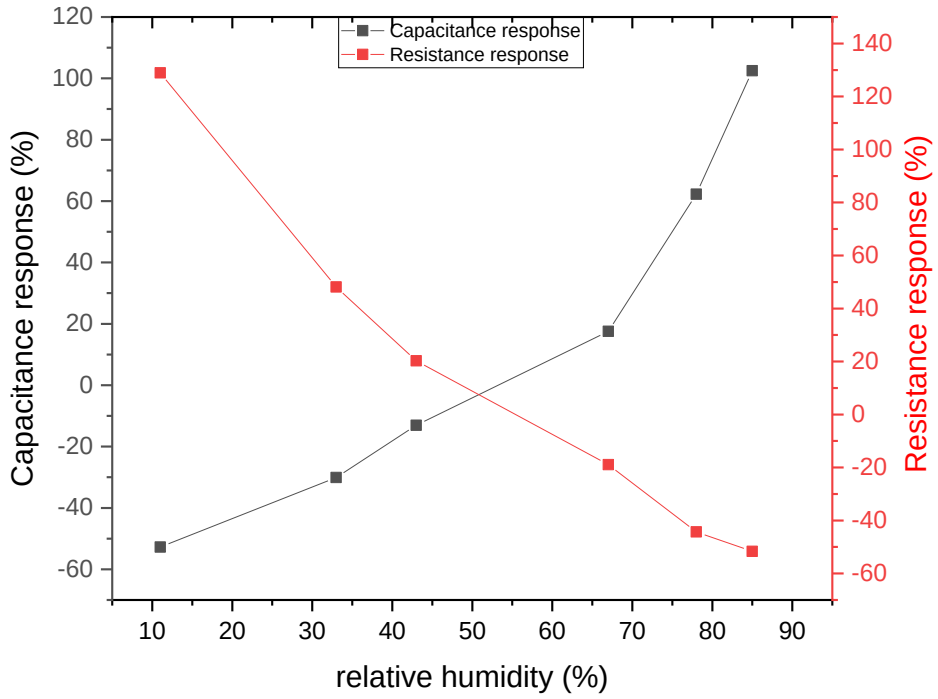


Figure S4.3 Percentage response from capacitive and resistive response of 2-terminal CLIG impedance sensors.

Chapter 5: Discussion and Conclusions

5.1 Discussion and Conclusion

The key driver for this study was to the examine and then determine the potential benefits of using laser-induced graphene fabrication as a more environmentally friendly approach to the fabrication of porous carbon sensing elements. This was explored in both examining lower carbon footprint manufacturing processes, as well as examining a more sustainable precusor substrate (chitosan) for LIG conversion and investigating potential sensor responses (humidity, VOC) of chitosan-based LIG devices.

The outline of the current state of the art of laser-induced graphene, mainly towards sustainablity was explored in chapter one. Laser-induced graphene supplies the community with a facile method of creating conductive carbon elements. Current methods outside of LIG to create graphene-like and graphtic materials, while showing a great advantges such as producing high quallity material, often have signficant disadvantages; difficulty at producing high volumes, expensive fabrication methods, and environmentally inefficient to name a few. Laser-induced graphene meanwhile provides a facile, inexpensive additive method to produce graphene-like and graphtic structures, in a manner which is significantly less environmentally damaging, and relatively simple to scale up to larger volumes.

While laser-induced graphene is a remarkable method at rapidly fabricating sensing elements, and with less environmental footprint than some contemporaries, there remains room for improvement. Much of the research is heavily dependent on specialized equipment, such as industry-level lasing systems, and controlled atmosphere enviroments. Its general dependancy on synthetic polyimide as a precusor material, leaves much to be desired. On one hand, polyimide-base LIG is a marked improvement on other fabrication methods that have a dependancy on raw materials, and produce a high amount of waste in production. Polyimide-based LIG, however, has depandcy on a non-sustainable feedstock material.

On the question of conversion material, while most research is based around polyimide, there have been some strides in utilizing more sustainable materials. Research directed at sustainablity has focused for the most part been directed on conversion of bulk woods, which leaves an open area of research toward other sustainable materials. As such, the direction of this thesis has been toward using bioplastic alternatives for LIG precusor material.

Chapter two explored the use of a low cost visible laser engraving machines under ambient conditions to produce laser-induced graphene material on polyimide (Kapton) tape. Under this method LIG was fabricated using a facile lasing method, over more extensive methods (CO_2 lasing for example). While in comparison to other contemporary lasing methods the quality of material produced was more akin to an amorphous carbon, than that of a graphitic material produced using a 10.6 µm CO_2 lasing process, the benefits of using such a methodology can outweigh such discrepancies. Here the lasing system used is a hobbyist engraving laser and was able to convert in ambient conditions. Even so, the end product was a material with a 3D porous morphology, low sheet resistance and graphene-like carbon spectral signatures. The ability for such a setup to produce material of this quality is remarkable considering its low overall financial cost, ease of use, and overall carbon footprint of the method when compared to similar processes using, for example, 10.6 µm CO_2 laser systems under controlled atmospheres. The benefits of this method were further explored by showing its potential as an electrochemical sensor, making the LIG produced ideal for such applications as a point-of-care sensing as it can produce devices for low cost and disposable analysis and development of versatile, low-cost electrochemical platforms.

Chapter 3 explored the use of a sustainable precursor feedstock material for laser-induced graphitization, namely chitosan biopolymer films. This chapter also highlights the potential of multi-wavelength, direct-write, multi-step conversion of aqueous biopolymer formulations into a graphene-like material. The potential of using sustainable LIG production,

in particular from a nontoxic, biodegradable, and compostable feedstock material, is a further highlight from this proof-of-concept work.

Finally, chapter 4 explored the potential of chitosan-based laser-induced graphene devices for impedance-based sensing of humidity and volatile organic compounds. These chitosan-based proof-of-concept LIG sensors showed clear responses to changing humidity from 0% RH to ~60% RH and detection of methanol, ethanol, IPA and acetone at ~100 ppm levels. By using LIG designs to form a current collector device with a dielectric gap between the two terminals consisting of chitosan film, a device could be fabricated with low carbon footprint on a biodegradable and compostable substrate.

The 2-terminal impedance style chitosan based LIG sensor was shown to have an increased conductance in the presence of a high humidity enviroment, with the conductance decreasing when exposed to low humidity enviroments. Results suggest that the sensing mechanism can be described in terms of Grotthuss mechanisms of protonic conduction in hydrogen-bonded networks, where the device resistance (inverse of conductance) increased when the Relative Humidity (and thus surface density of adsorbed water molecules) decreased. Similarly for VOC detection, our results suggest that adsorption of solvent molecules (in particular, methanol) can effectively block percolation paths through Grotthuss networks. Other factors (polarity) may allow for a certain level of solvent selectivity. These initial results illustrate the promise of sustainable sensors which could be incorporated into future intelligent packaging.

5.2 Future Work

Chapter 2 saw the development of low-cost and easily fabricated devices via low-cost visible laser engraving machines under ambient conditions to produce laser-induced graphene material on polyimide (Kapton) tape. While most of the focus of this thesis has been directed toward sustainable substrates, there are many potential further avenues of research towards the application and fabrication of said devices.

In fabrication for example, the focus of this thesis has been on a single 405nm diode laser engraving system as the lasing source for LIG fabrication. This device provides limitations in that only the dwell time could be varied for optimization. It is possible that other optimization paths are possible, one of the key parameters being varying laser power, as this current laser has a fixed power output of 500 mW. In addition, separate works from this thesis see great potential in other laser systems (For example polyimide-based LIG Via 450nm diode, and CO_2 laser irradiation). Using alternate laser systems allows for examination of different fabrication conditions such as laser wavelength, dwell time, focus plane and output power. This then provides optimization paths for the fabrication of LIG.

Proof-of-concept work in this chapter focused on electrochemical detection of analytes, showing a potential application in the detection of benzocaine. As this methodology can potentially produce low cost and disposable devices for flexible electrochemical platforms, verification of the ability to detect other analytes, and limit of detection of said analytes would be highly beneficial. Such scenarios which could benefit from LIG sensors include on-site monitoring of pesticides in water sources from an environmental aspect; detection of alcohol, narcotics, and toxins from a forensic aspect; and health monitoring of patients, for example glucose in sweat, from a medical aspect.

Chapter three explored the fabrication of chitosan-based laser-induced graphene as a method capable of producing biodegradable sensors with low environmental footprint across their entire life cycle. While chitosan based LIG shows great potential in this regard, there are many aspects in which this field can develop and grow. Although this work shows the potential of this chitosan film production, variations upon it may yield further benefits still. Altering the current formulation can produce chitosan films with differing properties. One aspect, for example, are chitosan blends. By incorporating other biopolymers, for example lignin, chitosan film can potentially become a more water resistive material, while maintaining its flexibility. Combining this with laser-induced graphene fabrication can allow for the development of sensors with a longer lifespan in more humid or moist environments, such as the proof-of-concept example of the electrochemical sensor detecting ferricyanide. Another example where this can be beneficial is wearable electronics. A wearable, more water resistive chitosan-based laser-induced graphene device would be particularly useful in fields such as health monitoring for applications such as smart bandages, glucose monitoring from sweat sensor, or measuring of muscle activity in physiotherapy patients.

The chitosan formulation from this thesis as it stands also has potential for further applications. The benefits of a compostable, biodegradable, and nontoxic sensing element can potentially yield a boundless number of potential applications. Some aspects of which were explored further in chapter 4, but additionally, potential applications such as monitoring of composting quality, through either pH, water content, or degradation rates within composters, disposable environmental electrochemical sensors, or environmentally friendly intelligent packaging.

Finally, the work in chapter 4 explores a potential application of chitosan-based laser-induced graphene in the form of a humidity and VOC sensor. While this shows a strong start for this branch of research, many aspects of this have yet to be full explored. The development

of real-time monitoring of the chitosan-based Laser-induced graphene 2-terminal impedance style sensors and humidified nitrogen airflow significantly improved the through-put and quality of measurements. However, future improvements to the design of the experimental set-up can widen and improve further the quality of studies possible. For example, current constraints with the set-up result in only low relative humidity detection for humidified nitrogen airflow. However, the addition of a heating element for the bubbling system can increase the capacity of humidity in the airflow system, thus increasing the relative humidity in the measuring chamber.

The current measurement set-up of VOC solvent detection can also be improved with further design additions. Currently a fixed volume of analyte is introduced into chamber and evaporated via the aid of a temperature-controlled heat bath. However future plans include the introduction of a solvent bubbling system, similar to the humidity detection regime, which will allow greater control of solvent concentration in the measurement chamber. However, due to the lack of an auxiliary VOC detector currently to know the concentration of VOC within the system, this method has not yet been explored.

On the topic of VOC and solvent detection, while the chitosan-based laser-induced graphene 2-terminal impedance style sensors could detect known concentrations of various solvents, the actual limit of detect of the sensors was not estimated, and a full investigation into the selectivity of sensor was not determined as of this point. Additionally, an investigation into a mixed gas, either with multiple solvents or solvent and humidified nitrogen air flow.

All of these improvements would in turn provide a more robust measuring system, which would then point to potential applications for chitosan-based laser-induced graphene 2-terminal impedance style sensors, namely intelligent environmentally friendly packaging methods.

Appendix A: peer reviewed publications

Main Publications

Fabrication and Electrochemical Properties of Three-Dimensional (3D) Porous Graphitic and Graphene like Electrodes Obtained by Low-Cost Direct Laser Writing Methods

Micheal Burke, Cathal Larrigy, Eoghan Vaughan, George Paterakis, Labrini Sygellou, Aidan J. Quinn, Grégoire Herzog, Costas Galiotis, and Daniela Iacopino.

ACS Omega 2020, 5, 3, 1540–1548. January 10, 2021. https://doi.org/10.1021/acsomega.9b03418

Targeted publications

Porous 3D graphene from sustainable materials: laser graphitization of chitosan

Cathal Larrigy, Micheal Burke, Alessandra Imbrogno, Eoghan Vaughan, Chiara Santillo, Marino Lavorgna, Labrini Sygellou, George Paterakis, Costas Galiotis, Daniela Iacopino, and Aidan J. Quinn.

Larrigy, C. et al. Porous 3D graphene from sustainable materials: laser graphitization of chitosan. Adv. Mater. Technol. doi:10.1002/admt.202201228 {in press}

VOC, solvent and humidity sensors from sustainable Chitosan- based Laser-induced graphitic carbon materials

Cathal Larrigy, Richard Murray, Micheal Nolan, Arbresha Muriqi, and Aidan J. Quinn.

In preparation for submission to Advanced Function Materials

Additional publications

Visible Laser Scribing Fabrication of Porous Graphitic Carbon Electrodes: Morphologies, Electrochemical Properties, and Applications as Disposable Sensor Platforms

Eoghan Vaughan, Cathal Larrigy, Micheal Burke, Labrini Sygellou, Aidan J. Quinn, Costas Galiotis, and Daniela Iacopino.

ACS Appl. Electron. Mater. 2020, 2, 10, 3279–3288. September 23, 2020. https://doi.org/10.1021/acsaelm.0c00612

Laser-Induced Graphene Supercapacitors by Direct Laser Writing of Cork Natural Substrates

Alessandra Imbrogno, Jahidul Islam, Chiara Santillo, Rachele Castaldo, Labrini Sygellou, Cathal Larrigy, Richard Murray, Eoghan Vaughan, Md. Khairul Hoque, Aidan J. Quinn, and Daniela Iacopino.

ACS Appl. Electron. Mater. 2022, 4, 4, 1541–1551. March 30, 2022. https://doi.org/10.1021/acsaelm.1c01202